# 실리콘 카바이드 가공을 위한 레이저-폴리싱 융복합 공정

## Hybrid Laser-Polishing Process for Machining Silicon Carbide

2019년 2월

서울대학교 대학원

기계항공공학부

김 민 철

# 실리콘 카바이드 가공을 위한
# 레이저-폴리싱 융복합 공정

## Hybrid Laser-Polishing Process for Machining Silicon Carbide

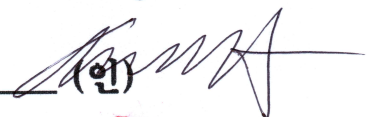지도교수 안 성 훈

이 논문을 공학박사 학위논문으로 제출함

2018년 10월

서울대학교 대학원
기계항공공학부
김 민 철

김민철의 공학박사 학위논문을 인준함

2018년 12월

위 원 장 : _____ (인)

부위원장 : _____ (인)

위　　원 : _____ (인)

위　　원 : _____ (인)

위　　원 : _____ (인)

# Abstract

# Hybrid Laser-Polishing Process for Machining Silicon Carbide

Mincheol Kim

Department of Mechanical and Aerospace Engineering

The Graduate School

Seoul National University

Silicon Carbide (SiC) is considered one of the best candidate materials for mirrors or structures for space optic applications because it has excellent mechanical and chemical properties, such as low density, high strength, low thermal expansion and superior chemical inertness. To fabricate optical elements, the work material needs to be polished and satisfy the requirements of accurate form and surface roughness at the same time. Given the micron-scale rate of material removal, however, the polishing is one of the most time-consuming processes. Furthermore, the extreme hardness and brittleness of SiC make it difficult and costly to fabricate for applications using conventional machining processes such as milling or turning.

There have been previous studies to investigate polishing SiC, including hybrid approaches of polishing SiC that employ external energy sources such as ultrasonic vibrations, magnetic fields or plasma. However, most of these efforts have been focused on roughness improvement. In contrast, improving the material removal rate

(MRR) has not received much attention. Laser beams have frequently been adopted in hybrid manufacturing as the best assistive energy source to improve MRR. However, the laser beam has not yet been adopted as an assistive energy source for polishing.

A novel hybrid polishing process, namely laser assisted polishing (LaPol), was developed in this study to improve the MRR of polishing SiC, by combining a $CO_2$ laser source with a conventional mechanical polishing process. For the first time a laser beam was synchronously irradiated through a rotating custom-made hybrid tool and focused onto the SiC surface during polishing in a water-based slurry environment. The effect of the resulting pre-cracked surface on material removal during the polishing of SiC was evaluated, along with characterization of the laser induced cracking, as well as the cracks' lateral length, vertical depth, the crystalline structure and chemical composition, local hardness and roughness.

The results showed that the MRR of SiC polishing increased by 79% using the LaPol process on a pre-cracked SiC surface, with new crack opening. In comparison, during normal polishing of the pre-cracked SiC surface, the MRR increased by 45%, leaving no deterioration or alteration, as compared to the normal polishing process of an as-received SiC surface. It is expected that the proposed LaPol process and understanding of the material removal mechanism will help expand the hybrid machining field and increase the industrial applications of SiC.

**Keyword: Hybrid machining, Surface finishing, Laser assisted polishing, Silicon carbide (SiC), Ceramics**
**Student Number:** 2013-30943

# Table of Contents

# List of Tables

# List of Figures

viii

# Chapter 1. Introduction

## 1.1.   Silicon Carbide

Silicon carbide (SiC), also known as carborundum, is one of the hardest materials in the world. It is believed that the SiC compound was first produced by Jöns Jacob Berzelius in 1824 [1]. The naturally occurring SiC mineral was first discovered by Ferdinand Henri Moissan in 1893 while examining rock samples found in the Canyon Diablo meteorite in Arizona, United States. It was named moissanite in his honor [2].

The smallest building element of any SiC lattice is silicon (Si) and carbon (C), and its structure is a tetrahedron consisting of a central Si atom surrounded by four C atoms, $SiC_4$, or *vice versa*, $CSi_4$, as shown in Fig. 1. Different polytypes, however, can appear based on different stackings of the tetrahedral layers. The cubic packing ABC becomes 3C ($\beta$-SiC), whereas, ABA'C' becomes 4H and ABCB'A'C' becomes 6H, both of which are the most common hexagonal polytypes and called $\alpha$-SiC (Fig. 2). 6H-SiC can also be regarded as a cubic structure with twinning. A large number of SiC polytypes are mixes of these polytypes, having numerous layers before repetition; these have an overall hexagonal structure [3].
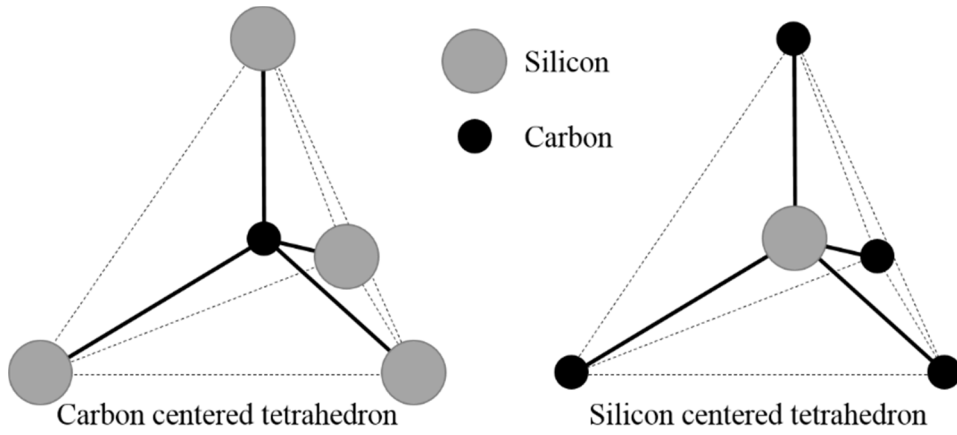
**Fig. 1 | Tetrahedral structure of SiC**
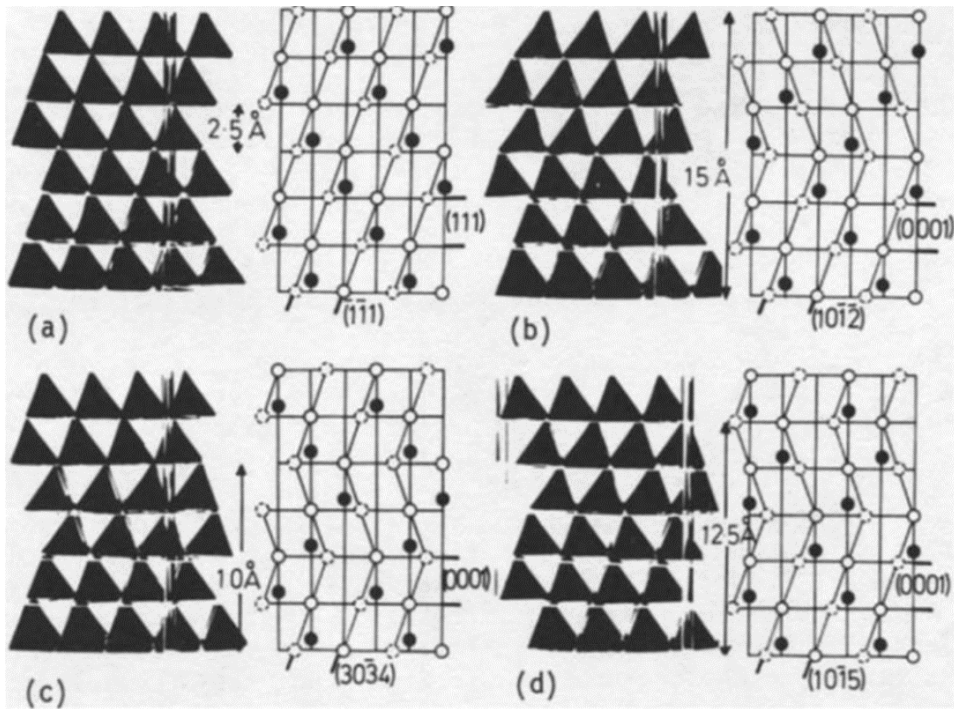


**Fig. 2 | Solid tetrahedral models with 'tramline' structure diagram [3]**

(a) 3C – ABCABC,    (b) 6H – ABCB'A'C',
(c) 4H – ABA'C'    (d) 15R – ABCB'A'BCAC'B'CABA'C'

SiC exhibits remarkable mechanical properties including high hardness, high strength, low density, high thermal resistance, and a very low thermal expansion, as listed in Table 1. These properties make it suitable for wide use in many applications in space optics and aerospace, defense, and the automobile industry. The mechanical properties of several optical materials are compared in Fig. 3.

However, its intrinsic hardness and brittleness are so extreme that its productivity is very poor, involving long process times and high cost with a great amount of tool wear. Besides, the machining process for the fabrication of optical parts which need a mirror-like surface quality is more complex, difficult, and expensive, along with shaping, grinding, polishing, and superfinishing [4-6].

**Table 1 | Mechanical and thermal properties of SiC polytypes [7-11]**

| Property | 3C-SiC | 4H-SiC | 6H-SiC |
|---|---|---|---|
| Young's Modulus [GPa] | 433 | - | - |
| Lattice Parameter [Å] | 4.36 | (a) 3.8 (c) 10.1 | (a) 3.1 (c) 15 |
| Density [g cm$^{-1}$] | 3.2 | 3.2 | 3.2 |
| Melting point [°C] | 2,830 | 2,830 | 2,830 |
| Moh's Hardness | 9 | 9 | 9 |
| Bulk Modulus [GPa] | 250 | 220 | 220 |
| Debye Temperature [K] | 1,200 | 1,300 | 1,200 |
| Thermal Conductivity [W cm$^{-1}$ °C$^{-1}$] | 3.6 | 3.7 | 4.9 |
| Thermal Diffusivity [cm$^2$ s$^{-1}$] | 1.6 | 1.7 | 2.2 |
| Thermal Expansion [10$^{-6}$ °C$^{-1}$] at 1,000°C | 3.8 | (a) 4.7 (c) 5.15 | ($\perp$c) 4.6 ($\parallel$c) 4.7 |
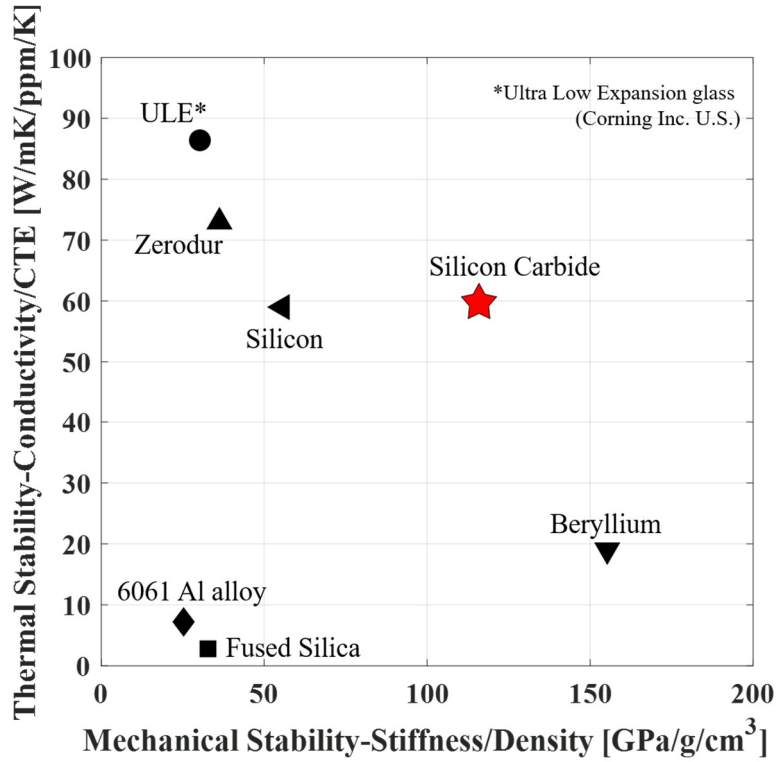
**Fig. 3 | Mechanical property comparison of optical materials**

## 1.2. Fabrication of Optic Parts

In general, an optical element is fabricated using the following common steps, each of which is processed differently depending on the optics and the quality [12]:

> ➢ Rough shaping: The fabrication of the initial blank. Typical error tolerance is within a few millimeters of the final dimensions.

> ➢ Support: The optic parts should be fixed for the successive operations, whose difficulty is mainly from the requirements of the support.

> ➢ Generating: The blank is engaged in the removal process; the tolerance is within 0.1~1 mm of the final dimensions.

➢ Fining: The optical surface is then ground to remove the damaged layer produced by the generating step, and the roughness tolerance is within 1~5 μm of the final shape.

➢ Polishing: The optical surface is repeatedly polished, and roughness decreased down from 0.1 μm to 5 nm.

➢ Centering and Edging: The optic is well aligned on a rotating tool and the outer edge is machined.

➢ Cleaning: The finished optic is cleaned and prepared for coating.

Successive coating and mounting process are generally not considered to be part of the optical fabrication process.

As mentioned above, the shaping process to reducing figure error is followed by several repetitions of the surface smoothing processes, such as grinding, polishing and magnetorheological finishing, MRF as shown in Fig. 4. As the smoothing process reaches the end, the removal amount, the corresponding surface damage and surface roughness all decrease [13].

The objective of any rough smoothing process like grinding is not only to reduce surface roughness but also is to reduce figure error created during the shaping process, down to 0.1~1.0 mm of the finished dimensions. Although the roughness can be decreased down to 0.1~10 μm, the formation of subsurface damage is inevitable. The damage generated by shaping and grinding is then removed in the subsequent fine smoothing process, such as polishing.

In the polishing process, the surface roughness is reduced to a few or tens of nanometers, removing the subsurface damage. The main purpose of polishing is to improve surface integrity in preparation for the superfinishing, MRF. The typical

comparisons of surface smoothing processes are summarized in Table 2 [12, 13].

As the process approaches the final stages, the productivity becomes lower. As a result, the overall productivity is predominantly determined by the final stage, the MRF process for peak-to-valley (pv) error reduction. Reducing subsurface cracks or damages for the MRF, the polishing process is very important. If the process efficiency of the polishing were improved up to that of grinding, the polishing can replace the grinding process, and reduce the complexity of the fabrication process, and thus improve overall productivity.
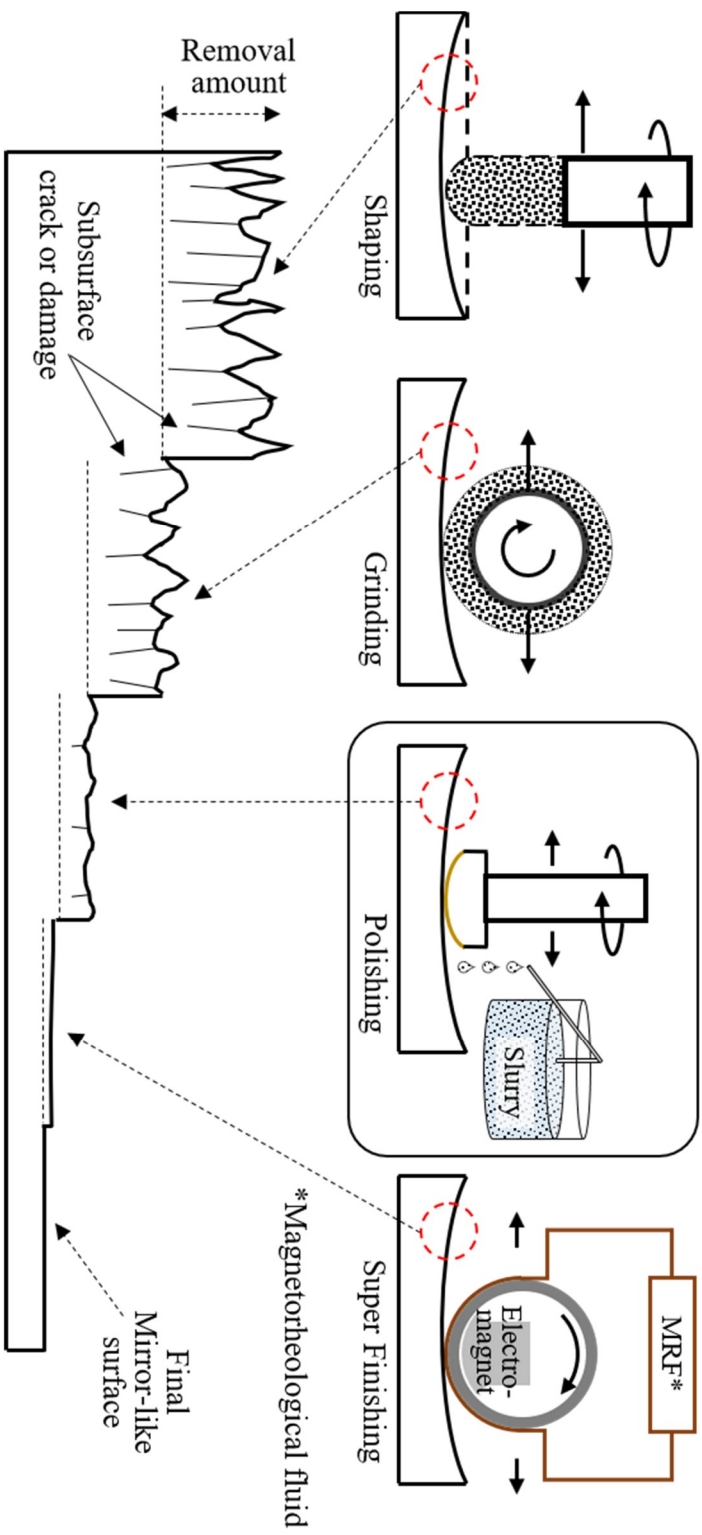
**Fig. 4 | Fabrication process of optic parts**

**Table 2 | Typical comparisons of surface smoothing process [12, 13]**

| Process | Grinding | Polishing | Super finishing |
|---|---|---|---|
| Objective | Form & RMS error reduction | RMS error & damage reduction | PV error & damage reduction |
| Abrasive size | $30 \sim 200$ μm | $0.1 \sim 1$ μm | $\sim 0.1$ μm |
| Roughness ($R_a$) | $0.1 \sim 10$ μm | $0.005 \sim 0.05$ μm | $< 5$ Å |
| Removal depth | $0.1 \sim 1$ mm | $0.1 \sim 100$ μm | $\sim 0.01$ μm |
| Problem | Damage formation | Time consuming | Time consuming |

## 1.3. Previous Study on Polishing

### 1.3.1. Single Polishing of SiC

Polishing is one of the most conventional machining processes to remove material, by mechanically rubbing the surface of the workpiece with abrasive particles and polishing pad [14, 15]. It is very useful for the machining of advanced ceramics and improving surface integrity, such as the reduction of roughness, residual stress, and subsurface damage. Although the removal rate of the polishing process is known to be very low, it can render nanometer-scale roughness on the surface of the workpiece.

The main purpose of the polishing is to reduce surface roughness, and most of the studies regarding polishing of SiC have focused only on the surface roughness, as listed in Table 3 [16-24]. However, improving the material removal rate (MRR) of polishing has not received much attention, even though it is still important for productivity. There have been a few studies regarding both removal rate and roughness in the polishing of SiC, as shown in Fig. 5 [16-18, 22, 23], suggesting there is a trade-off relationship between them. As previously stated in Chapter 1.2, the higher the surface quality that is achieved, the lower the removal rate.

**Table 3 | Previous study of single polishing of SiC**

| Mat. | Purpose | Abrasive | Grit size [μm] | Roughness, Ra [nm] | MRR [μm/min] | Ref. |
|---|---|---|---|---|---|---|
| (RB) SiC | Roughness | Diamond | 1~10 | 21.6 →10.7 | ~ 0.95 | [16] |
| SiC | Removal characteristics | Diamond | 0.5~7 | 1.45 | 0.017 | [17] |
| (S) SiC | Removal characteristics | Diamond | - | 47.5 *(pv 190.1)* | 0.45 | [18] |
| SiC | MRR | $KM_nO_4$, $Al_2O_3$ | - | 0.8 | 0.0075 →0.018 | [22] |
| (4H) SiC | Removal characteristics | Fe, $Al_2O_3$ | 0.5, 0.05 | 1.7 | 0.012 | [23] |
| SiC | Effect of micro-structure | Diamond | 1~3 | 3.02~8.38 | - | [19] |
| (4H) SiC | Abrasive free polishing | Diamond | - | 0.546 | - | [20] |
| (RB) SiC | Roughness | CeO | - | 353 →134.30 | - | [21] |
| (RB) SiC | Single grit simulation | Diamond | 0.5 | 152 | - | [24] |
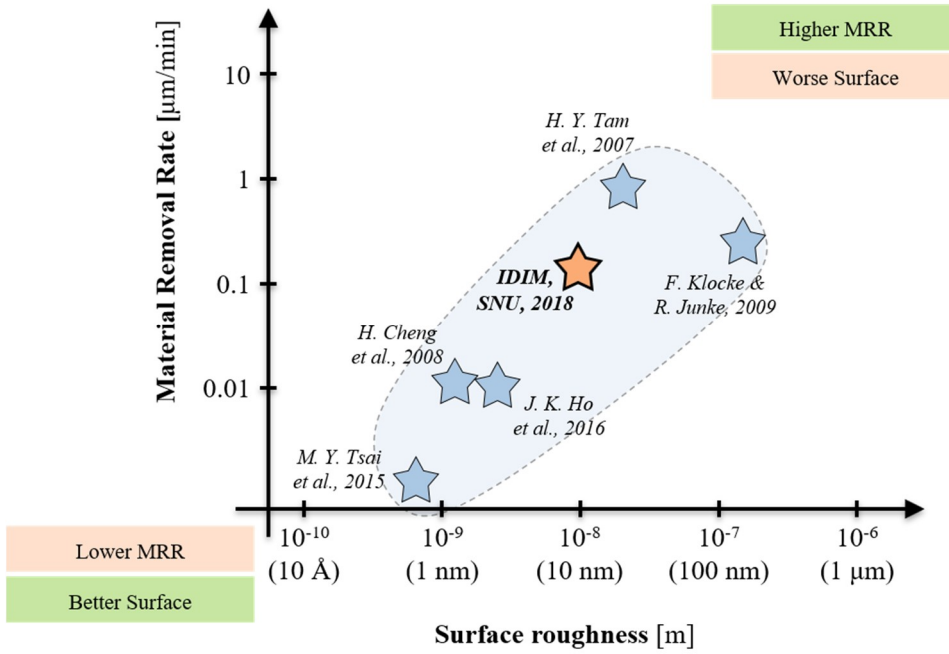
**Fig. 5 | Tradeoff relationship between MRR and surface quality**

### 1.3.2. Hybrid Polishing Process

With increasing demand for advanced ceramics applications, researchers have developed various hybrid machines and processes, integrating multiple energy sources or process mechanisms within one machining platform [25], in an attempt to enhance their individual advantages and reduce potential disadvantages [26]. Laser assisted machining (LAM) [26-29] has emerged as one of the best examples of hybrid machining. There have also been hybrid approaches for polishing SiC [25] utilizing an external energy source such as ultrasonic vibration [30-33], magnetic field [34, 35] or plasma [36]. However, the purpose of these hybrid works was primarily to improve surface roughness. Although laser assisted polishing of SiC has

10

recently been reported in a conference paper, the author did not demonstrate any simultaneous assisted polishing at all, but conducted UV laser induced surface oxidation, suggesting that the oxidation might enhance the removal rate of SiC polishing [37]. See the summary in Table 4.

**Table 4 | Hybrid polishing process**

| Process | Assistive energy | Mat. | Purpose of Hybrid | Roughness, Ra [nm] | MRR [μm/min] | Ref. |
|---------|------------------|------|-------------------|--------------------|--------------|------|
| Hybrid Polishing | Ultrasonic Vibration | Si | Roughness | 54 | - | [30] |
| | | STAVAX | Roughness Tool wear | 100 → 36 | - | [31] |
| | | WC | Roughness Form error | 3.0 → 1.2 | - | [32] |
| | | HPM75 | Roughness | 400 → 58 | - | [33] |
| | B-field | SiC | Roughness | 26.74 | - | [34] |
| | | Quartz | Roughness | ~ 1 | - | [35] |
| | Plasma | SiC | Roughness | ~ 0.1 (RMS) | - | [36] |
| | Laser | SiC | MRR | - | - | [37] |

## 1.4.   State-of-the-Art

As shown in Table 5, a laser source has been widely used and frequently adopted for various hybrid machining processes to improve process performance by enhancing advantages and reducing potential disadvantages found in individual processes [25] In most cases, however, the hybridization of thermal energy and a machining tool

has necessarily been carried out without a liquid based coolant or slurry, and therefore a laser assisted polishing process with slurry has yet to be implemented. Alternatively, research has been conducted on laser induced surface modification of advanced ceramics, and its effect on the machinability of materials in a subsequent machining process.

**Table 5 | Combinations of assisted hybrid process [25]**

| Relative frequency of journal papers<br>● Very frequent<br>◑ Frequent<br>○ Partly | | Primary Process | | | | | | | | | | |
|---|---|---|---|---|---|---|---|---|---|---|---|---|
| | | Turning | Milling | Drilling | Grinding | Polishing | EDM | ECM | Laser | Forming | Shearing | Etching |
| Secondary assistive process | Vibration (Ultrasonic) | ● | ○ | ◑ | ● | ◑ | ● | ◑ | ○ | ○ | | |
| | Laser | ● | ◑ | ◑ | | X | | | | ◑ | ○ | ○ |
| | Water-jet | | | | | | | | ○ | | | |
| | Pressure fluid | ◑ | | | ○ | | | | | ● | | |
| | Magnetic field | ○ | | | | ◑ | ○ | ○ | | | | |
| | Conductive heat | | | | | | | | | ◑ | | |

According to Xiao Yang *et al.*, the flexural strength of a SiC surface is decreased by thermal shock, and inner and surface artificial defects (pre-cracked surface) enhances crack propagation during thermal shock processes [38]. A laser (Nd:YAG) shock peening process was conducted on SiC, resulting in a modification of the surface properties, including morphology, an improvement in hardness, and

reduction in fracture lengths [39]. In a recent study, the femtosecond laser irradiation of a single SiC crystal generated ripples, oxidation, and an amorphous layer on the surface, which resulted in a higher removal rate and better surface planarization in chemical-mechanical polishing (CMP) process [40]. Laser induced microstructure design was able to increase the MRR in the subsequent grinding of silicon nitride, reducing the grinding force and wheel wear [41]. However, little attention has been paid to the effect of laser induced surface or subsurface cracks on the material removal characteristics and enhancement of MRR in the mechanical polishing of hard-to-cut materials.

## 1.5.    Objectives

As briefly reviewed, there have been a few assistive processes reported for polishing, but laser assisted polishing has not yet been studied. In this study, I'm going to improve both MRR and surface roughness using the laser assisted polishing process. It was hypothesized that the pre-cracked surface caused by laser irradiation may enhance the machinability of SiC in the subsequent mechanical polishing process. A novel hybrid SiC machining process was demonstrated to improve MRR. The process is called laser assisted polishing (LaPol), combining a $CO_2$ laser source and a slurry-based free abrasive polishing process within a single machining platform. The laser beam is irradiated along a hollow channel fabricated into the center of a rotating tool, focused on top of the SiC workpiece. The objective of the current study was to characterize the laser induced surface modification, investigate the effect of

the cracked surface on the subsequent polishing, and improve the productivity of SiC in terms of MRR and surface quality.

## 1.6. Dissertation Overview

When fabricating SiC optics, the poor machinability of the material and high complexity of the process results in very poor productivity, as discussed in Chapter 1. In Chapter 2, the principles of the material removal mechanism for laser-ceramic interaction, polishing, and LaPol is presented. In Chapter 3, the hybrid laser-polishing machine, consisting of LBM and mechanical polishing to improve the productivity of machining SiC, is introduced. In Chapter 4, the laser induced surface modification is characterized in terms of crack formation, crystalline structure and elemental composition. In Chapter 5, the removal processes is evaluated for performance and to investigate the removal mechanism. In Chapter 6, the differences and limitations of the current study is discussed. In Chapter 7, conclusions is drawn.
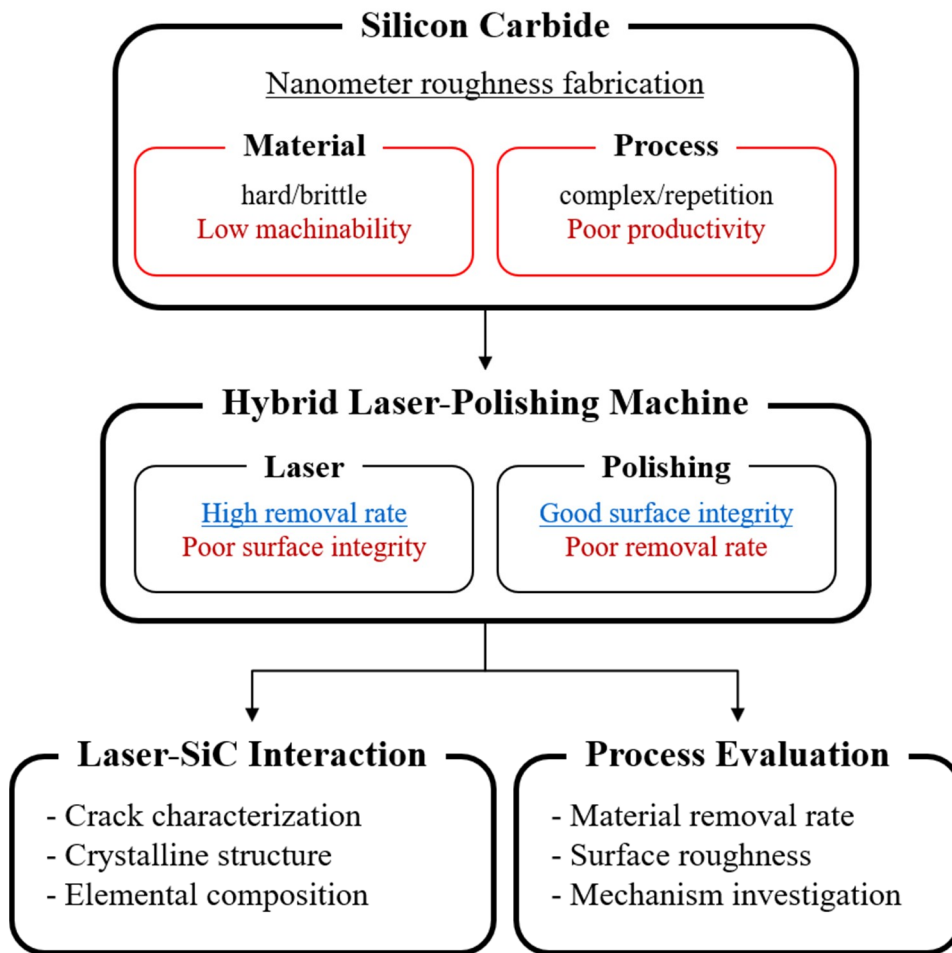
**Fig. 6 | Overview of the study**

# Chapter 2. Principles of Material Removal

## 2.1. Laser-Ceramic Interaction

### 2.1.1. Laser Beam Machining (LBM)

LBM has been studied and reviewed for decades [42-51] as a method for fabricating hard-to-cut materials for industrial applications. Achieve a very high rate of material removal, lasers have been widely adopted in various machining processes including cutting [46], drilling [52] and 3D structuring [53] of hard-to-cut materials. Depending on what material is being machined, and which process is being employed, the appropriate laser is selected in terms of the output wavelength, average and peak power, beam quality and also cost *etc*. [54]. Despite its high removal efficiency, however, LBM typically leaves poor surface integrity or roughness in hard-to-cut materials, and consequently the process frequently requires a subsequent finishing process such as grinding and polishing.

When the laser is irradiated on the surface of ceramic materials, various physicochemical phenomena take place, including heating, melting, dislocation, evaporation, and dissociation, as illustrated in Fig. 7. These effects are responsible for the material removal process [55]. Laser heating causes the temperature of the laser irradiated surface to rise as the material absorbs thermal energy. Once the temperature reaches its melting point and then exceeds its boiling point, melting / dislocation and evaporation / dissociation take place on the surface, respectively [46, 48].

The laser induced molten materials can also re-solidify around the beam spot

16

[56], where the temperature is a bit lower. Also, the dissociated molecules mostly react with oxygen [57] or rarely with nitrogen [58] in the air, generating oxidation or a nitriding layer on the surface [59]. Since the temperature difference inside the brittle material increases internal thermal stress, a large temperature gradient might result in crack generation, despite the fact that the ceramic material is very resistant to thermal shock [60]. Both are considered defects of laser related material processing, because they generate geometrical irregularities [61].
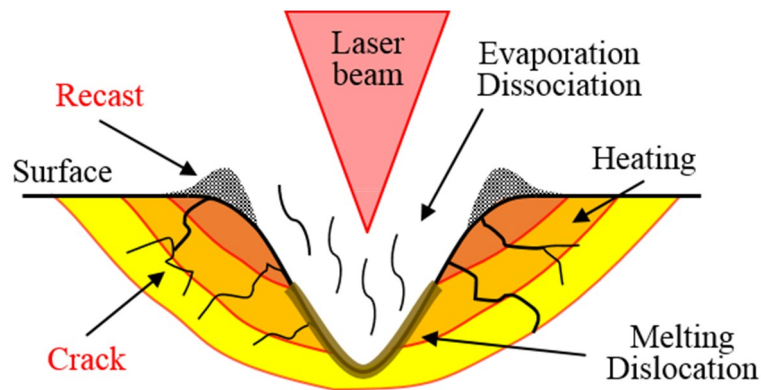


**Fig. 7 | Laser ceramic interaction**

### 2.1.2. CO$_2$ Laser-SiC Interaction

At less than $100 per watt, the CO$_2$ laser is the least expensive of any laser source. Due to the merit of cost, the maturity of the CO$_2$ laser is very high, and then it can offer a variety of output powers, ranging from a few watts to over 60 kW [54]. The output wavelength of a CO$_2$ laser can be chosen between 9 μm and 11 μm, but is most frequently 10.6 μm, which is the mid-infrared range.

One characteristic infrared property of SiC is the intrinsic reflection band at 12 μm, as shown in Fig. 8 [62, 63]. With increasing temperature its absorptivity at 10.6 μm increases up to 80%, as shown in Fig. 9 [64]. Accordingly, the $CO_2$ laser has long been employed for research on the material processing of SiC, including shaping [49], ablation [50], cutting [42] or drilling [51].
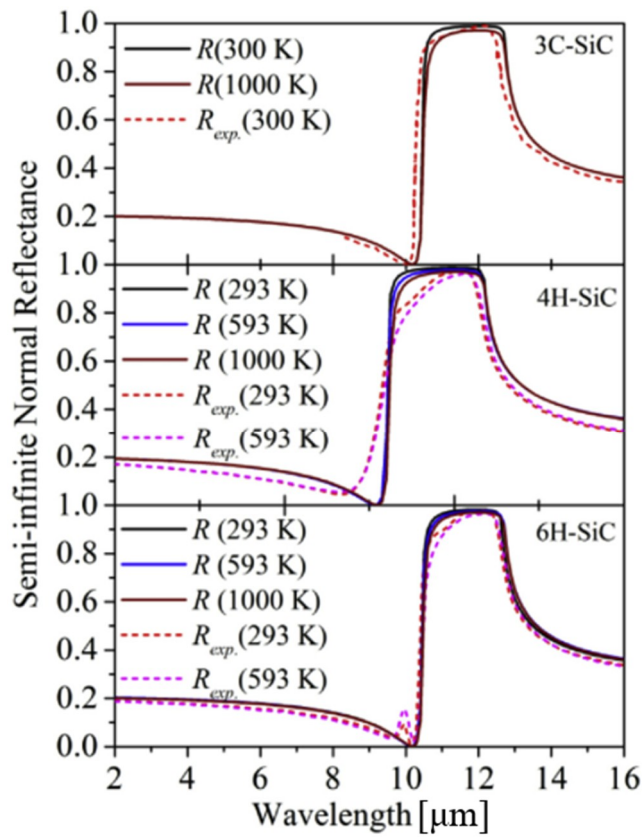


**Fig. 8 | Semi-infinite normal reflectance of SiC [63]**
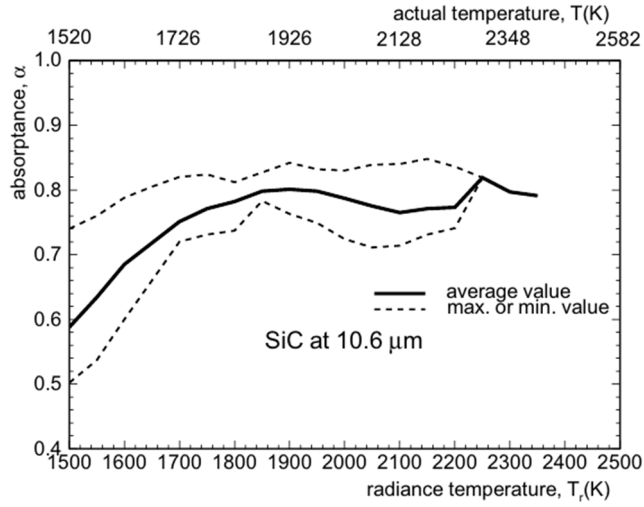
**Fig. 9 | Absorbance of SiC at 10.6 μm with temperature [64]**

$$2C(s) + O_2(g) \rightarrow 2CO(g)$$

$$2CO(g) + O_2(g) \rightarrow 2CO_2(g)$$

$$SiC(s) \rightarrow Si(l) + 2C(s)$$

$$2SiC + O_2(g) \rightarrow 2SiO(g) + 2C(s)$$

$$2SiO(g) + O_2(g) \rightarrow 2SiO_2(s)$$

$$2C(s) + N_2(g) \rightarrow (CN)_2(g)$$

$$3SiC + 2N_2(g) \rightarrow Si_3N_4(s) + 3C(s)$$

$$6C(s) + 3N_2(g) \rightarrow 3(CN)_2(g)$$
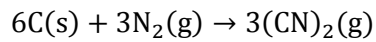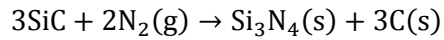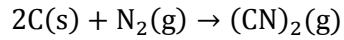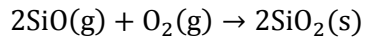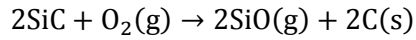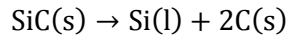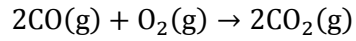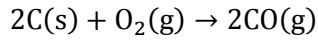
**Eq. 1 | Laser induced chemical reaction of SiC with atmosphere gas [65]**

19

Thermal energy induced by the $CO_2$ laser can cause chemical reactions on the surface of SiC, which consists of silicon and carbon. The chemical reactions between SiC and atmospheric gases such as oxygen and nitrogen are represented in Eq. 1. Note that the toxic gas, carbon monoxide, $CO$ and cyanogen, $(CN)_2$ are formed. The characteristics of oxidation and nitriding of SiC are summarized in Table 6, which is of interest in the current study.

**Table 6 | Laser induced oxidation and nitriding of SiC [66]**

| Chemical reaction / formation | Appearance | Hardness [kg/mm$^2$] |
|---|---|---|
| $2SiC + 3O_2 \xrightarrow{\Delta t°C} 2SiO_2 + 2CO$ | Transparent solid, White, Whitish Yellow | 600 |
| $6SiC + 7N_2 \xrightarrow{\Delta t°C} 2Si_3N_4 + 3C_2N_2$ | Grey | 1,580 |

## 2.2.   Polishing

### 2.2.1.   Contact Mechanism

Free abrasive machining is a material removal process that involves rubbing the surface of the workpiece with free abrasive particles. The best example is mechanical polishing [14, 67]. There are four process components in the material removal mechanism of polishing: the workpiece, abrasives, fluid and pad [68]. Since the fluid is a transporter of the abrasive and a medium for heat removal from the workpiece surface, the material removal takes place due to wear caused by the pad-abrasive-

workpiece interactions [68, 69]. During the polishing process, the three components

are contacting each other, in a process governed by contact theory, as shown in Fig.

10 (Eq. 2) and Fig. 11 (Eq. 3) [70-73].
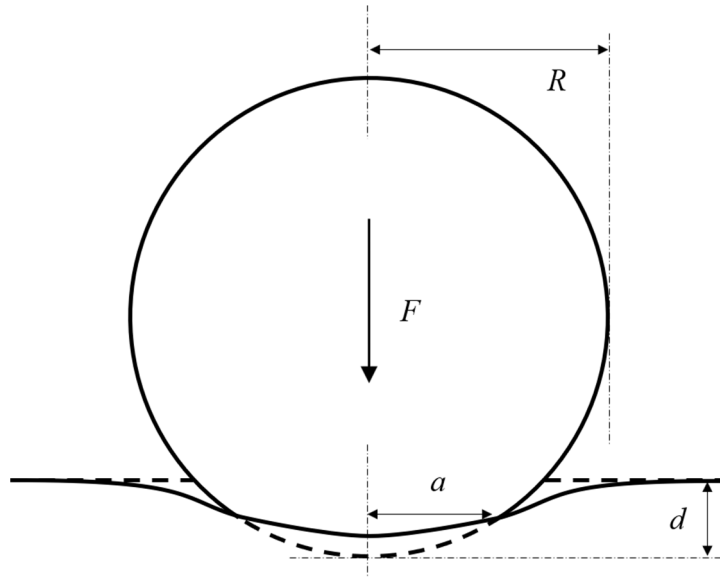


**Fig. 10 | Contact model between a sphere and a half-space**

$$a = \sqrt{Rd}$$

$$F = \frac{4}{3}E^*R^{1/2}d^{3/2}$$

$$\frac{1}{E^*} = \frac{1-v_1^2}{E_1} + \frac{1-v_2^2}{E_2}$$

$$p(r) = p_0\left(1 - \frac{r^2}{a^2}\right)^{1/2}$$

$$p_0 = \frac{3F}{2\pi a^2} = \frac{1}{\pi}\left(\frac{6FE^{*2}}{R^2}\right)^{1/3}$$

$$a^3 = \frac{3FR}{4E^*}$$

$$d = \frac{a^2}{R} = \left(\frac{9F^2}{16E^{*2}R}\right)^{1/3}$$

**Eq. 2 | Contact between a sphere and a half-space**

where $E_1$, $E_2$ and $v_1$, $v_2$ are the elastic modulus and Poisson's ratio of each body, respectively, $F$ is total force, $p(r)$ is the distribution of normal pressure in the contact area as a function of distance from the center of the circle, $p_0$ is the maximum contact pressure, $d$ is the depth of indentation. [70, 74]
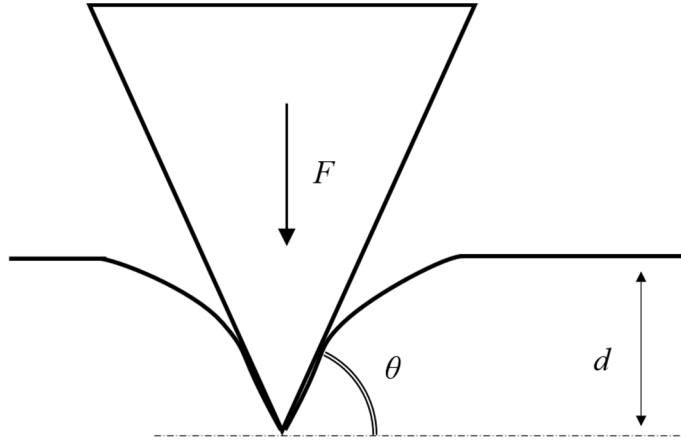
**Fig. 11 | Contact model between a conical indenter and a half-space**

$$\epsilon = a \tan \theta$$

$$d = \frac{\pi}{2} \epsilon$$

$$F = \frac{\pi E}{2(1 - v^2)} a^2 \tan \theta = \frac{2E}{\pi(1 - v^2)} \frac{d^2}{\tan \theta}$$

$$p(r) = \frac{Ed}{\pi a(1 - v^2)} \ln\left(\frac{a}{r} + \sqrt{\left(\frac{a}{r}\right)^2 - 1}\right) = \frac{Ed}{\pi a(1 - v^2)} \cosh^{-1}\left(\frac{a}{r}\right)$$

**Eq. 3 | Contact between a conical indenter and a half-space**

where $\epsilon$ and $a$ are the contact region and radius, respectively, $\theta$ is the angle between the plane and the side surface of the cone, $d$ is the depth of indentation, $F$ is total force, $p(r)$ is the pressure distribution [73].

## 2.2.2. Abrasive Wear

Unlike conventional material removal processes, such as milling or turning, the main mechanism of material removal in polishing is the abrasive wear. The wear rate is directly proportional to the applied load and sliding distance of each abrasive, and is inversely proportional to the hardness and fracture toughness of the material [75, 76]. During polishing, the workpiece is removed by the pad-abrasive-workpiece interaction, occurring as three-body rolling wear. When the free abrasive is stuck into the pad, which then act as a single body, two-body sliding wear also takes place [77] as shown Fig. 12.
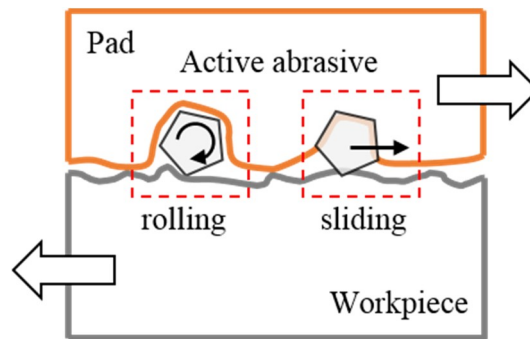


**Fig. 12 | Multibody wear model**

Three-body wear refers to hard particles between two sliding surfaces, which plow through at least one surface. Two body wear refers to a rough and hard surface whose asperities plow through the stronger counter face, while protrusions plow through it. Surface penetration causes indentation and local plastic deformation. These two wears are not mutually exclusive, as two body wear can often lead to three

body abrasion when hard abrasive particles are separated from the surface, and *vice versa* [75-78].
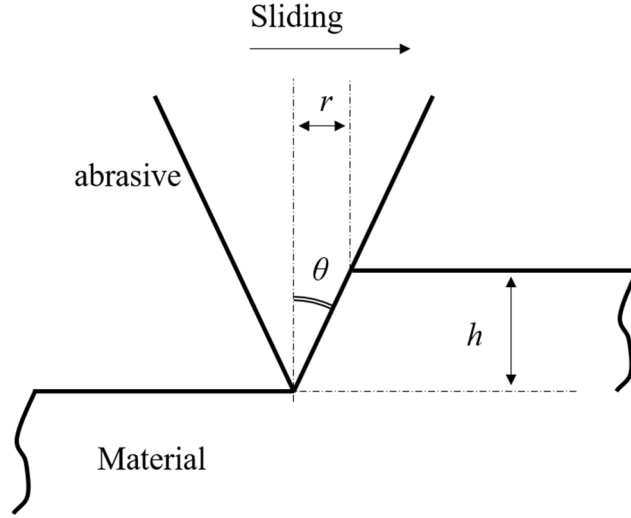


**Fig. 13 | Plowing of a softer surface by a hard-conical asperity**

$$v = rh = r^2 \tan \theta$$

$$N_i = 0.5\pi r^2 \text{H}$$

$$v = 2N_i \tan \left( \frac{\theta}{\pi H} \right)$$

$$Q = 2N \tan \left( \frac{\theta}{\pi H} \right)$$

**Eq. 4 | Total wear amount for all asperities in abrasive wear**

where $v$ is the volume for a single asperity from the sliding displacement, $N_i$ is the normal load on the single asperity, $H$ is the hardness of the material, $Q$ is the wear amount for all the asperities [76].

### 2.2.3. Preston Model

Preston's law determines the material removal amount in polishing [15] which depends on how strongly, how fast and how long the workpiece is rubbed, as shown in Fig. 14 and Eq. 5.

$$\Delta z = kPV\Delta t$$

**Eq. 5 | Preston's equation**

where $P$ is polishing pressure, $V$ is the relative velocity of pad and workpiece, and $\Delta t$ is dwell time.

A synchro-speed kinematics renders the material removal in polishing more predictable, where polishing pressure and relative velocity are evenly distributed on the whole surface by a computer numerical control (CNC) based polishing machine, so that the MRR is defined as the removal height per unit time, viz. nm/min or μm/min [18].

### 2.2.4. Planetary Motion Model

A planetary motion model was established, as shown in Fig. 15. The self-rotating tool moves in an orbital motion with a tool radius eccentricity of 60% and a negative relative velocity [79].
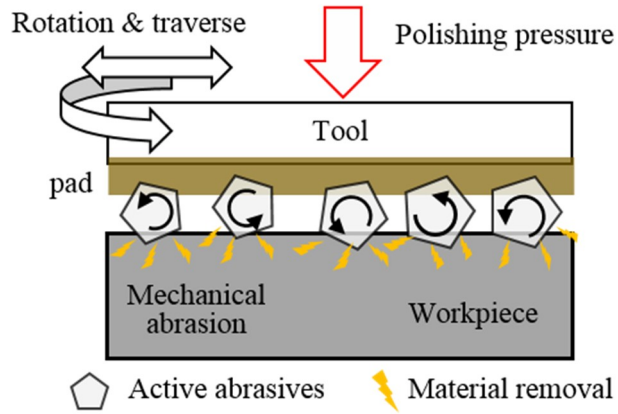
**Fig. 14 | Material removal mechanism of mechanical polishing of SiC**
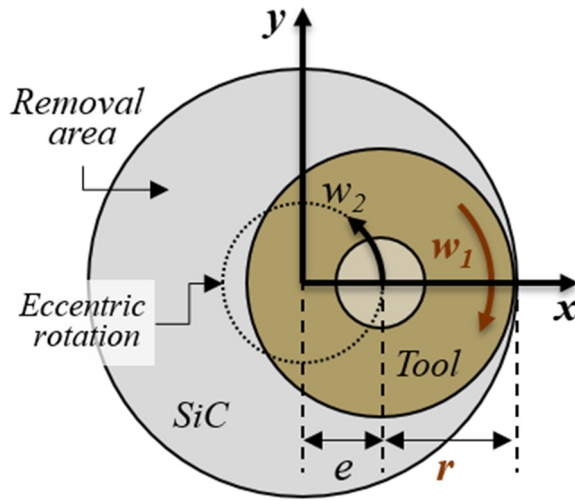


**Fig. 15 | Planetary motion model (top view)**

According to the Preston's equation [15], the removal amount is proportional to the tool-work pressure and the relative velocity between tool and workpiece. Both the workpiece surface and tool end are planes, so that a planetary motion model is

suggested during the polishing process. When the self-rotating tool moves on the workpiece surface, the velocity of an arbitrary point between the tool and the surface is determined as follows:
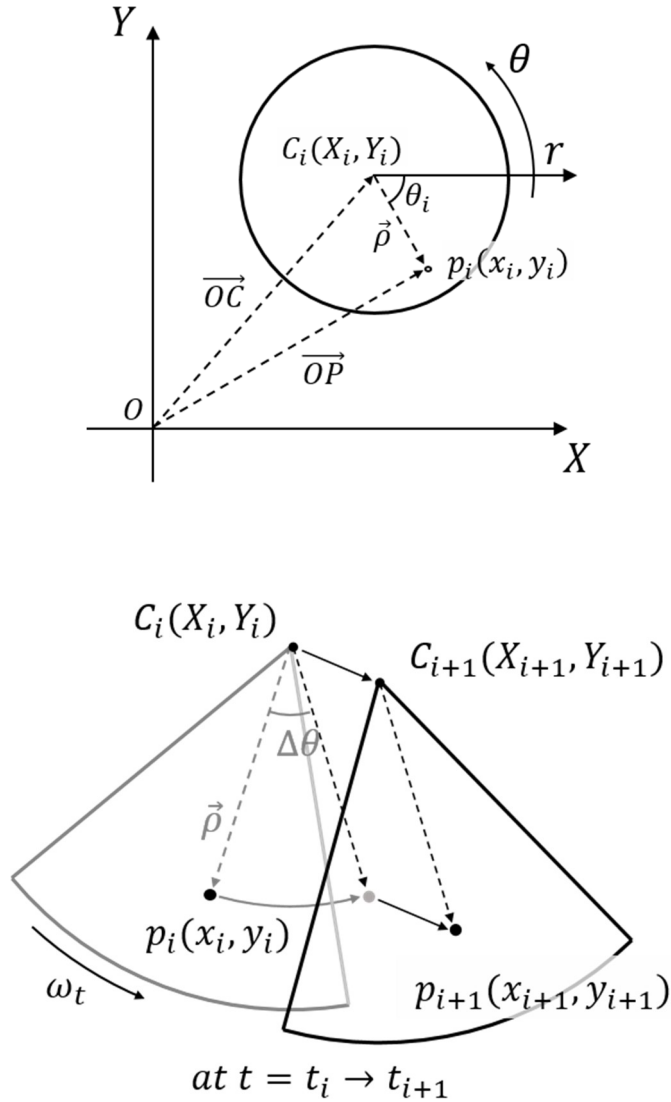


**Fig. 16 | The motion of an arbitrary point in tool-workpiece contact area**

$$V_r = V_{tool} - V_{work}$$

$$V_{work} = 0, \ V_r = V_{tool}$$

$$V_{tool} = V_{tool.rot} + V_{tool.tra}$$

$$\overrightarrow{V_r} = (\vec{\omega} \times \vec{\rho}) + \overrightarrow{V_s}$$

$$\omega = \begin{bmatrix} 0 \\ 0 \\ \omega_t \end{bmatrix}$$

$$\overrightarrow{OP} = \overrightarrow{OC} + \vec{\rho}$$

$$p_i \begin{bmatrix} x_i \\ y_i \\ 0 \end{bmatrix} = \begin{bmatrix} X_i \\ Y_i \\ 0 \end{bmatrix} + \begin{bmatrix} r_p \cos\theta_i \\ r_p \sin\theta_i \\ 0 \end{bmatrix}$$

$$\vec{\rho} = \begin{bmatrix} r_p \cos\theta_i \\ r_p \sin\theta_i \\ 0 \end{bmatrix}, r_p = |\vec{\rho}| = \sqrt{(x_i - X_i)^2 + (y_i - Y_i)^2}, 3.5 < r_p < 15 \text{ mm}$$

$$\overrightarrow{V_s} = \begin{bmatrix} v_X \\ v_Y \\ 0 \end{bmatrix} = \begin{bmatrix} v_s \cos\left(\tan^{-1} \frac{Y_{i+1}-Y_i}{X_{i+1}-X_i}\right) \\ v_s \sin\left(\tan^{-1} \frac{Y_{i+1}-Y_i}{X_{i+1}-X_i}\right) \\ 0 \end{bmatrix}, v_s = |\overrightarrow{V_s}| = \sqrt{v_X^2 + v_Y^2}$$

**Eq. 6 | Relative velocity of planetary motion model**

where $\omega_t$ and $|\overrightarrow{V_s}|$ are the self-rotating spindle speed and tool motion feed rate, respectively.

## 2.3.  Removal Mechanism of Laser Assisted Polishing

Three modes of material removal mechanism are represented in Fig. 17. In the first mode, a mechanical abrasion-based material removal was carried out on the surface with free abrasives rolling and scratching in a typical polishing process. In the second

mode of crack propagation and elongation, cracks were generated, and weak edges were broken by laser irradiation. In this mode, the surface layer was also oxidized, which decreased the local surface hardness and eased the removal process. In the third mode of stress corrosion, free abrasives were stuck into the cracks and when a downward pressure was applied for polishing, the stuck abrasives (red dashed in Fig. 17) increased the lateral stress. In such a situation, the number of active abrasives as well as the contact area of the abrasives with the surface increased at the actual material removal site. In addition, the cracks on the surface decreased the local hardness of the material, which could result in an improvement in the process of material removal.
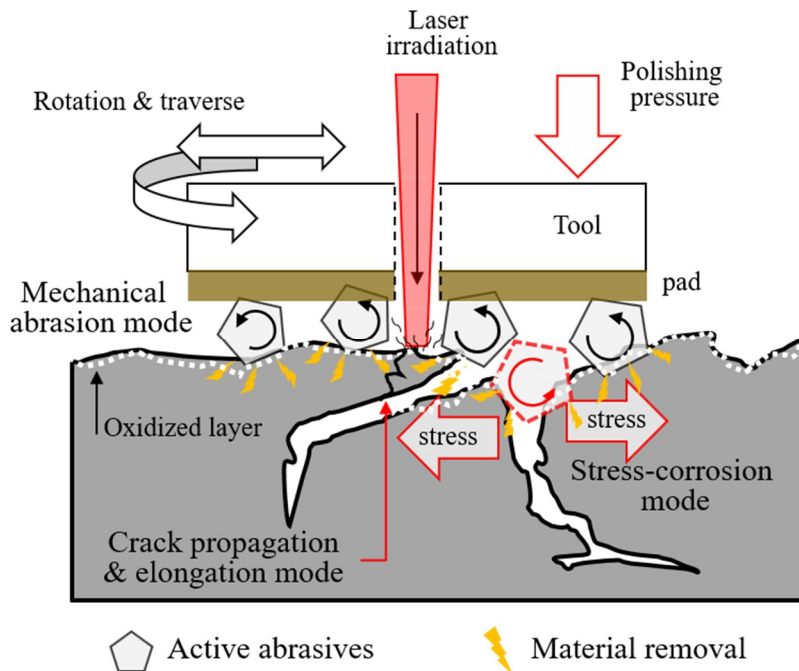


**Fig. 17 | Material removal mechanism of hybrid laser-polishing process**

# Chapter 3. Hybrid Laser-Polishing Machine

## 3.1. System Development

3D model of a three-axis polishing machine was constructed as shown in Fig. 18. The system contains the gantry type of motion stage, consisting of three linear guides and one ball-screwed stage, viz, one linear guide is for X-axis, two synchronous linear guides for Y-axis and the ball-screwed for Z-axis. X- and Z- axes are attached together covering XZ plane. A spindle is attached to the X-axis dependent Z-axis, and the slurry reservoir bed is attached to Y-axis, covering full 3D motion.
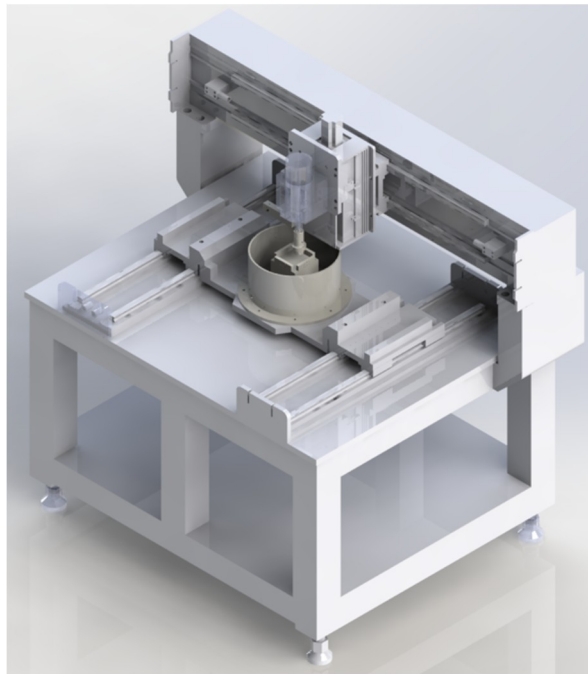


**Fig. 18 | 3D rendering image of the system**

In order to assess the structural stability for the resonance and chatter vibration of the system, modal analysis was conducted in the various periods where it will naturally resonate in frequency domain. The model contains 182,753 nodes and 80,801 elements. As the boundary condition, the bottom part of the system that touches the ground was fixed so as not to move. Considering the normal and sheer force of the spindle and workpiece during polishing, a maximum load of 1,000 N was applied to all directions of the X-, Y- and Z-axes.

As shown in Fig. 19, the natural frequencies were evaluated from 53.30 Hz at the 1st mode to 173.2 Hz at the 6th mode. The maximum deformation of 0.89 mm was obtained at the 1st mode which is the most important. The maximum rotational speed of the spindle in this system is 12,000 RPM and its resonant frequency is approximately 200 Hz, so that 53.30 Hz at the 1st mode was suggested to be stable.

**Table 7 | Result of modal analysis for the system**

|  | Natural Freq. [Hz] | Max. deformation [mm] |
|---|---|---|
| 1st mode | 53.30 | 0.894 |
| 2nd mode | 56.55 | 0.866 |
| 3rd mode | 83.48 | 1.206 |
| 4th mode | 144.6 | 2.201 |
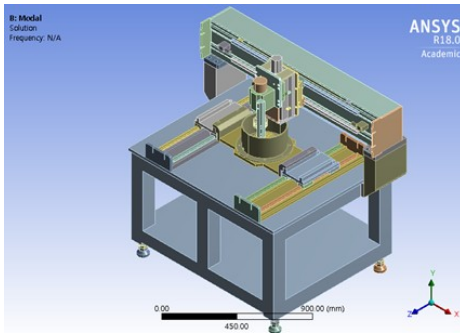
182,753 nodes
80,801 elements

Model
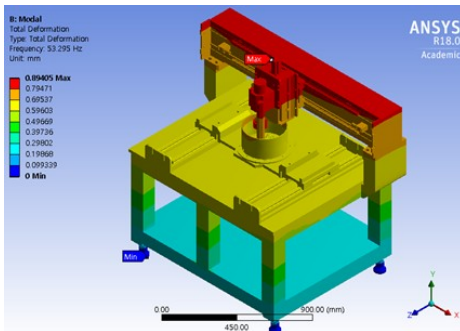


1st mode deformation
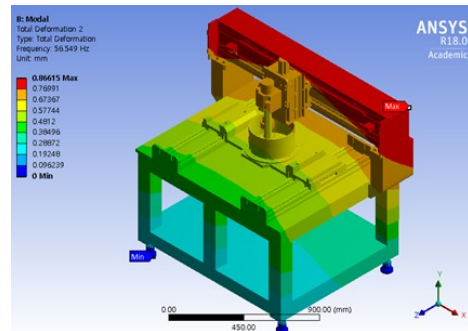


2nd mode deformation
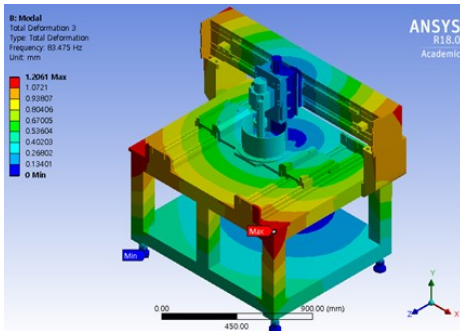


3rd mode deformation
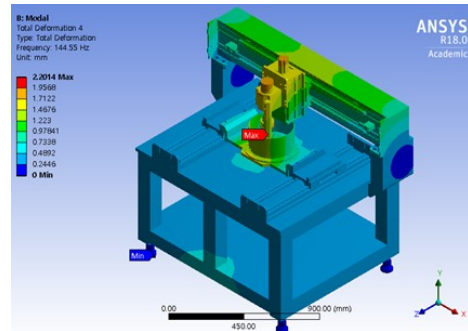


4th mode deformation

**Fig. 19 | Natural frequency modal analysis of the system**

33

The hybrid system was set up as shown in Fig. 21. First, the simple three-axis polishing machine was set up which consisted of a three-axis motion stage, a spindle, and slurry circulation system. A dynamometer was installed underneath the bed on which a workpiece was fixed as shown in Fig. 20, to measure the polishing pressure. When the tool was in contact with the workpiece, the polishing pressure was controlled by driving the Z-axis up/down using a feedback signal from the dynamometer. A $CO_2$ laser source was installed and integrated with the polishing machine using three 45- degree mirrors. A laser beam irradiated an X-axis dependent mirror M1 and was then reflected onto an XZ dependent mirror M2, which covers the complete three-axis movement of the workpiece surface, facilitating the LaPol process. For polishing the SiC surface, an elastomer made of Polydimethylsiloxane (PDMS) and a polyurethane pad of thickness 1.5 mm were attached to the bottom of the tool. Specifications of parts in experimental apparatus were listed in Table 8.
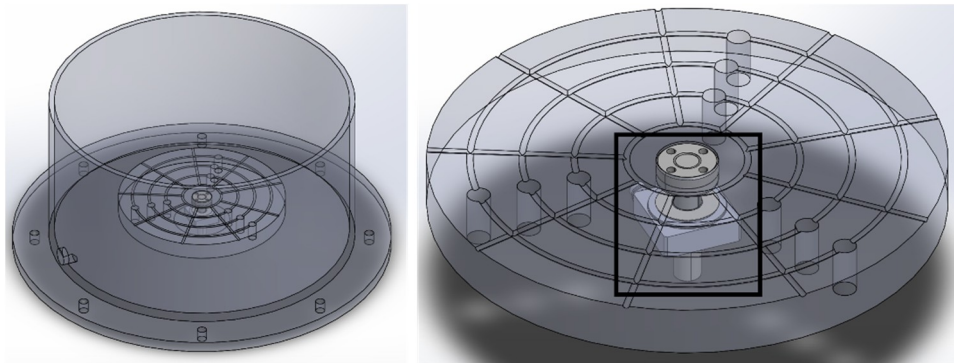


**Fig. 20 | Dynamometer underneath work bed in slurry reservoir**
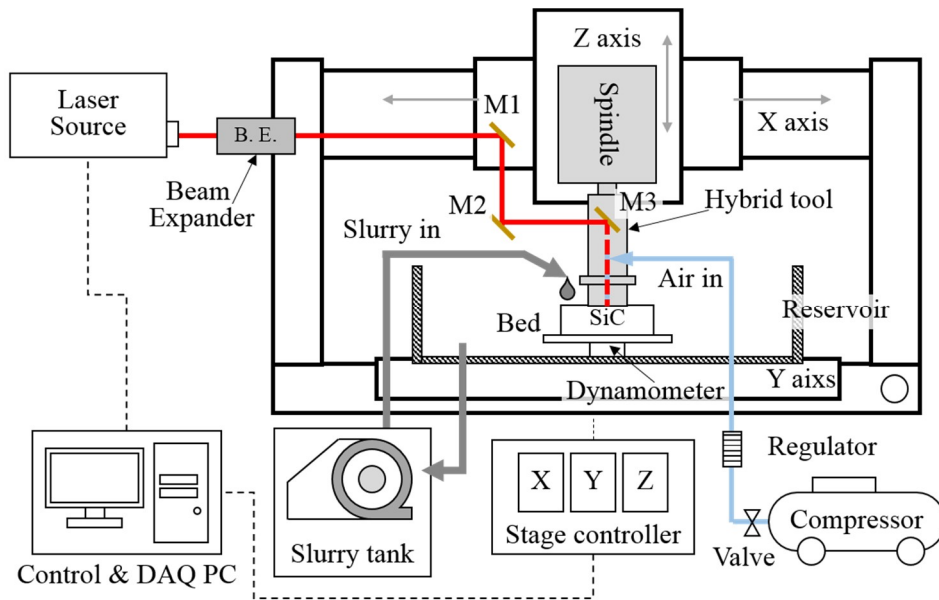
(a) Schematic diagram
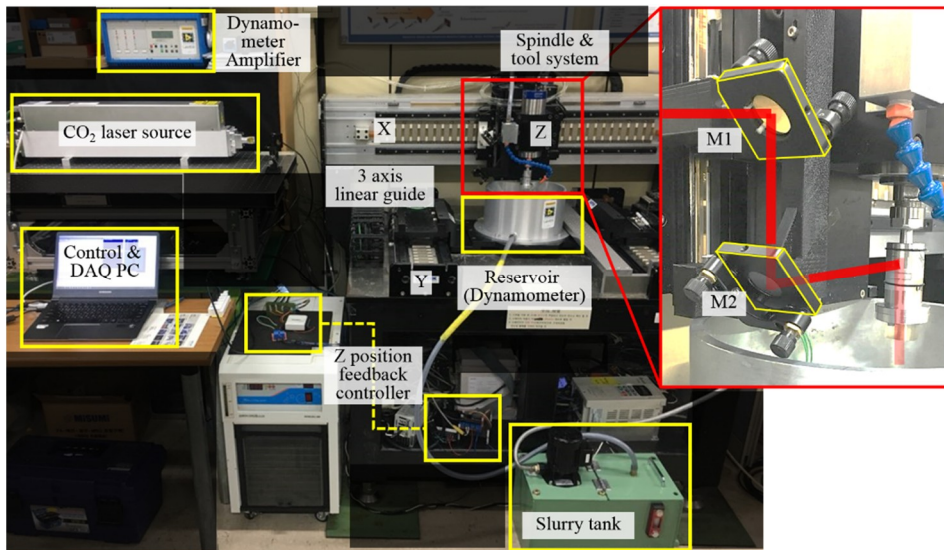


(b) Photograph

**Fig. 21 | Experimental apparatus**

**Table 8 | Specifications of parts in experimental apparatus**

| Part name (model, maker) | Specification |
|---|---|
| Three-axis motion stage (JTM-30 / JTMZ20-30, Justek Inc., Korea) | Resolution: 1 μm (encoder)<br>Accuracy: 2 μm / 4 μm<br>Repeatability: ±0.5 μm<br>Z Max. holding torque: 0.83 Nm |
| Motion controller (Clipper, DeltaTau, USA) | 4 axis Turbo PMAC2<br>12-bit filtered DAC<br>PID servo algorithm |
| Spindle (SW80-1213-SK10, SAMWOO hitech, Korea) | Motor power: 1.3 kW<br>Speed: 12,000 RPM<br>Torque: 1.1 Nm |
| Slurry pump (KTF 25/170, Brinkmann Pumps, Germany) | Type: Plastic, Immersion<br>Motor power 0.045 kW<br>Lift: 3 m<br>Output: 25 L/min |
| Laser source (CR100, Nanjing CRD Laser Co, Ltd, China) | Source: $CO_2$<br>Wavelength: 10.6 μm<br>Power: 100 W<br>Type: Continuous wave<br>Beam mode: $TEM_{00}$ (Gaussian)<br>Beam diameter: 150 μm<br>Focus length: 50.8 mm |
| Chiller (for spindle and laser source) (DLC-1000, Dawoncooler, Korea) | Cooling capacity: 1,000 kcal/h<br>Flow rate: 10 L/min |
| Dynamometer (Type 9251A, Kistler, Switzerland) | Range: -5.0 ~ 5.0 kN<br>Sensitivity: -4 pC/N<br>Resolution: 1 μN |
| Powermeter (PAC-3200, SIEMENS, Germany) | Max. 3-phase, 50/60 Hz<br>400 V AC Phase/N<br>0.01 to 1.2 AC A per Phase<br>64 samples / cycle at 60 Hz |

The beam was focused on the SiC surface through the custom-made hybrid tool (Fig. 22), by means of another 45- degree mirror M3 and a focusing lens of focal length 50.8 mm integrated inside the rotating tool. The duty cycle and pulse width

of the laser beam was controlled to synchronously irradiate it through the rotating tool. The cylindrical tool had two lateral, half-penetrated holes, one for the laser beam and the other for the assist gas. The two holes were joined together to a vertical hole for merging the beam and the gas. The gas instantly pushed the slurry out from the spot when the laser was irradiated on the surface, which made it possible for the beam to be irradiated on the slurry environment during polishing.

## 3.2.    Force Feedback Z-Position Control System

In order to keep the tool pressure constant during polishing process, force feedback Z-position control system was developed by using Labview and PLC programming as shown in Fig. 24. First, the reference force the user wants to operate with was set up. During polishing, the output force signal prom the sensor was compared to the reference force. Once the output force exceeds the upper threshold, it generates system input to the stage controller for the Z-axis to move up, *vice versa*, in real time.
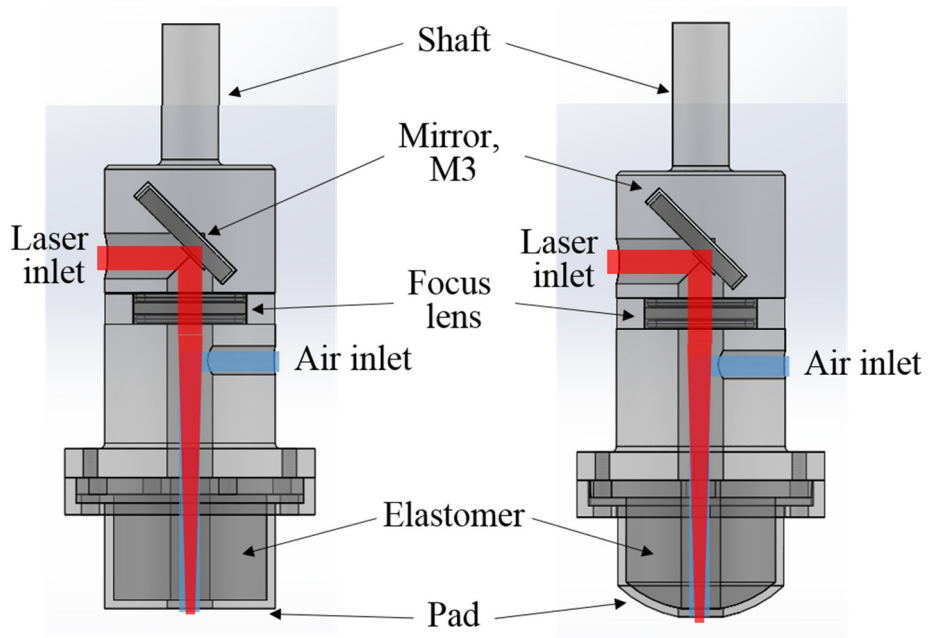
**Fig. 22 | Design of flat (left) and ball-nose (right) polishing tool**
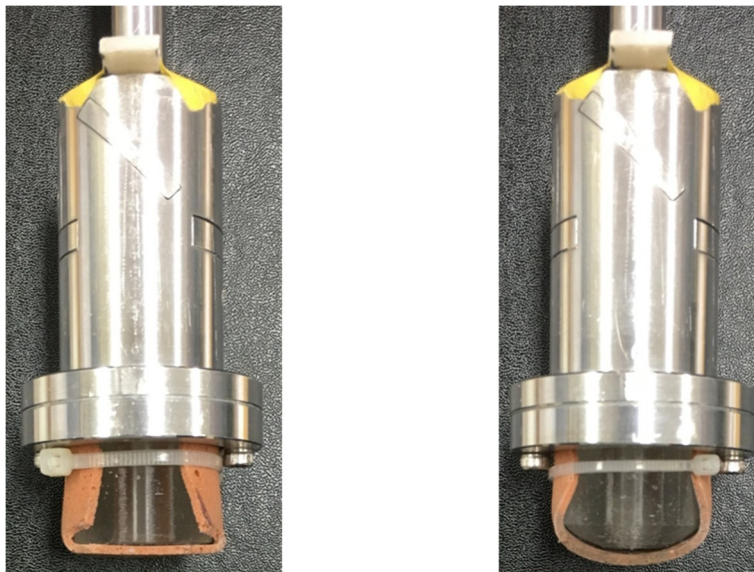


**Fig. 23 | Photograph of flat (left) and ball-nose (right) polishing tool**
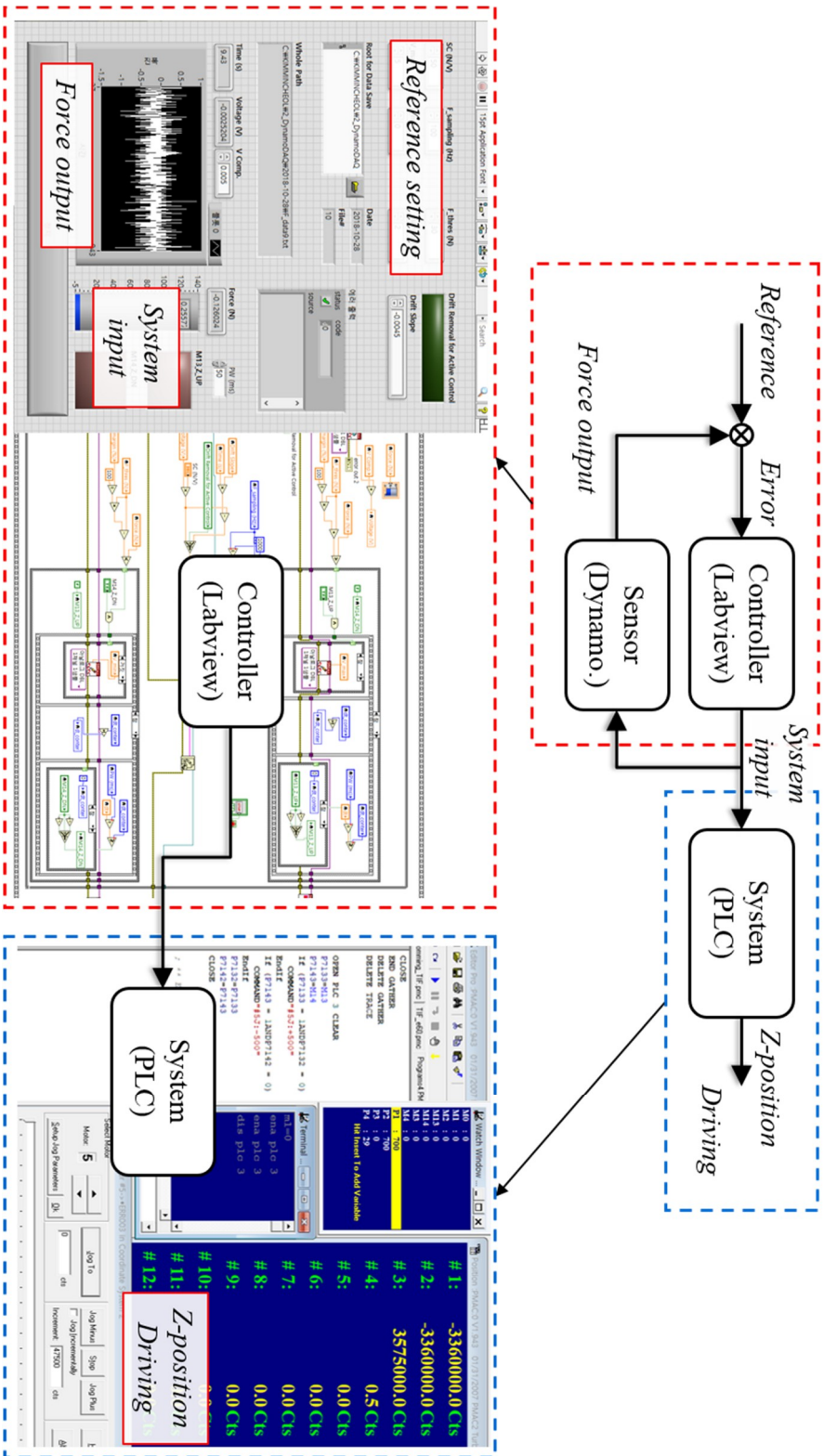
**Fig. 24 | Force feedback Z-position control system**

## 3.3. Spindle Energy Monitoring System

It is very difficult to measure or predict the characteristics of the workpiece surface in the middle of the polishing process. In order to predict the surface form of the workpiece from the electric power consumption, spindle power monitoring system was developed by installing the electric power meter onto the spindle electric power lines. The schematic paradigm was illustrated in Fig. 25. As the polishing tools moves over the workpiece surface, the spindle load changes depending on the surface form, which affects the electric power consumption of the spindle [80, 81]. By mapping the spindle power consumption to the 2D tool position (Fig. 26), it was suggested the surface form will be predictable (Fig. 27).
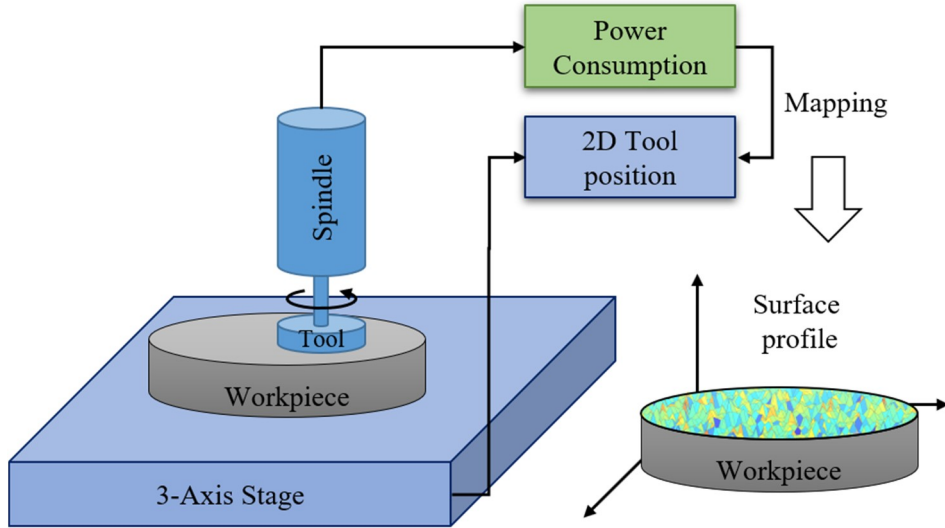


**Fig. 25 | Experimental paradigm of surface prediction**
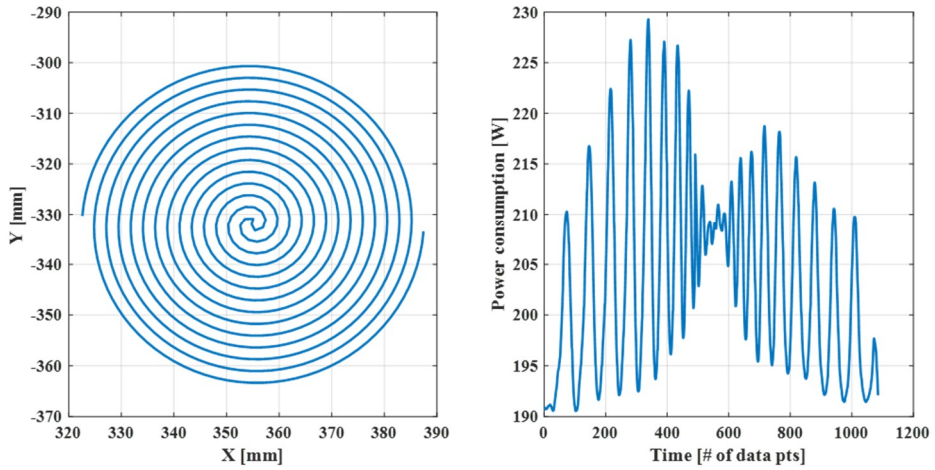
**Fig. 26 | 2D Tool position and respective power consumption**
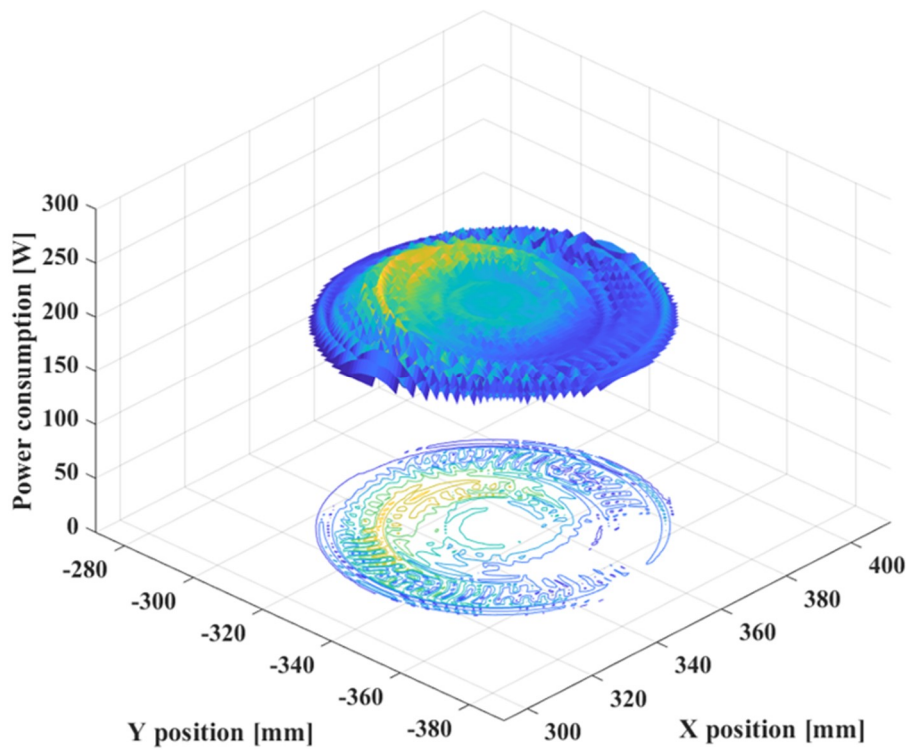


**Fig. 27 | Mapping of 2D tool position and respective consmption**

## 3.4. Tool Path Generator

The tool path generator was developed in Matlab [82]. The input parameter was the type of tool path, such as raster or spiral, the origin of the hybrid machine and the radius of workpiece. Also, the raster distance which is the distance between the subsequent paths (raster distance) is needed for raster tool path. Since the spiral tool path was generated in the polar coordinated system, the theta increment needs to be determined in spiral tool path. Also, the number of the Archimedean spiral rotations from edge to center should be determined. While the tool is going to the center, the distance between to subsequent points are getting shorter and shorter, remaining lots of points at the center. This may cause the problem on the compatibility of machine movement, where the system is operated based on the linear movement from one point to the next point with the feed rate, acceleration and deceleration. Thus, the distance between two subsequent points are set to be identical, so that the feed rate of the machine that the user ordered is obeyed. The tool path is then converted to the G-code that the machine can read and follow. The generator provides only one cycle of the tool path, and the machine controller execute it repeatedly (see Appx. 1).
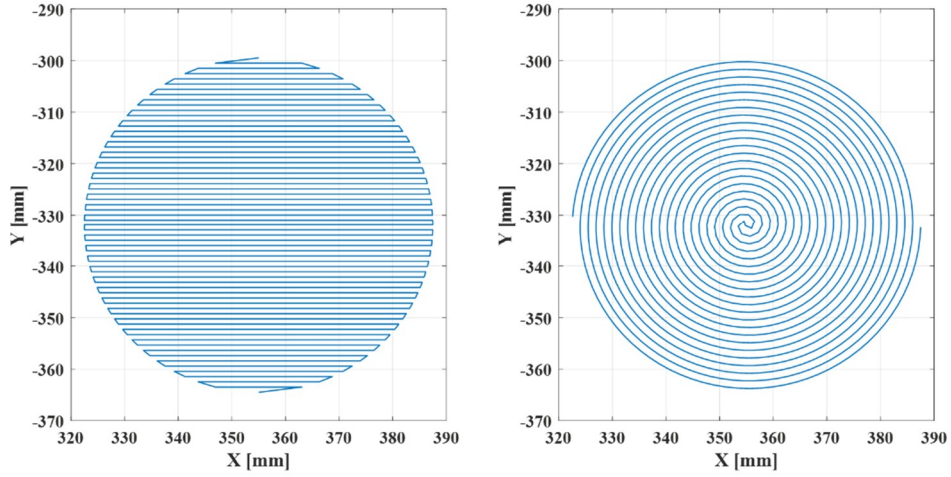
**Fig. 28 | The generated tool path; raster (left) and spiral (right)**

## 3.5. Laser Beam Machining Profile

In order to obtain the 3D removal profile of $CO_2$ laser beam for SiC surface, a single back-and-force travel of laser beam irradiation was made on SiC surface with the parameters listed in Table 9. The raster width varied from 20 to 150 μm. The corresponding federate was calculated (Eq. 7) for the circular area with diameter of 5 mm to take 20 sec covering whole raster scanning as shown in Fig. 29. The shorter the raster width of the beam path is used, the longer the total travel length it takes to cover the whole area. The total travel length of the tool path was calculated for the circular area of 5 mm in diameter as shown in Fig. 30, where the raster widths of 20, 50, 100 and 150 μm were chosen (red markers in Fig. 30) and the corresponding feed rate was obtained as listed in Table 10.
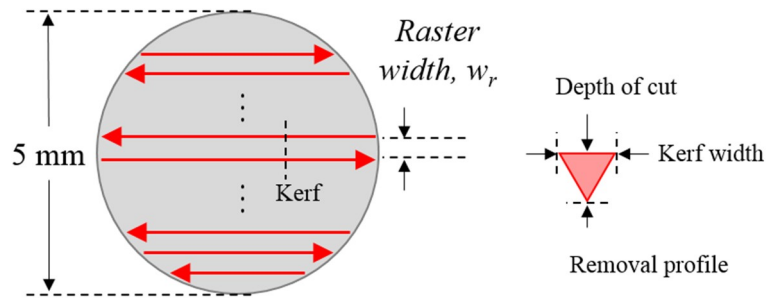
**Fig. 29 | Laser beam path of circular area**

**Table 9 | Parameters for laser processing**

| Laser beam irradiation | |
|---|---|
| Beam path | Raster (50 ~ 250 μm in width) |
| Output power | 94.3 W (=30% duty ratio) |
| Feed rate | 6.64 ~ 49.47 mm/s |
| Assist gas | Compressed air |
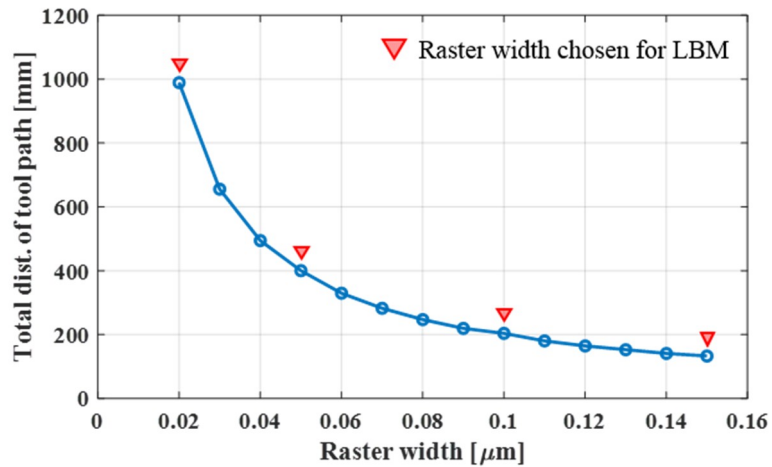


**Fig. 30 | Relationship between raster width and total distance of path**

$$T_{machining} = \frac{\sum L_{Path}}{feed\ rate} = K = 20\ sec$$

$$feed\ rate = \frac{\sum L_{Path}}{20\ sec}$$

**Eq. 7 | Feed rate calculation for each raster width**

**Table 10 | Raster width and corresponding feed rate**

| # | Raster width [μm] | Total dist. of tool path [mm] | Feed rate [mm/s] |
|---|---|---|---|
| 1 | 20 | 989.3 | 49.47 |
| 2 | 50 | 400.1 | 20.01 |
| 3 | 100 | 203.6 | 10.18 |
| 4 | 150 | 132.8 | 6.640 |

The laser beam machining profile of the four cases were obtained as shown in Fig. 31. When using the raster width of 20 μm, the reciprocating tool motion seemed as if the tool path was single travel, resulting in no separation of the kerf. The back-and-forth motion makes the beam overlapped by approximately 67% with the beam waist of 150 μm and the raster width of 50 μm, laser beam started to generate the kerf separation. With increasing raster width, the kerf separation tended to increase. This might result from the Gaussian distribution of the laser power density, and the power density at the beam boundary was not enough to remove the SiC.

The calculated feed rate was inverse relationship with the raster width. In the

material point of view, the slower feed rate of laser beam irradiation causes the more laser energy absorption per unite area. When using the feed rate of 49.47 mm/s, maximum removal depth was approximately 5 μm, which increased up to 12.5 μm with the feed rate of 6.64 mm/s.
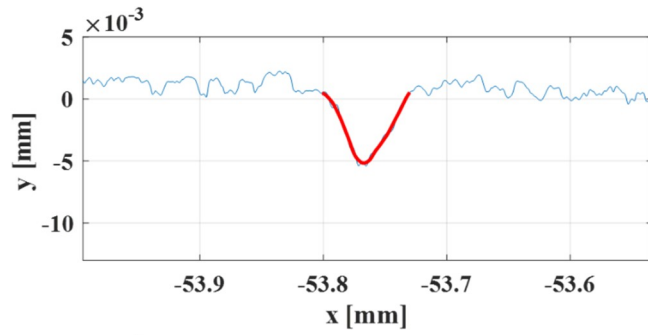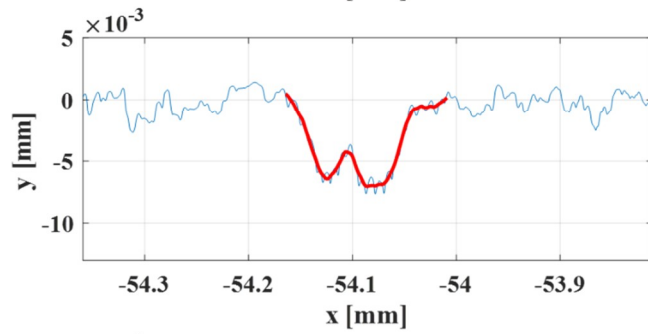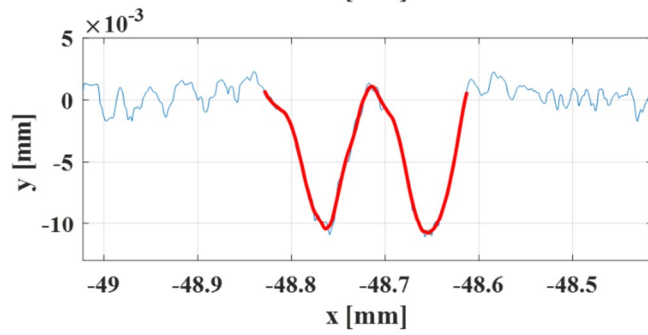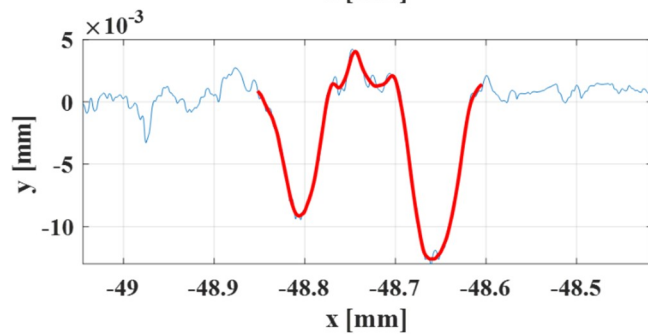
**Fig. 31 | Single back-and-force travel (5mm each) and kerf profile**
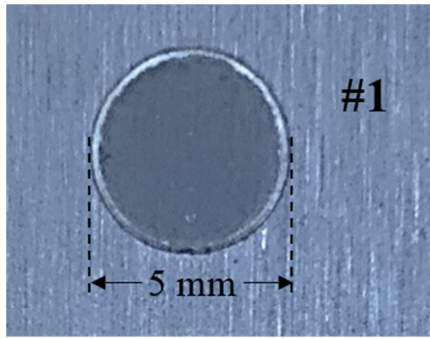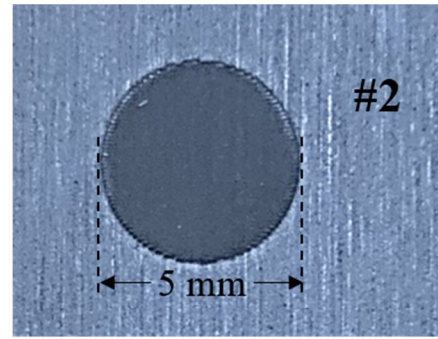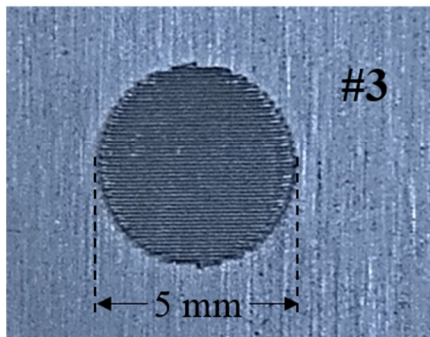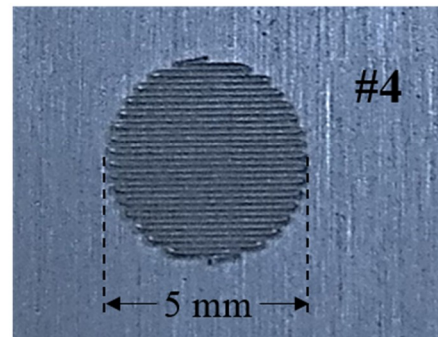
**Fig. 32 | Laser beam irradiation of circular area with raster path**

**Table 11 | Depth of cut with the raster width and the corresponding feed rate**

| # | Raster width [μm] | Feed rate [mm/s] | Depth of cut [μm] |
|---|---|---|---|
| 1 | 20 | 49.47 | 7.7 |
| 2 | 50 | 20.01 | 3.4 |
| 3 | 100 | 10.18 | 0.8 |
| 4 | 150 | 6.64 | 0.0 |

## 3.6. Polishing Tool Influence Function (TIF)

According to the Preston's equation, basic characteristics of the TIF were adopted as follows [83]:

> ➢ A rotational-symmetric and smooth function
>
> ➢ Central peak removal, decreasing with increase in radius
>
> ➢ Zero removal rate at the maximum radius
>
> ➢ Zero slope at the center and outer most region

In order to obtain the TIF of the hybrid tool, the polishing process was conducted with the parameters listed in Table 12. The TIF of the system was shown in Fig. 33, resulting in the maximum removal rate of 0.105 μm/min at the center.

**Table 12 | Parameters for TIF**

| Parameters | |
|---|---|
| Tool radius | $r = 15$ mm |
| Tool rotation | $w_1 = 1200$ RPM |
| Eccentricity | $e = 0.6\ r = 9$ mm |
| Eccentric rotation | $w_1 = 26.5$ RPM (feed rate = 25 mm/s) |
| Polishing pressure | $P = 45.7$ kPa (F=30 N) |
| Polishing time | 30 min |
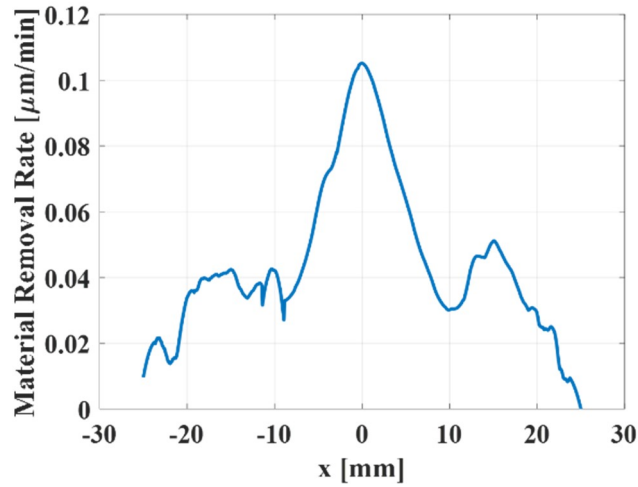
**Fig. 33 | Influence function of the hybrid tool**

## 3.7. Multi Process of Hybrid Machine

Using the hybrid $CO_2$ laser-polishing machine, as depicted in Fig. 34 - Fig. 36, three processes were available on a single machining platform for the material removal on the SiC sample: (i) laser beam irradiation (Fig. 34), which cracked, oxidized, and evaporated the surface [44], (ii) mechanical polishing (Fig. 35), also known as free abrasive machining, where abrasive particles or grains cut away the material as governed by Preston's equation [15], and (iii) laser assisted polishing (Fig. 36), which is the hybrid process where the laser beam is synchronously irradiated through the rotating tool during the polishing process, so that the polishing process is combined with the laser irradiation in order to continuously and simultaneously produce the crack initiation and oxidation by the laser and material removal by polishing.

50
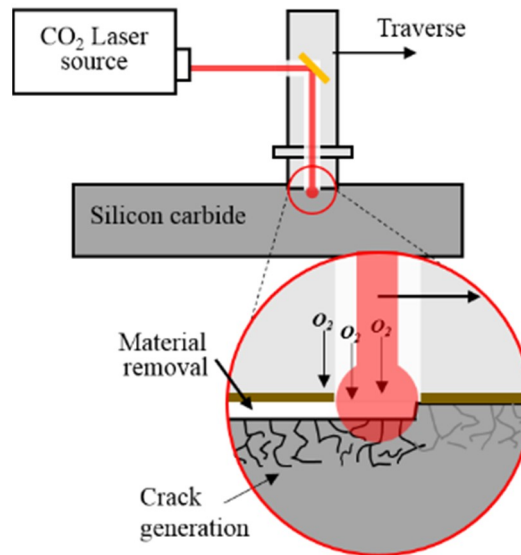
**Fig. 34 | The hybrid CO₂ laser-polishing process: Laser beam machining**
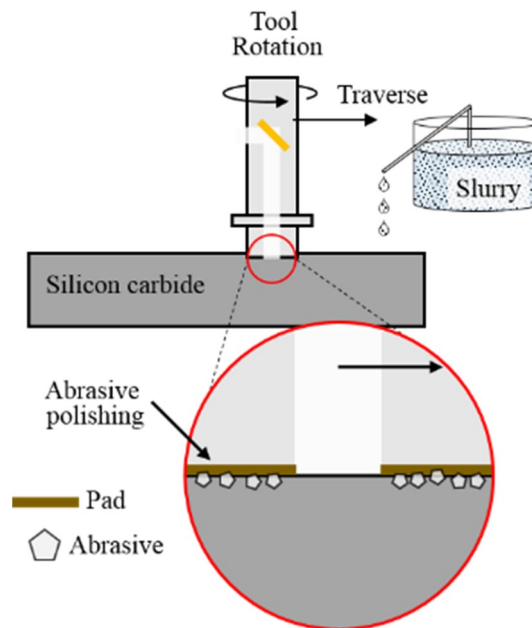


**Fig. 35 | The hybrid CO₂ laser-polishing process: Mechanical polishing**
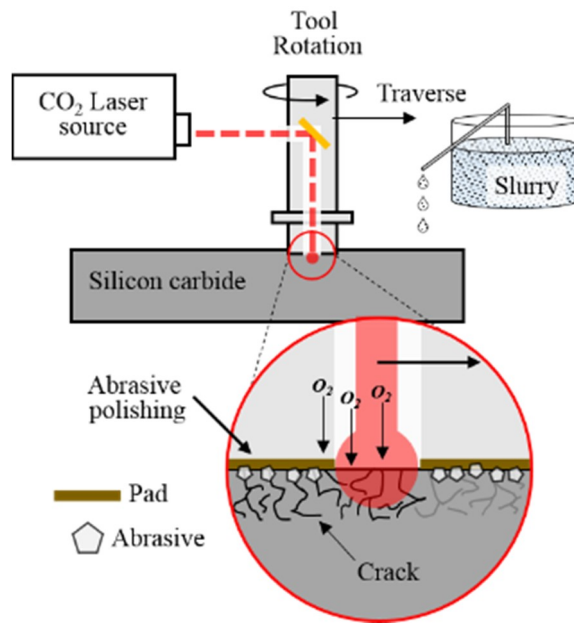
**Fig. 36 | The hybrid CO₂ laser-polishing process: Laser assisted polishing**

# Chapter 4. Laser Induced Surface Modification

## 4.1.    Surface Identification Method

The lateral crack length and vertical depth were characterized as shown in Fig. 37. The lateral crack length was calculated by summing all the crack lengths on top of the surface within $130 \times 100 \ \mu m^2$ area of the field of view (FOV) seen through the optical microscope (OM) (BX53M, Olympus Corporation, Japan) at x1,000 magnification. As shown in Fig. 38, the crack depth was examined by using the bonded interface sectioning method [84, 85], where two identical SiC workpieces, one side of each of which was polished, were glued together with an epoxy resin adhesive so that the polished surfaces were facing each other. The laser beam was irradiated on top of the bonded workpiece. The workpieces were then separated by melting the adhesive and the interfaces were cleaned and polished again to measure the depth of the crack. After the laser induced generation of the crack, the Vickers hardness test was conducted by using a portable indentation system (AIS-3000, FRONTICS, Inc., Korea) and the surface roughness was measured by a surface profiler (SJ-410, Mitutoyo, Japan) and optical profiler based on coherent correlation interferometer (CCI HD, Taylor Hobson, U.K.) installed in Korea Basic Science Institute (KBSI)
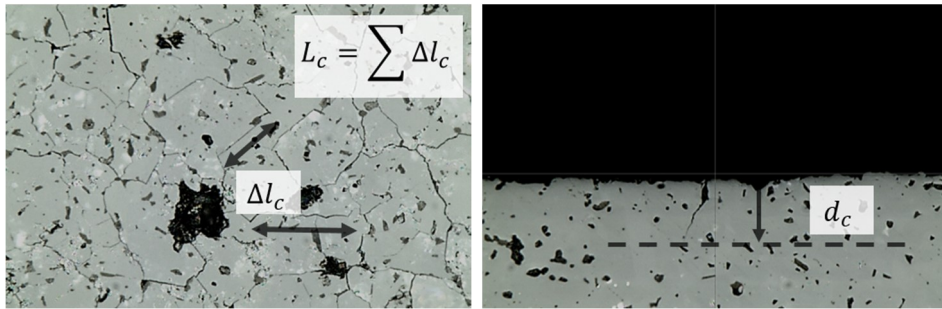
**Fig. 37 | crack length (left) and depth (right) measurement**
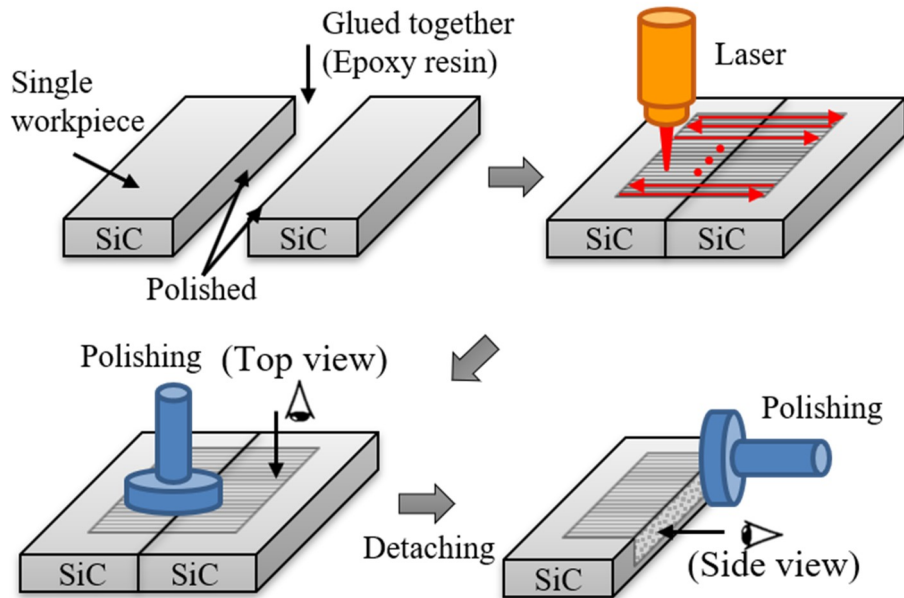


**Fig. 38 | Bonded interface sectioning method**

The X-ray diffractometer (XRD) (SmartLab, Rigaku, Japan) and X-ray photoemission spectroscope (XPS) (SIGMA PROBE, ThermoFisher Scientific, U.K.) were used to investigate the surface modification before and after the laser irradiation

with regard to the crystalline structure and elemental composition, respectively. The XPS analysis was performed rapidly with high energy density of the X-ray to scan the broad range of binding energy, after which a detailed investigation of the outstanding peaks of the spectra was carried out with low energy density. Energy-dispersive X-ray spectroscopy (EDS) analysis was also conducted only for the as-received sample in preparation.

## 4.2. Preparation of SiC Sample

The SiC used in the current study was fabricated by hot-press sintering process, namely hot-press sintered SiC (HP-SiC) with a subsequent grinding process for satisfying the figure dimension and surface roughness (Dandan Co. ltd., Korea). In order to investigate the crystalline structure of the as-received HP-SiC, XRD analysis was conducted as shown in Fig. 39. Several apparent peaks represented by Bragg's index [86] were observed, which results in the crystalline structure of the SiC was hexagonal 6H major (see Table 13).
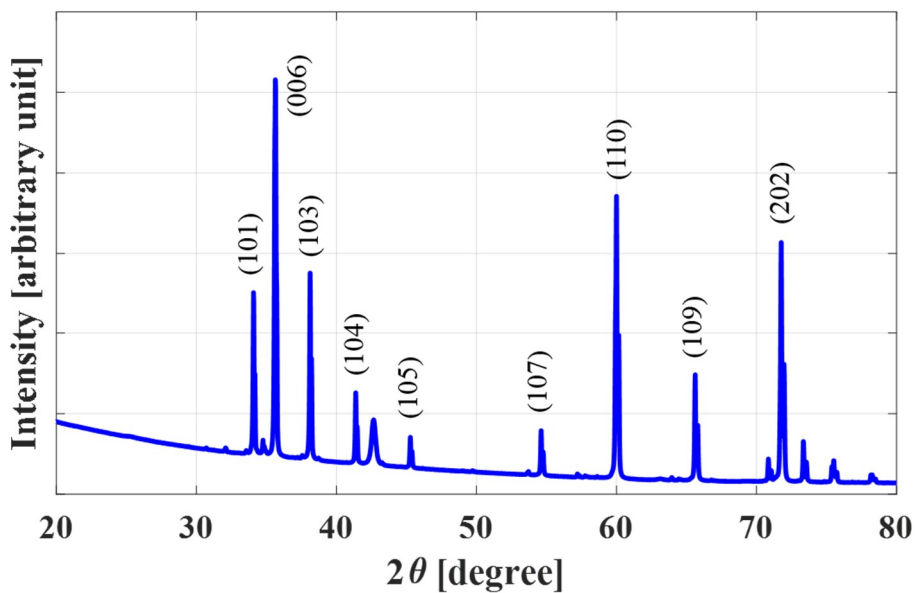
**Fig. 39 | XRD result of HP-SiC (as-received)**

**Table 13 | XRD results of HP-SiC in detail**

| 2-Theta (deg.) | Height (cps) | Phase name |
|---|---|---|
| 33.56 | 16,600 | Moissanite-4H, syn (1,0,0), alpha-SiC (1,0,1) |
| 34.08 | 813,613 | Moissanite-6H (1,0,1) |
| 34.75 | 55,796 | Moissanite-4H, syn (1,0,1) |
| 34.89 | 22,897 | alpha-SiC (1,0,4) |
| 35.61 | 1,949,485 | Moissanite-6H (0,0,6), Moissanite-4H, syn (0,0,4), alpha-SiC (0,0,15) |
| 37.58 | 10,373 | alpha-SiC (1,0,7) |
| 38.12 | 820,761 | Moissanite-6H (1,0,3), Moissanite-4H, syn (1,0,2) |
| 38.60 | 7,735 | alpha-SiC (0,1,8) |
| 41.38 | 312,103 | Moissanite-6H (1,0,4), alpha-SiC(1,0,10) |

| 2-Theta (deg.) | Height (cps) | Phase name |
|---|---|---|
| 42.62 | 182,251 | Carbon (1,1,-1), alpha-SiC (0,1,11) |
| 43.25 | 9,519 | Moissanite-4H, syn (1,0,3) |
| 45.28 | 134,545 | Moissanite-6H (1,0,5) |
| 49.71 | 6,302 | Moissanite-6H (1,0,6) |
| 54.18 | 1,081 | Carbon (3,1,1), alpha-SiC (0,1,17) |
| 54.61 | 208,049 | Moissanite-6H (1,0,7) |
| 57.19 | 15,673 | Moissanite-4H, syn (1,0,5) |
| 57.79 | 5,027 | Carbon (1,1,-2), alpha-SiC (1,0,19) |
| 59.92 | 476,432 | Moissanite-6H (1,0,8) |
| 59.99 | 1,529,112 | Moissanite-6H (1,1,0), Moissanite-4H, syn (1,1,0), alpha-SiC (0,1,20) |
| 64.47 | 5,933 | Carbon (4,0,2), alpha-SiC (1,0,22) |
| 65.61 | 554,582 | Moissanite-6H (1,0,9), Moissanite-4H, syn (1,0,6) |
| 66.67 | 2,868 | Carbon (5,1,-1), alpha-SiC (0,1,23) |
| 70.84 | 119,302 | Moissanite-6H (2,0,1) |
| 71.76 | 1,300,311 | Moissanite-6H (2,0,2), Moissanite-4H, syn (1,1,4) |
| 73.34 | 227,757 | Moissanite-6H (2,0,3), Moissanite-4H, syn (2,0,2) |
| 75.38 | 85,794 | Moissanite-6H (0,0,12), Carbon (0,2,0) |
| 75.50 | 107,035 | Moissanite-6H (2,0,4) |
| 78.16 | 36,480 | Moissanite-6H (1,0,11) |
| 78.25 | 39,292 | Moissanite-6H (2,0,5) |
| 79.37 | 1,136 | Carbon (0,2,1) |

In order to verify the elemental composition of HP-SiC, XPS analysis was also conducted. The peaks representing silicon and carbon are observed as shown in Fig.

40 and the detailed results were listed in Table 14. The oxygen peak was also observed which might result from the inevitable oxidation during grinding and cleaning in material fabrication process. EDS analysis was also conducted in order to double check the elemental composition of HP-SiC as shown in Fig. 41, and Boron (B) was captured at the the darker area, which turned out to be a sintering agent.

**Table 14 | XPS results of HP-SiC in detail**

| Name | Peak BE | Height CPS | FWHM eV | Area (P) CPS.eV | Atomic % | Q | SF |
|------|---------|-----------|---------|-----------------|----------|---|-----|
| C1s | 284.47 | 3433.54 | 2 | 7305.14 | 26.51 | 1 | 1 |
| C1s | 281.44 | 1806.81 | 1.46 | 2802.67 | 10.17 | 1 | 1 |
| C1s | 282.94 | 509.11 | 2 | 1083.86 | 3.93 | 1 | 1 |
| C1s | 286.37 | 1272.28 | 2 | 2708.61 | 9.83 | 1 | 1 |
| C1s | 288.07 | 549.93 | 2.18 | 1273.3 | 4.62 | 1 | 1 |
| O1s | 531.27 | 4627.34 | 2.03 | 10307.04 | 12.77 | 1 | 2.93 |
| O1s | 532.78 | 3343.76 | 2.04 | 7388.58 | 9.16 | 1 | 2.93 |
| Si2p | 99.53 | 1965.79 | 1.66 | 3469.48 | 15.45 | 1 | 0.817 |
| Si2p | 101.64 | 554.13 | 2 | 1179.71 | 5.25 | 1 | 0.817 |
| Si2p | 103.65 | 242.36 | 2 | 515.96 | 2.3 | 1 | 0.817 |
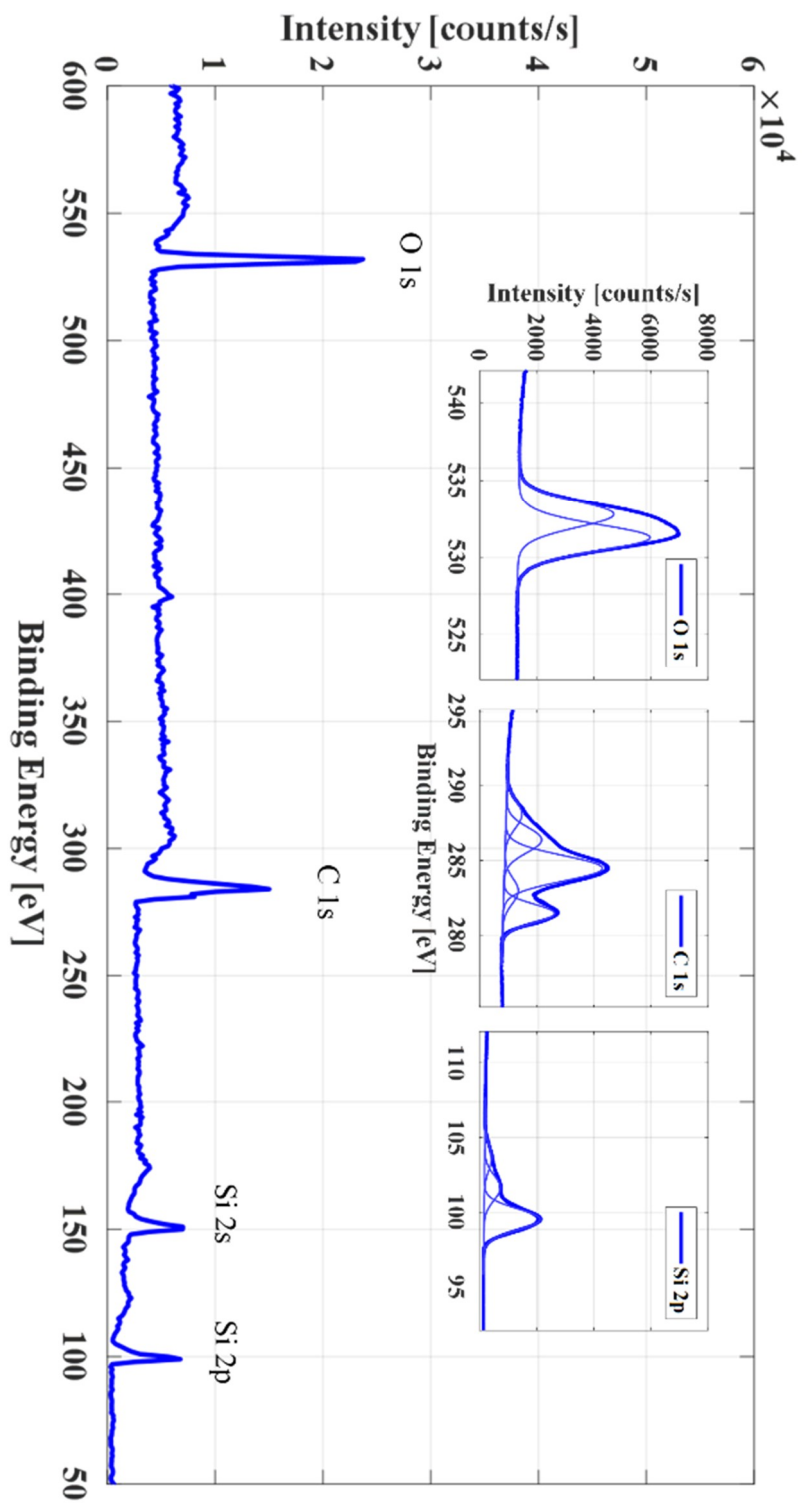
**Fig. 40 | XPS results of HP-SiC (as-received)**

59
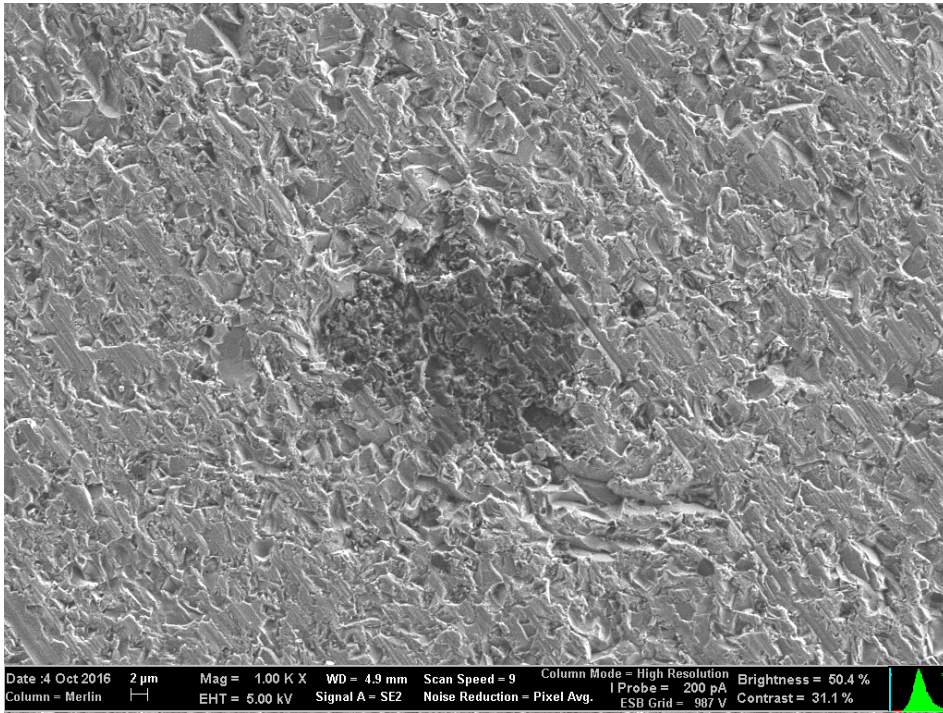
**Fig. 41 | EDS results of HP-SiC (as-received)**

In order to verify whether there is any subsurface crack in the initial material (as-received), one of the samples is polished for 10 min with the parameters listed in Table 15. The equally distributed 15 points on the as-received SiC surface were observed in OM as shown in Fig. 42, where the horizontal ground tool marks were observable in the whole sample surface. It is because that the final surface finishing process was the grinding process for the sample preparation. After 10 min of polishing, the horizontal ground tool marks were apparent with the micro scale pits, originated from the material sintering stage as shown in Fig. 43. However, there is no subsurface cracks, which will be shown in the next section, laser induced cracks.

**Table 15 | Parameters for verifying subsurface damage**

| Polishing | |
|---|---|
| Pressure (Force) | 45.69 kPa (30 N) |
| Tool diameter | 30 mm |
| Rotational speed | 1200 RPM |
| Dwell time | 10 min |
| Feed rate | 25 mm/s |
| Slurry | Diamond and ceria (~1 μm diameter) |
| Pad | Polyurethane (1.5 mm in thickness) |
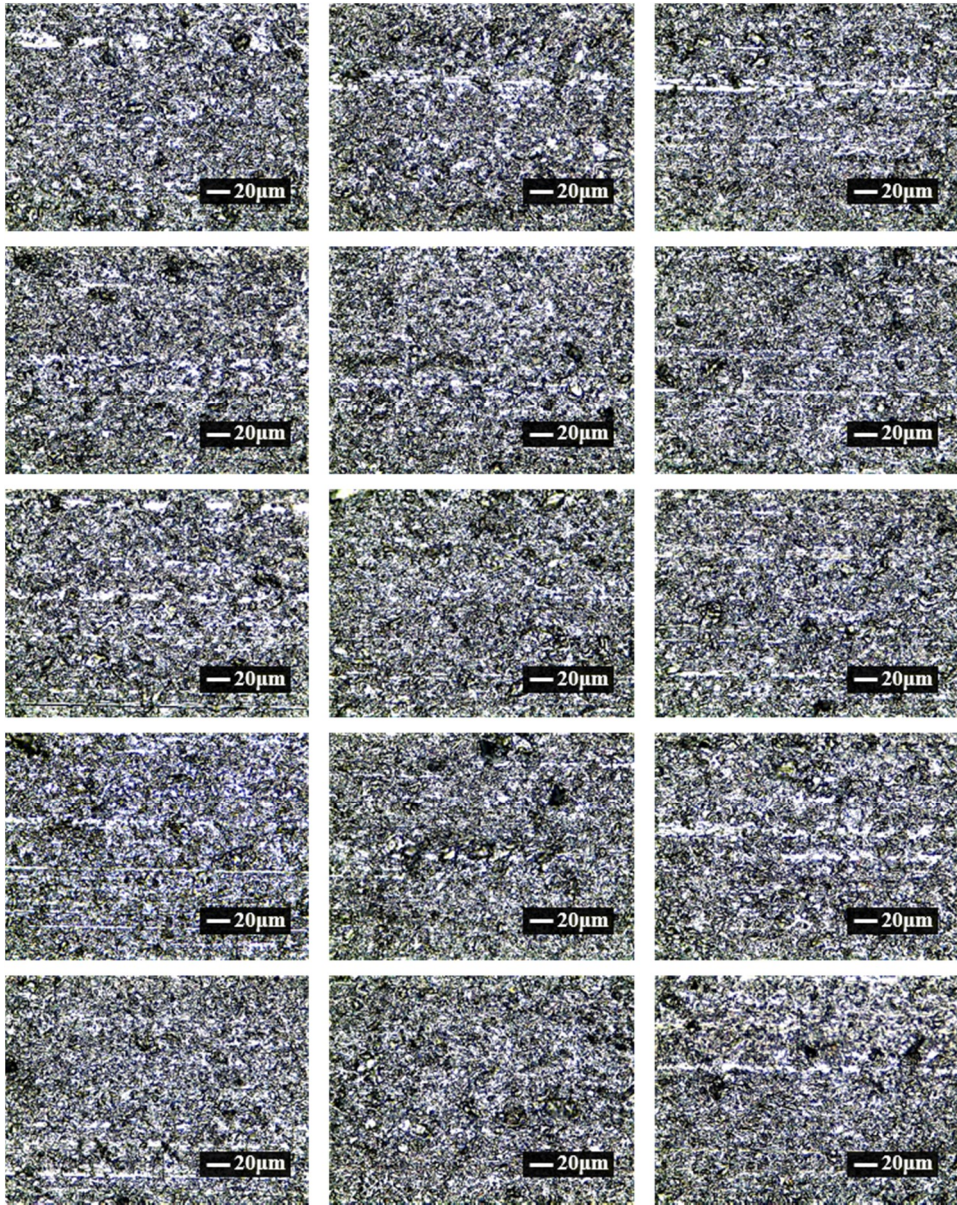
**Fig. 42 | As-received SiC sample surface**
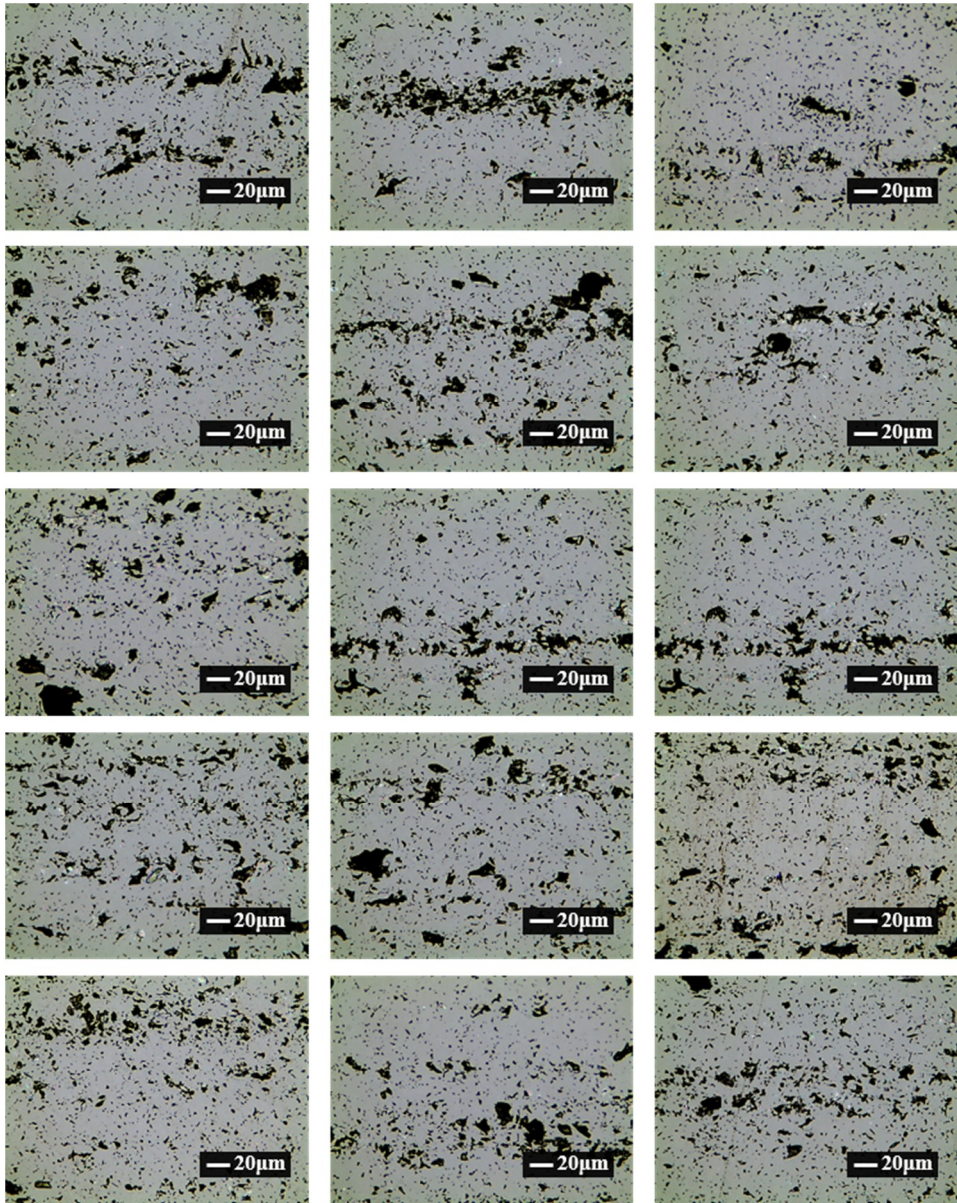
**Fig. 43 | Polished surface of the as-received sample**

**Table 16 | Properties of SiC**

| Silicon carbide | |
|---|---|
| Fabrication process | Hot-press sintering |
| Crystal structure | Hexagonal (6H major), $\alpha$-SiC |
| Density | 3.21 g/cc |
| Modulus of Elasticity | 410 GPa |
| Compressive Strength | 4,600 MPa |
| Fracture toughness | 4.6 MPa-m½ |
| Thermal conductivity | 4.9 W/cm°C |
| Thermal shock resistance | 350 ΔT°C |
| Thermal expansion | 4.7 x $10^{-6}$/°C |

## 4.3. Characterization of Laser Induced Crack

Output power of the laser source varied from 21.8 to 53.8 W to investigate the output power threshold for crack initiation as shown in. The beam was irradiated on SiC surface, whose area of each is $10 \times 10$ mm². As power increases, the laser irradiated area is getting darker as seen in naked eye (Fig. 44, center). Top layer was then polished 10 min to see whether crack generated and how strong the laser output power is enough to initiate cracks. The OM images were shown in Fig. 45. Apparent cracks are observed on the sample with 53.8 W of laser irradiated sample, which looks like a ground with droughtiness. The crack length was measured for varying output power of the laser beam as shown in Fig. 46. The cracks started to appear when more than 30 W of the laser beam was irradiated and were saturated at approximately 40 W of the laser beam.
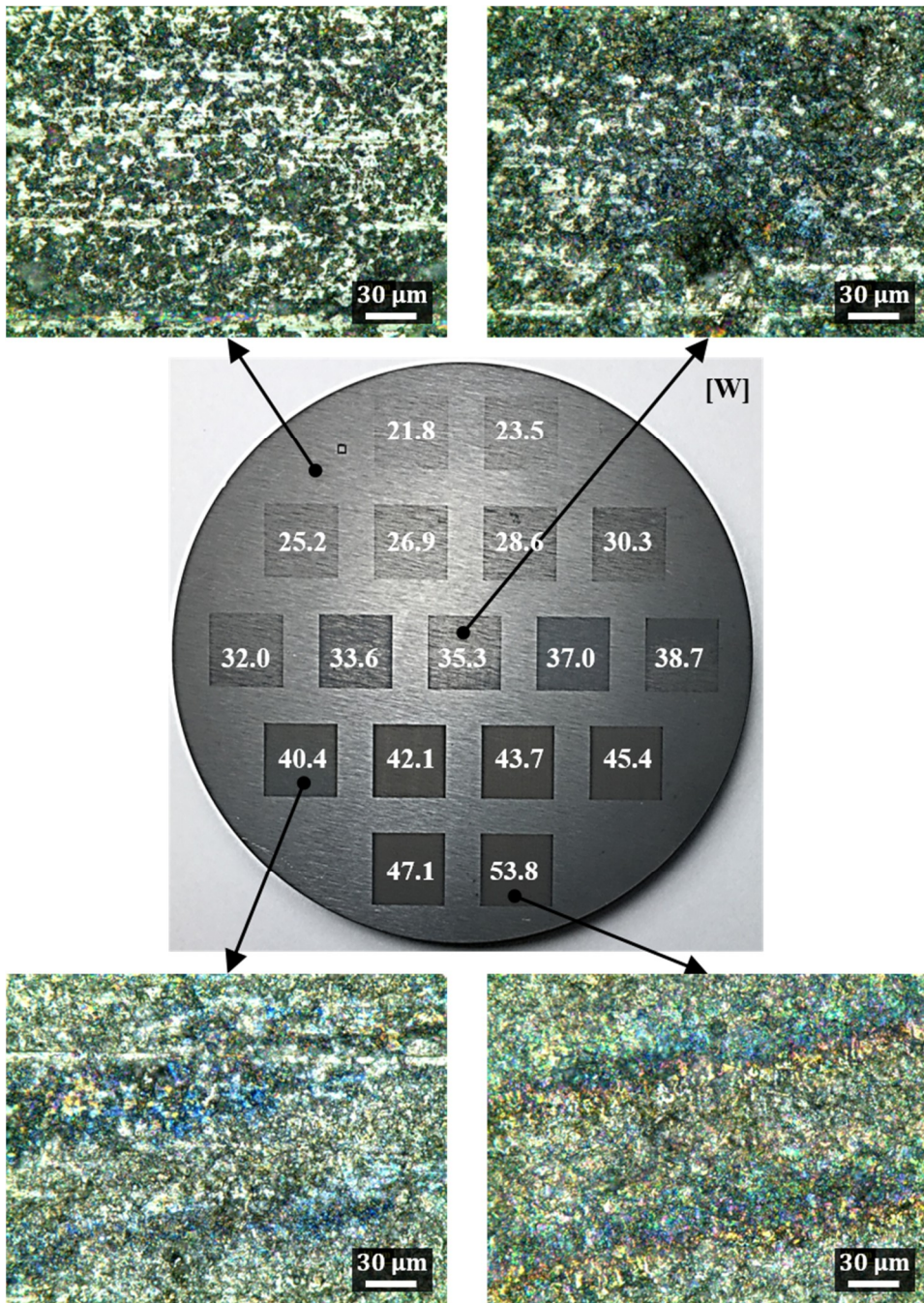
**Fig. 44 | Laser induced SiC surface modification**
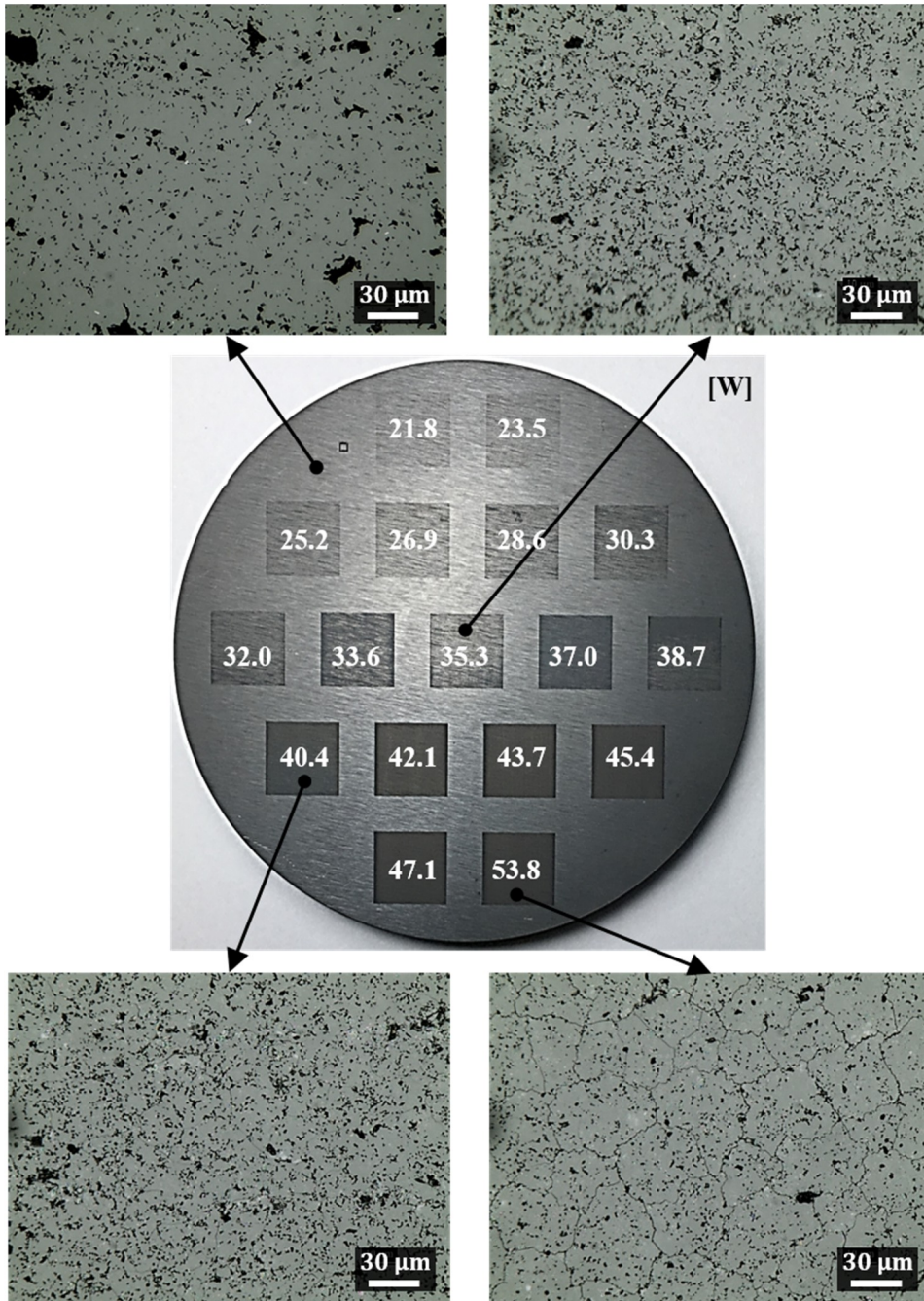
**Fig. 45 | Laser induced crack observation after 10 min polishing**

66
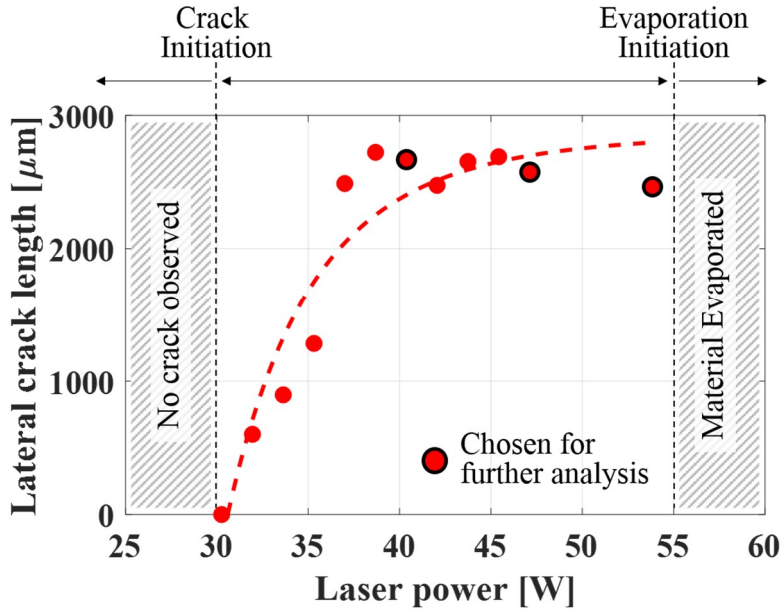
**Fig. 46 | Summation of lateral crack length**

The crack depths, local hardness, and surface roughness were measured only for three different output powers viz., 40.4, 47.1 and 53.8 W, at which the lateral crack length was saturated (red dots with a black circle in Fig. 46). In order to investigate the characteristics of the laser induced crack on the SiC surface, the output power of the laser was varied up to 53.8 W. The laser beam irradiated surface is shown in Fig. 47 (a), and the polished top and side surfaces of the SiC sample are represented in Fig. 47 (b) and (c), respectively. As the output power increased, local burns occurred evenly on the whole surface as shown in Fig. 47 (a-i) to (a-iv). At first, the laser irradiated surface was polished for 10 min to characterize the lateral crack length. As the output power increased, more cracks appeared with increasing length as shown in Fig. 47 (b-i) to (b-iv). The crack depth was also observed, as shown in Fig. 47 (c-i) to (c-iv), by using the sectioning method. The crack depth was

summarized for varying output power of the laser beam as shown in Fig. 48. In addition, the load-displacement curve was obtained by using Vickers' hardness test ($HV_{80}$) as shown in Fig. 49 and hardness was measured from the curve as shown in Fig. 50. The surface roughness were also measured with respect to the laser power and are shown in Fig. 51
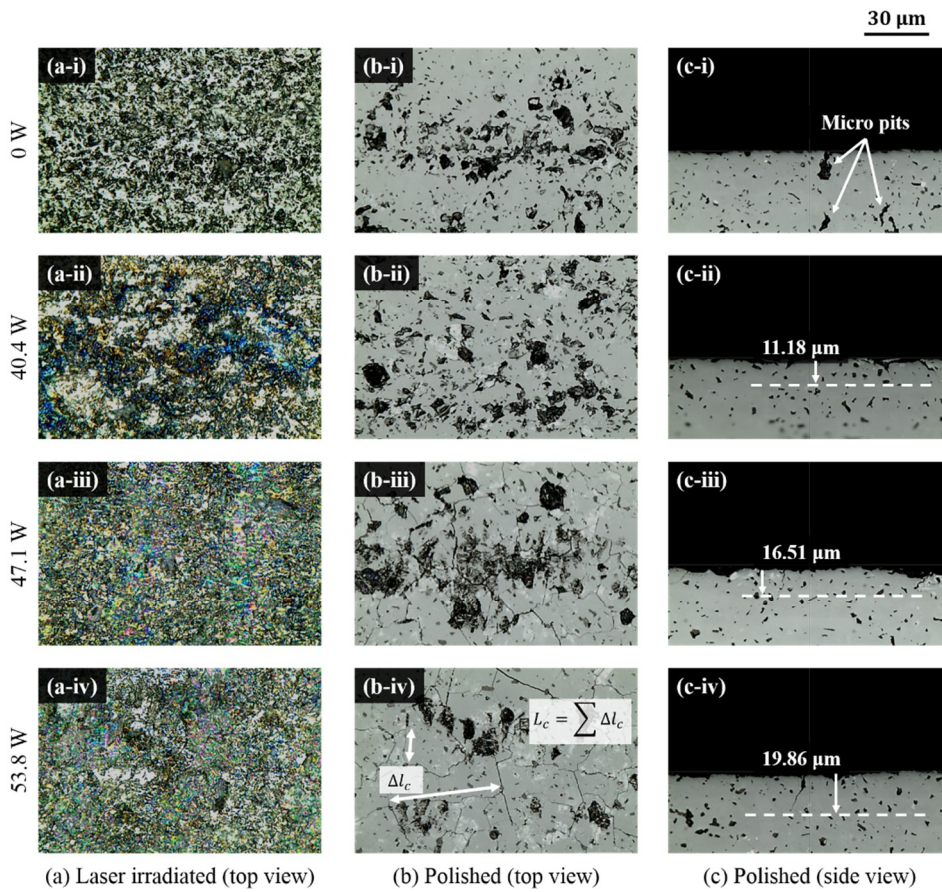


**Fig. 47 | Laser irradiated surface, crack length and depth after polishing**
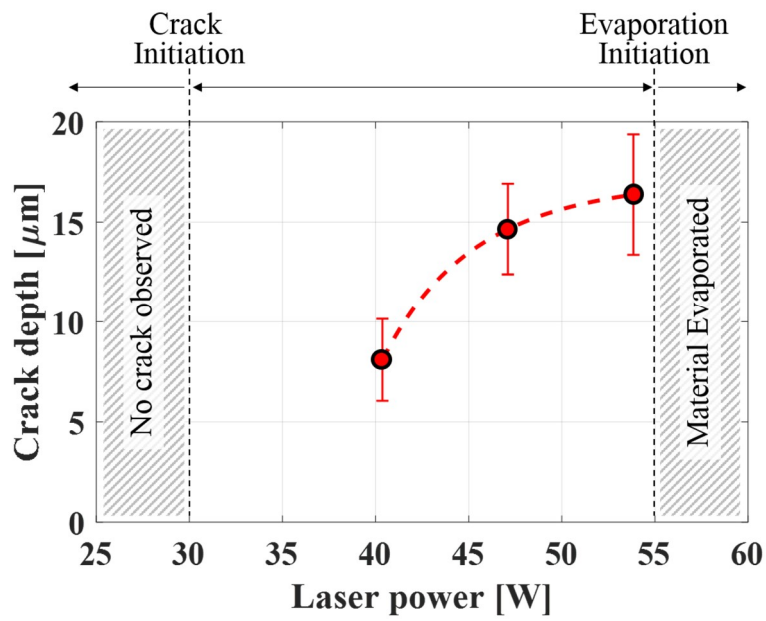
**Fig. 48 | Crack depth over laser output power**
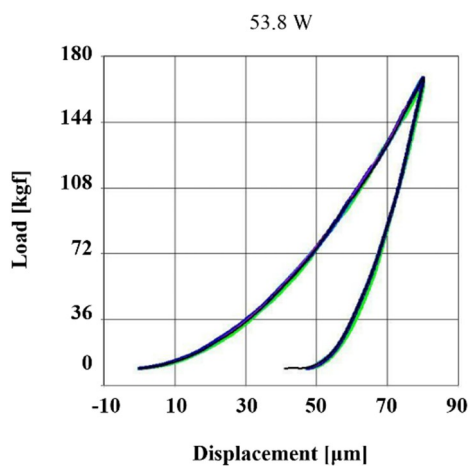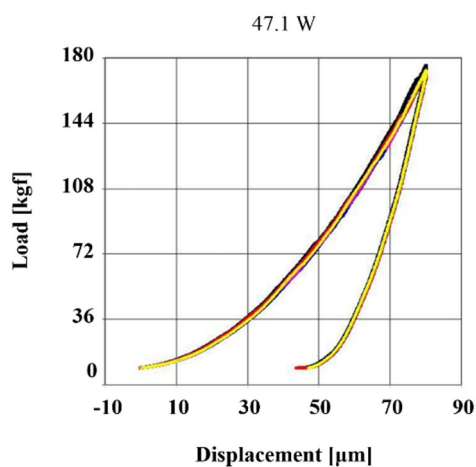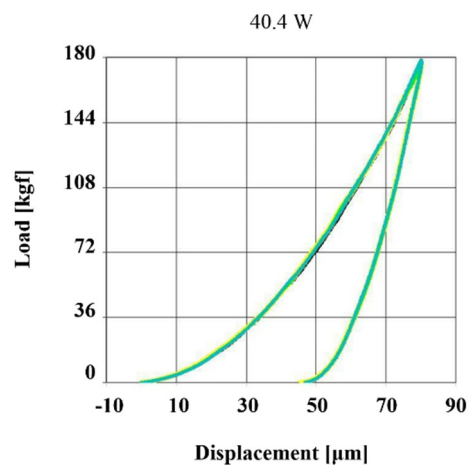
**Fig. 49 | Load-displacement curve for Vickers' hardness test [HV$_{80}$]**
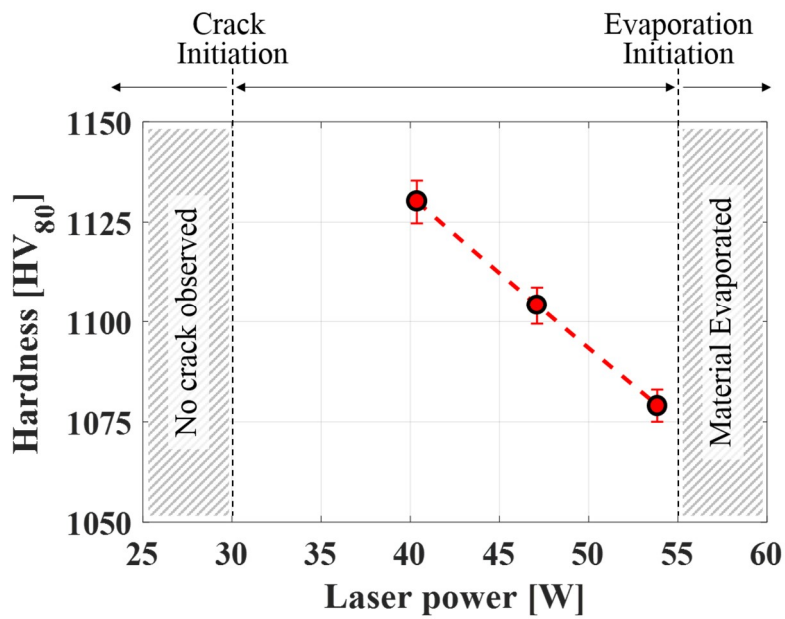
**Fig. 50 | Local hardness over laser output power**
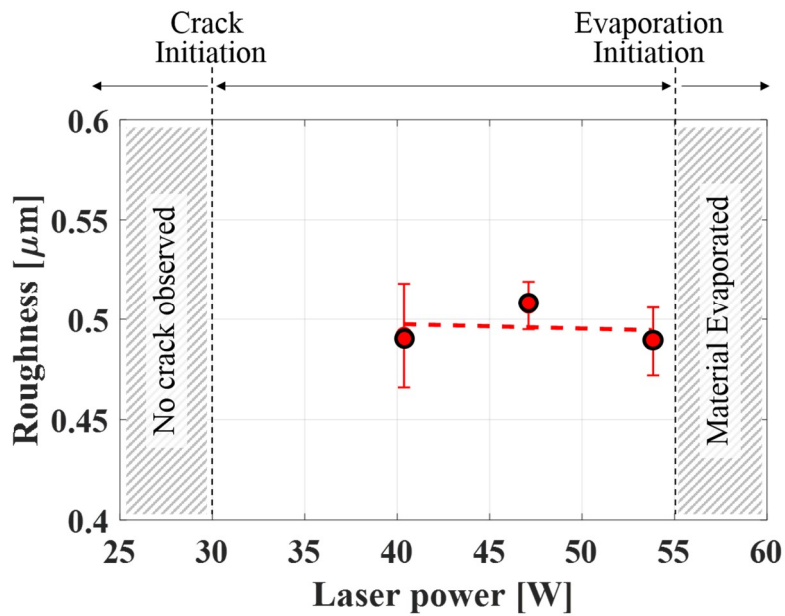


**Fig. 51 | Surface roughness over laser output power**

## 4.4. Effect of CO₂ Laser on Surface Modification

XRD analysis was carried out to investigate the effect of the laser induced crack generation on the crystalline structure of the SiC surface. Several apparent peaks were observed and represented by Bragg's index [86] in both the as-received and laser irradiated SiC samples. The overall peak intensity of the laser irradiated SiC (red line) decreased slightly as compared to that of the as-received sample (blue line), as shown in Fig. 52. However, the peak position in both the cases was the same, indicating that there was no change in the crystalline structure before and after the laser irradiation. It was deduced that the energy density of the irradiated laser was insufficient to affect its crystallinity.
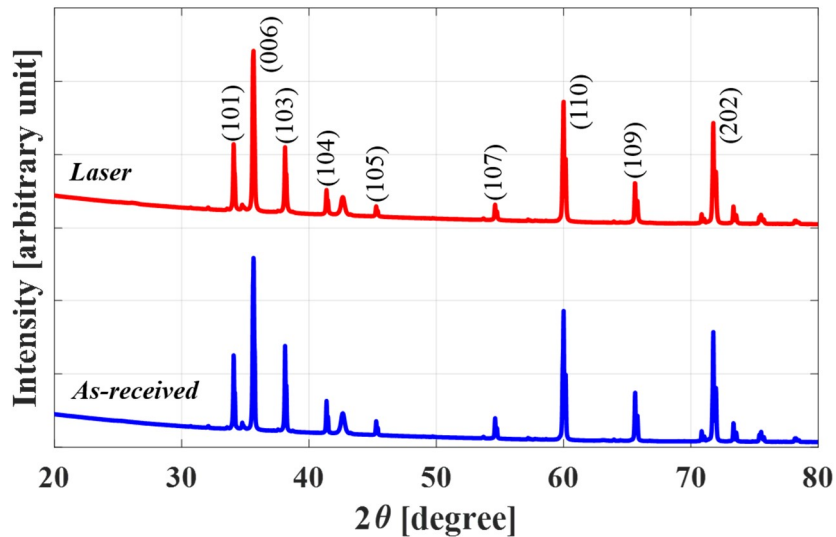


**Fig. 52 | XRD results of as-received and laser irradiated SiC**

As the laser induced crack generation is accompanied by thermal oxidation, argon (Ar) gas was used to replace compressed air to minimize the oxidation during laser irradiation. To investigate the elemental composition before and after the laser induced crack generation, as shown in Fig. 53, rapid and broad scanning of XPS analysis, using high energy density of the X-ray, was conducted on three different SiC surfaces, viz., the as-received sample (blue), the laser irradiated sample with compressed air (red) and the laser treated sample with Ar gas (green). Several apparent peaks were observed whose binding energy represented the elemental composition of Si (2p and 2s), C (1s), and O (1s). It was observed that the amount of surface O increased significantly, whereas that of Si and C was altered to a much lesser extent. Subsequently, XPS analysis with lower energy density of the ray was performed only for the outstanding 1s peaks of O, to observe its spectra in detail (inset), inferring that the argon gas suppressed the surface oxidation during the laser induced crack generation.
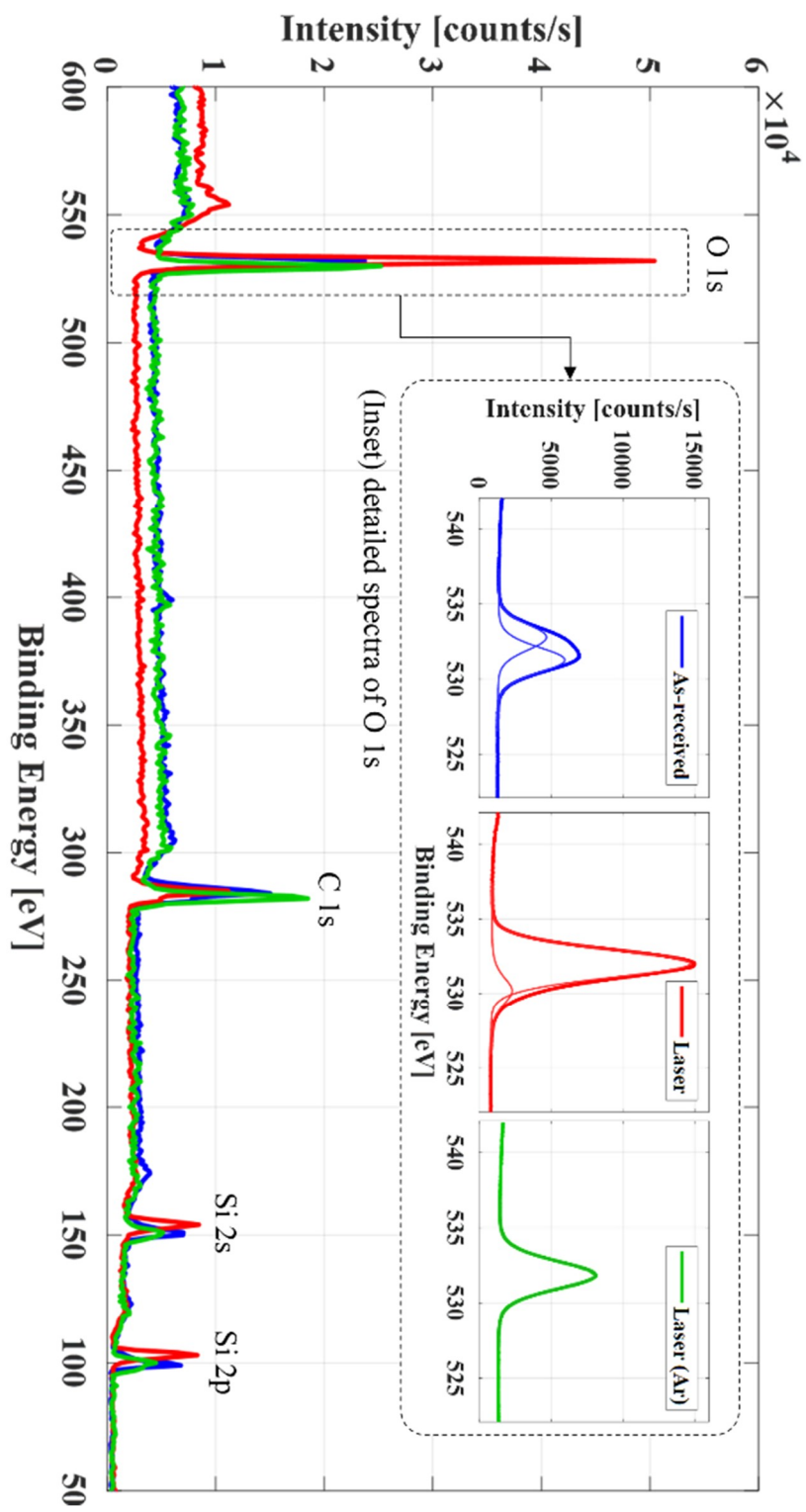
**Fig. 53 | XPS results of the as-received, laser and laser with argon**

# Chapter 5. Evaluation of Material Removal

## 5.1.    Process Design

In order to investigate the effect of the surface cracks on the material removal in the polishing of the SiC sample, the low power laser induced crack generation process was followed by polishing or LaPol as shown in Fig. 54 (a) and (b), respectively. For performance evaluation, the MRR of the polishing or LaPol processes with prior crack generation was evaluated by comparing them with single polishing or single LaPol, as shown in Fig. 34 (b) and (c), respectively. The surface quality in the four processes was also compared. As the laser induced generation of the crack was accompanied by oxidation at the beam spot, compressed air was substituted by argon as the assist gas to minimize the oxidation during crack generation. The cracked, but non-oxidized, surface was then polished and its MRR and surface roughness were evaluated. The process parameters are listed in Table 17.
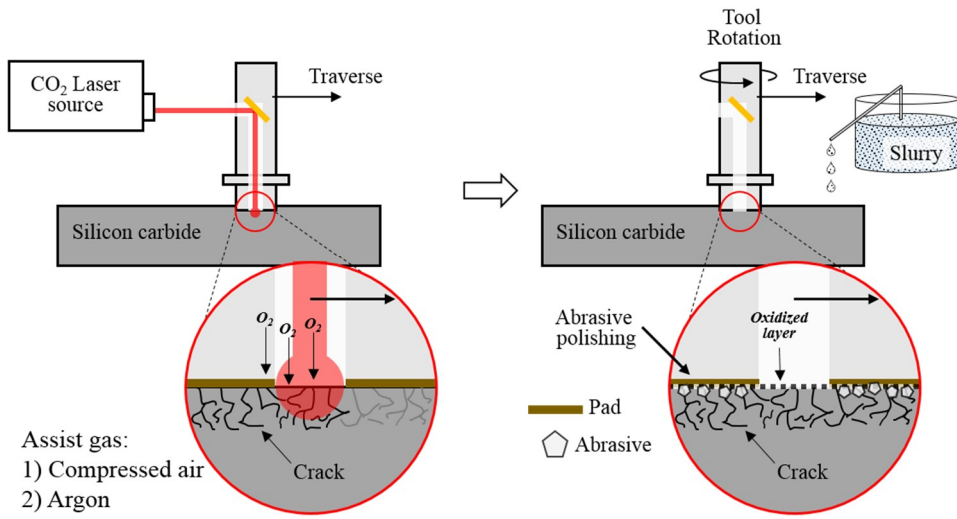
(a) Crack generation and successive polishing (Crk+Pol)
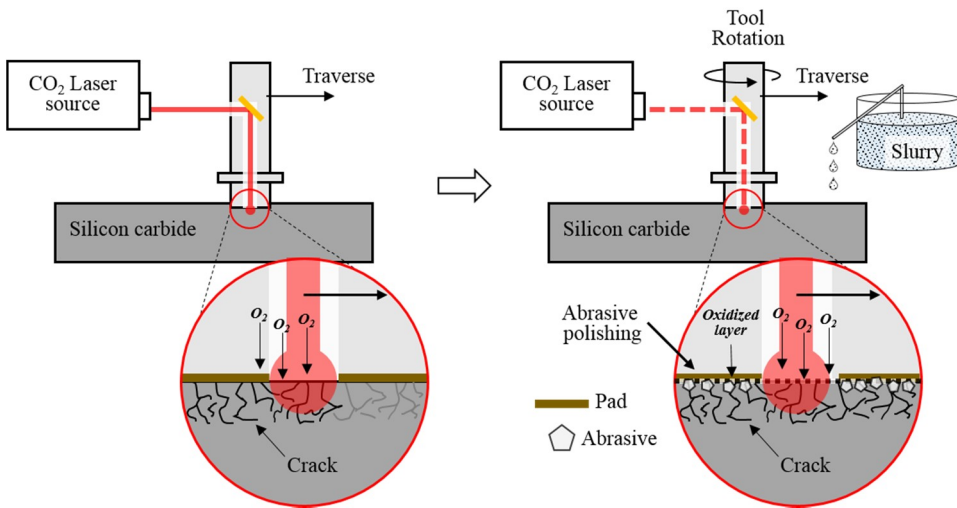


(b) Crack generation and successive LaPol (Crk+LaPol)

**Fig. 54 | Experimental paradigm of hybrid process**

**Table 17 | Process parameters**

| Laser induced crack generation | |
|---|---|
| Source | $CO_2$ (wavelength 10.6 μm) |
| Type | Continuous wave (CW) |
| Beam mode | $TEM_{00}$ (Gaussian) |
| Beam diameter | 150 μm |
| Beam path | Raster (50 μm in width) |
| Output power | 47.1 W (=16% duty ratio) |
| Feed rate | 25 mm/s |
| Assist gas | Compressed air or Argon gas (N50) |
| **Polishing** | |
| Pressure (Force) | 45.69 kPa (30 N) |
| Tool diameter | 30 mm |
| Rotational speed | 1200 RPM |
| Dwell time | 10 ~ 120 min |
| Feed rate | 25 mm/s |
| Slurry | Diamond and ceria (~1 μm diameter) |
| Pad | Polyurethane (1.5 mm in thickness) |
| (Laser output power) | 94.3 W (=30% duty) only for LaPol |

## 5.2.    Evaluation of MRR in Successive Process

In order to investigate the effect of laser induced crack generation on material removal in the polishing process, five SiC workpiece samples were prepared as shown in Fig. 55 and observed with the OM as shown in Fig. 56 (row i) viz., two as-received SiC samples for polishing (a) or LaPol (d), two cracked SiC samples for polishing (b) or LaPol (e), and one sample with a crack generated using argon gas (c). After 10 min of the successive polishing or LaPol process (Fig. 56, row ii), laser

induced cracks were observed, except in the as-received SiC surface for polishing. Not only was the laser induced pre-cracked surface observed (b-ii, c-ii and e-ii), even the single LaPol of the as-received SiC surface generated cracks during the process (d-ii). Microscale black pits were also observed in all the cases, which might have occurred during the material fabrication process such as sintering or grinding by the vendor. Little or no crack remained in 120 min of polishing or LaPol process (row iii). Note that fragmented traces were observed only in the LaPol process as shown in Fig. 56 (d-iii) and (e-iii) (red arrows), suggesting that there was a new grain boundary opening or crack propagation during the successive polishing process. The equally distributed 15 points were observed for each process in order to see if the surface were representative of whole sample surface as shown in Fig. 57~Fig. 61.



**Fig. 55 | Final polished surface in naked eye**
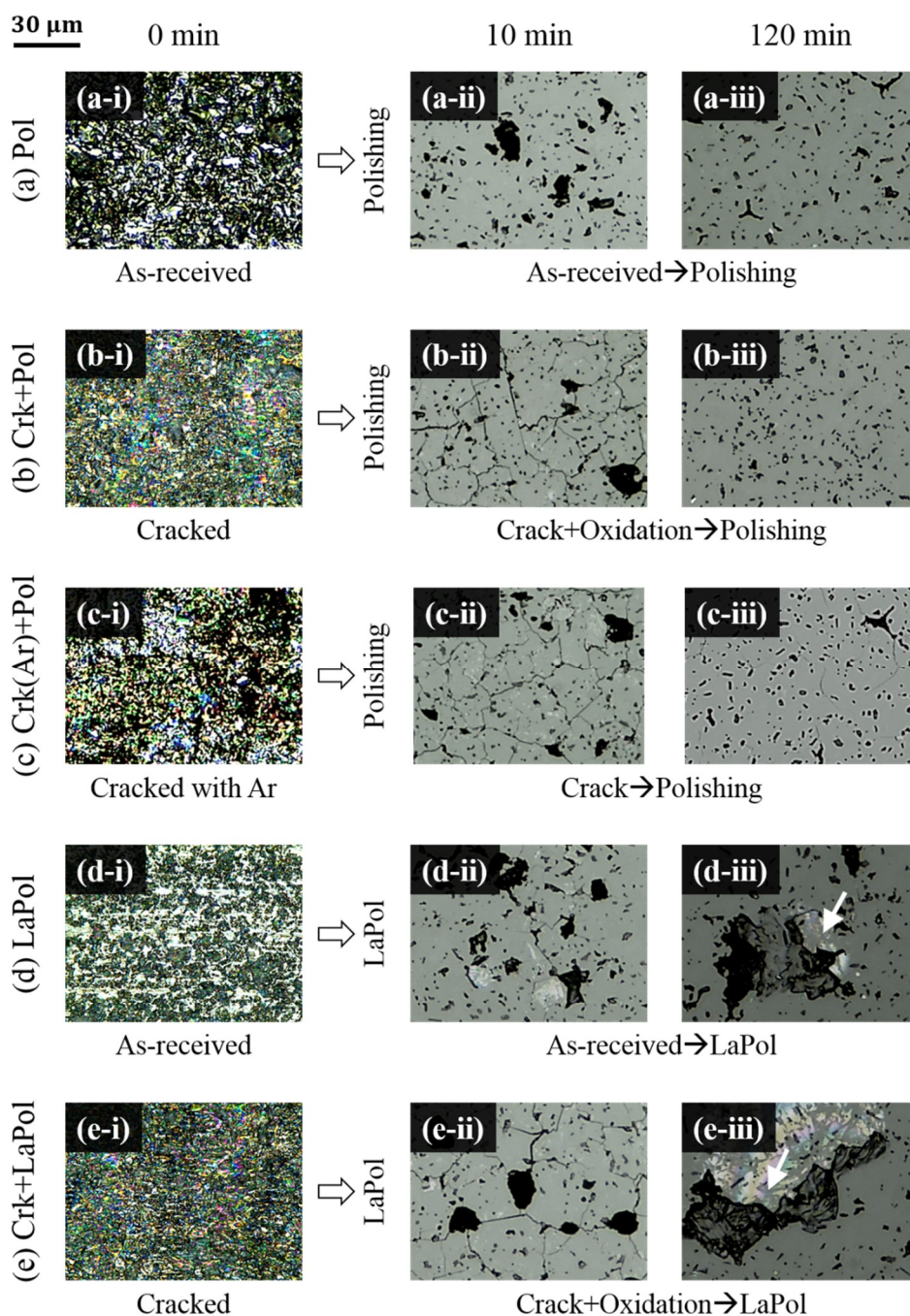
**Fig. 56 | Surfaces after five different processes**
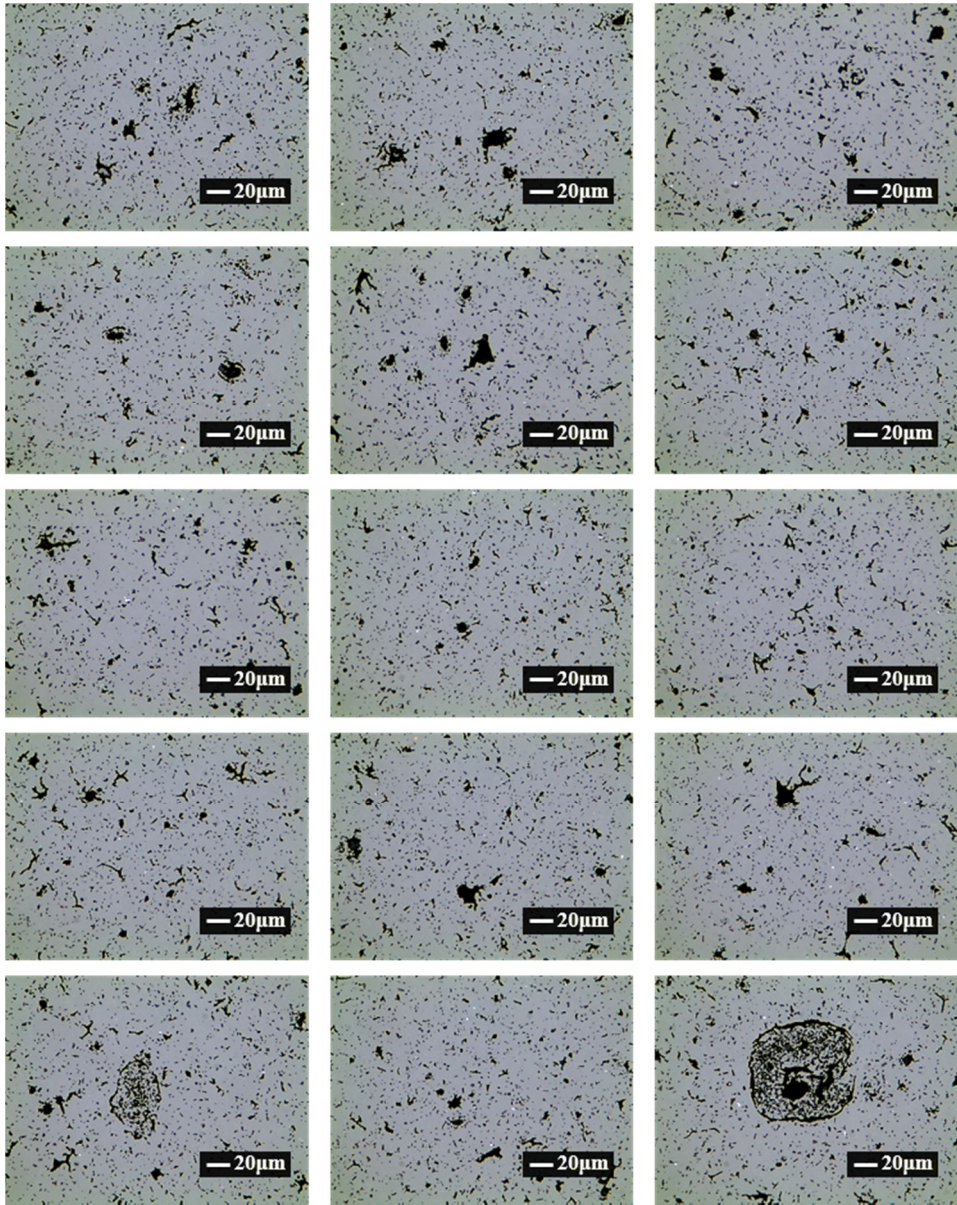
**Fig. 57 | Pol: Polishing of the as-received surface (OM)**

**Fig. 58 | Crk+Pol: Polishing of the cracked+oxidized surface (OM)**

**Fig. 59 | Crk(Ar)+Pol: Polishing of the cracked surface (OM)**

**Fig. 60 | LaPol: LaPol of the as-received surface (OM)**
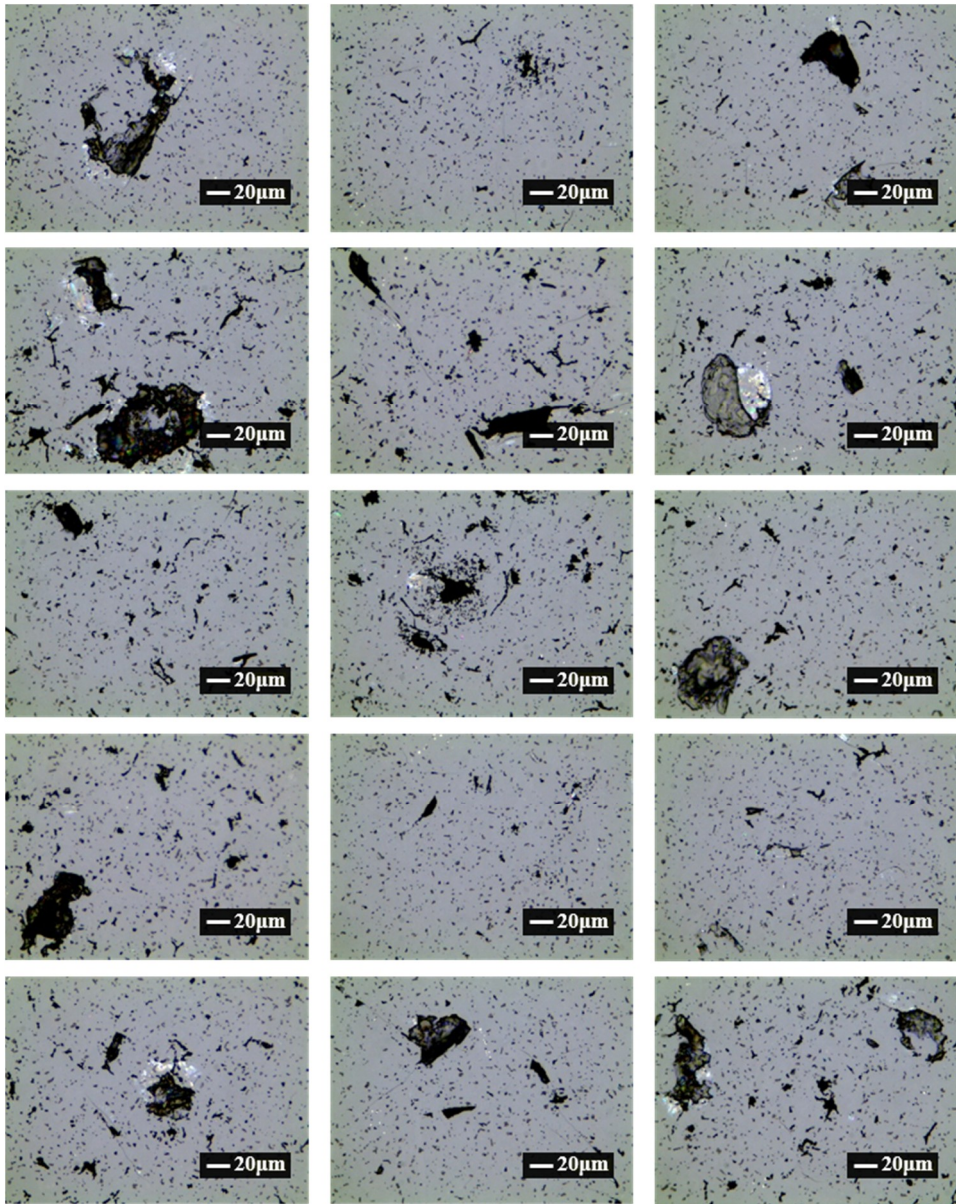
**Fig. 61 | Crk+LaPol: LaPol of the cracked+oxidized surface (OM)**

The removal height was measured, and removal rate calculated to evaluate the material removal in successive polishing or LaPol process as shown in Fig. 62. For 120 min of the successive process, the maximum removal height was $12.19 \pm 0.42$ μm in the LaPol process of the pre-cracked SiC surface (Crk+LaPol), whereas the minimum height was $6.81 \pm 0.71$ μm in a single polishing of the as-received sample (Pol). As shown in Fig. 63, the MRR was calculated from the removal height which was measured several times during the successive process. The effect of prior cracks on the successive polishing process regarding the MRR was investigated by comparing the three solid lines (blue triangle, red inverted triangle and green circle). Although the MRR of the Crk+Pol process was a little higher than that of the Crk (Ar)+Pol process, both were much higher than that of the single polishing (Pol) process. It is inferred that the prior laser induced crack was the more prominent mechanism as compared to oxidation resulting in a higher MRR in the successive polishing process. This was also shown with the normalized MRR (Fig. 64), representing crack portion is 45 % whereas 10 % from oxidation. On comparing the two dot-and-dash lines (red diamond and blue square), an increase in the MRR with prior crack was observed in the successive LaPol process.
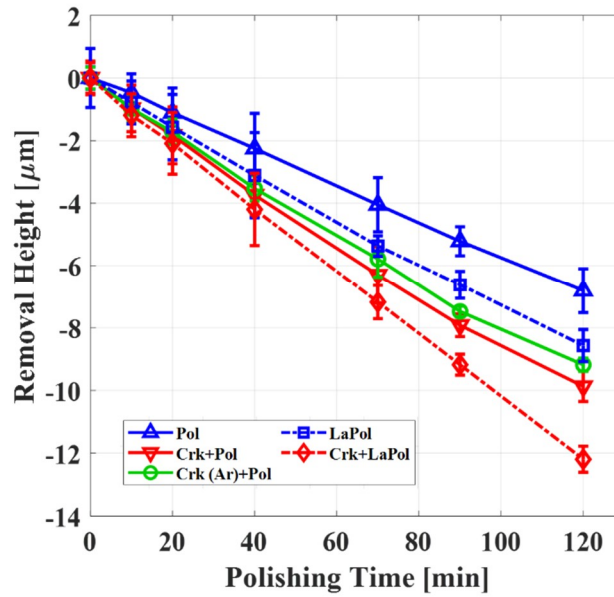
**Fig. 62 | Removal height over polishing time**
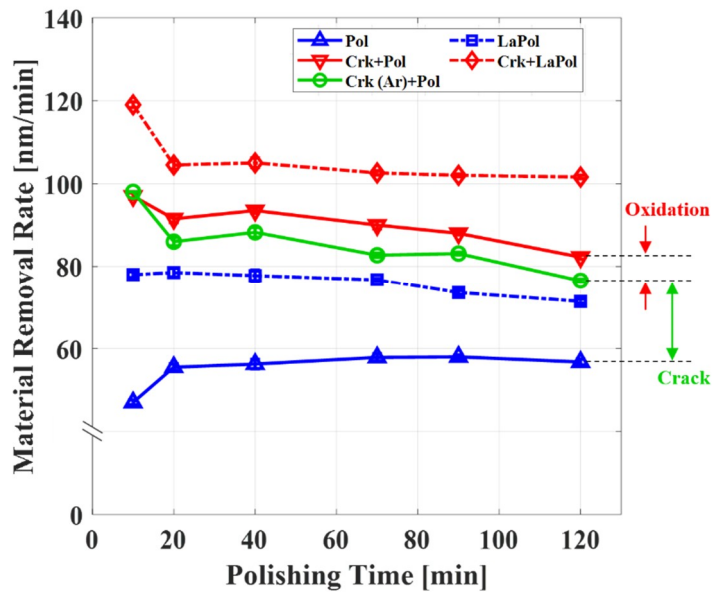


**Fig. 63 | Material removal rate over polishing time**
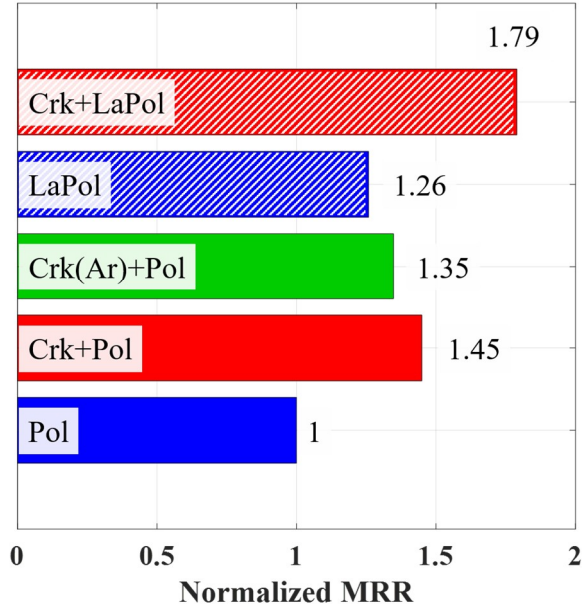
**Fig. 64 | MRR comparison after 120 min of processing**

## 5.3. Evaluation of Surface Roughness in Successive Process

The arithmetic roughness ($R_a$) of the surface, shown in Fig. 65, was also measured during each process. It is seen that the initial roughness is much higher in the prior crack generation process (Crk+Pol and Crk+LaPol), but only a little higher in the Crk(Ar)+Pol case, which might be due to the surface oxidation. After 10 min of successive polishing or LaPol process, the arithmetic roughness in all the cases decreased to less than 100 nm and the final roughness was less than 15 nm.

The peak-to-valley (pv) roughness ($R_{pv}$) shows the same trend as $R_a$ as represented in Fig. 68. The pv roughness of the pre-cracked sample was 5 times higher than that of as-received sample, which might also be originated from the

recast oxidized layer during the laser irradiation. After 10 min of successive polishing or LaPol process, the pv roughness also decreased to 500 nm in all the samples. Final pv roughness was less than 100 nm.

The $R_a$ and $R_{pv}$ of the final polished surface were compared after the 5 processes. The mean and standard deviation of $R_a$ and $R_{pv}$ with its maximum and minimum were compared for 5 processes as shown in Fig. 66 and Fig. 69, respectively. The distributions of $R_a$ and $R_{pv}$ were also compared for 5 processes using the box-whisker plots [87] as shown in Fig. 67 and Fig. 70, respectively.
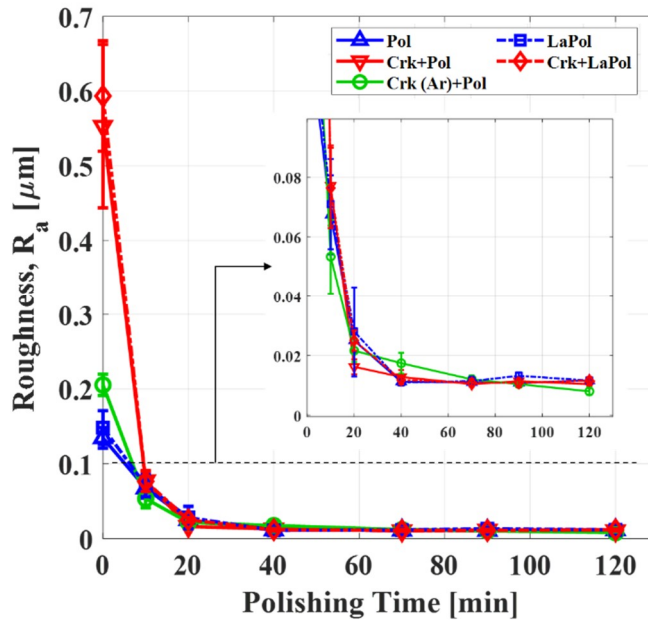


**Fig. 65 | Surface roughness ($R_a$) over polishing time**
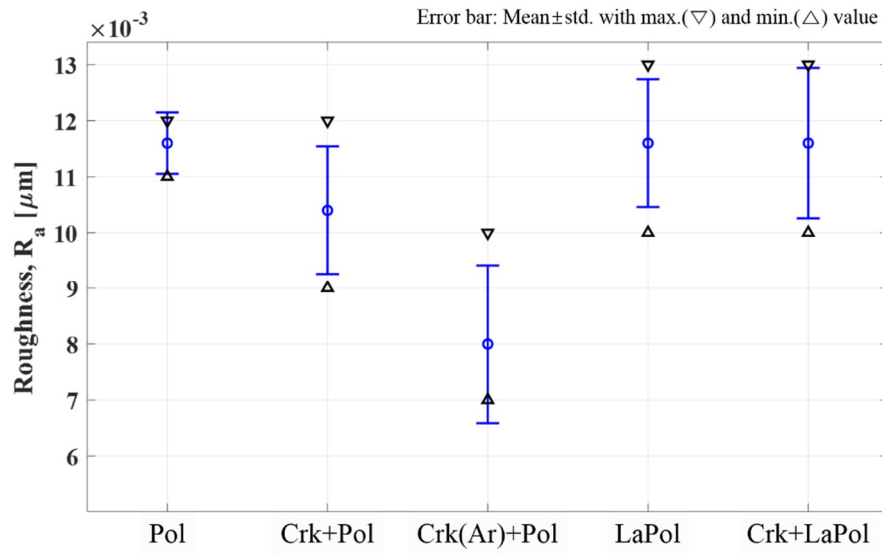
**Fig. 66 | Surface roughness ($R_a$) of final polished surface**
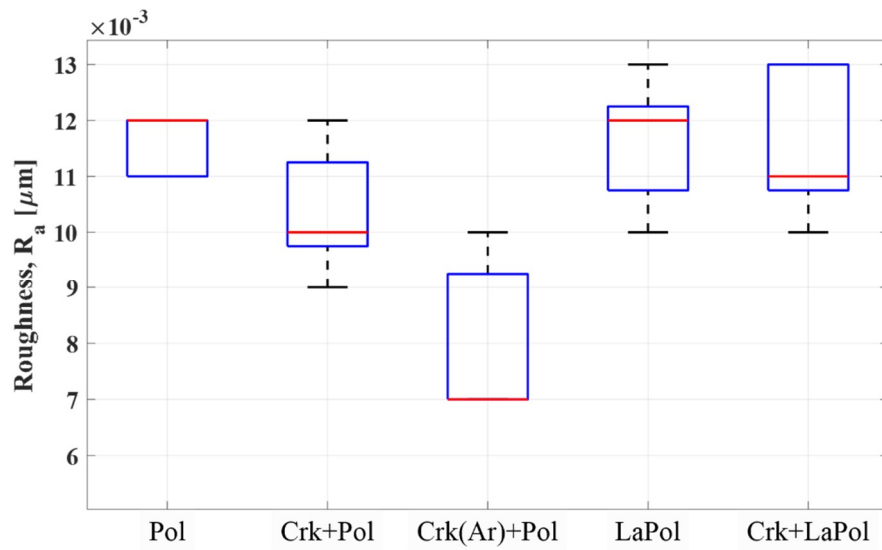


**Fig. 67 | Surface roughness ($R_a$) of final polished surface (box plot)**
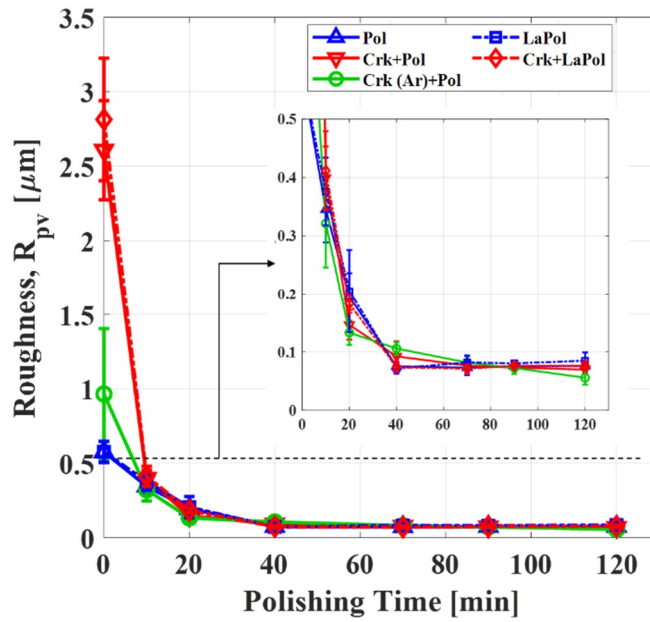
**Fig. 68 | Surface roughness ($R_{pv}$) over polishing time**
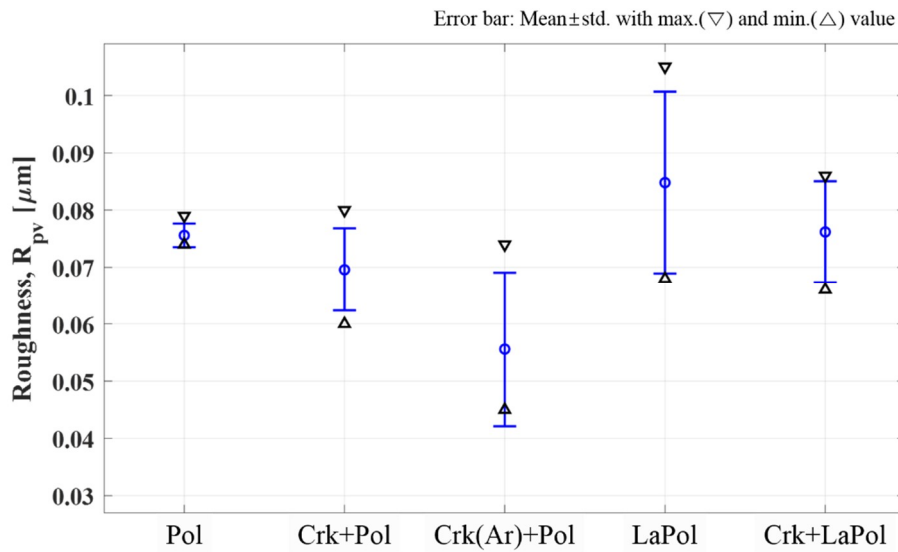


**Fig. 69 | Surface roughness ($R_{pv}$) of final polished surface**
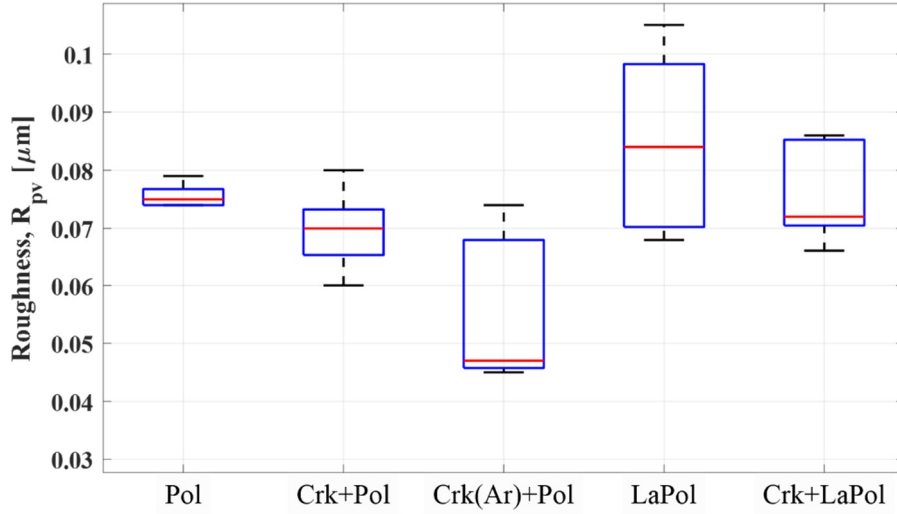
**Fig. 70 | Surface roughness ($R_{pv}$) of final polished surface (box plot)**

Since the area roughness parameter, such as $S_a$ (the arithmetic average of the 3D roughness), gives more significant values, final polished surface height profiles of the equally distributed 15 points (0.8 x 0.8 mm) were observed in CCI image as shown in Fig. 71 - Fig. 75, for 5 processes. The mean with standard deviation and the distribution of $S_a$ roughness were compared as shown in Fig. 76 and Fig. 77, respectively
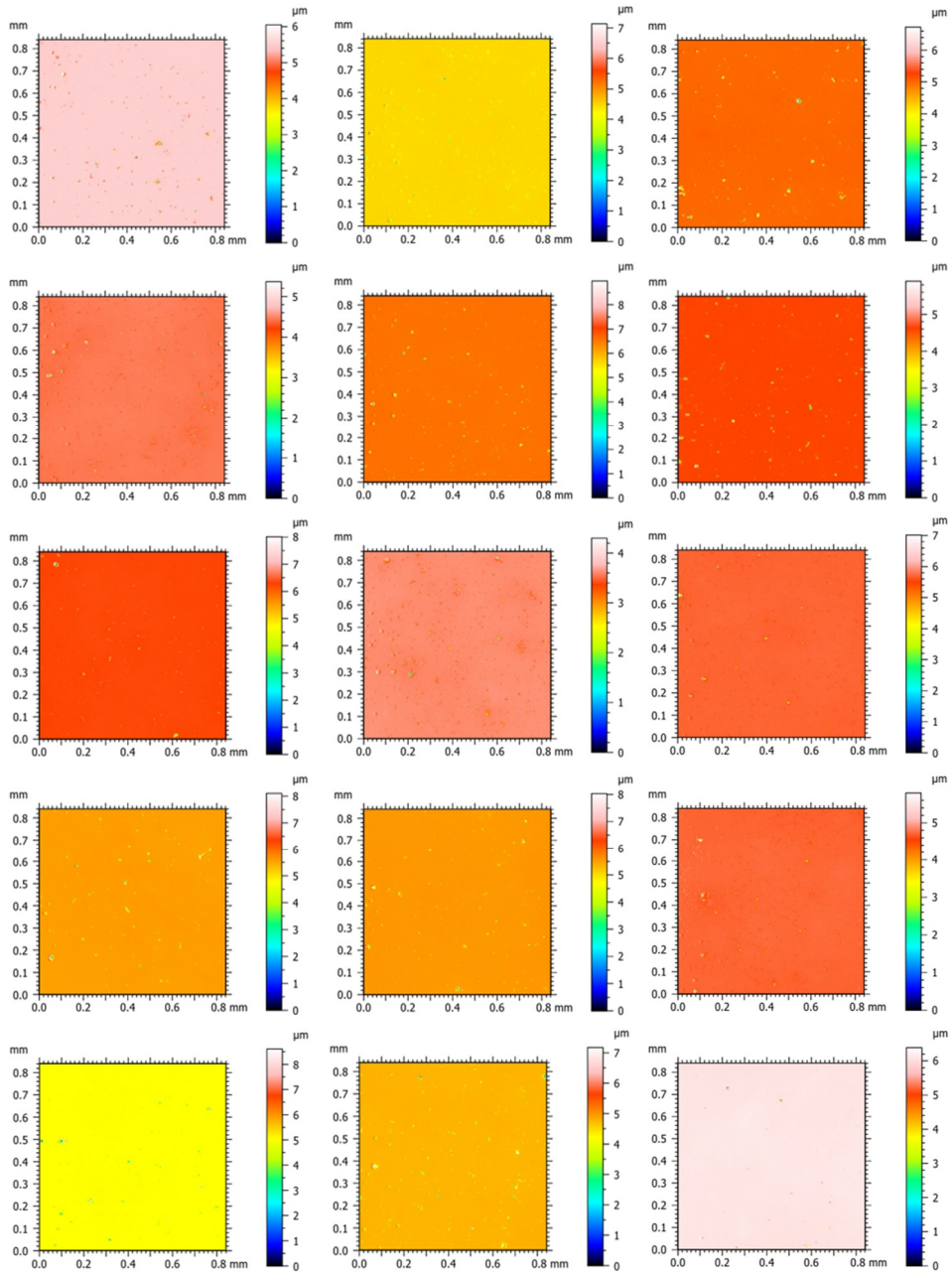
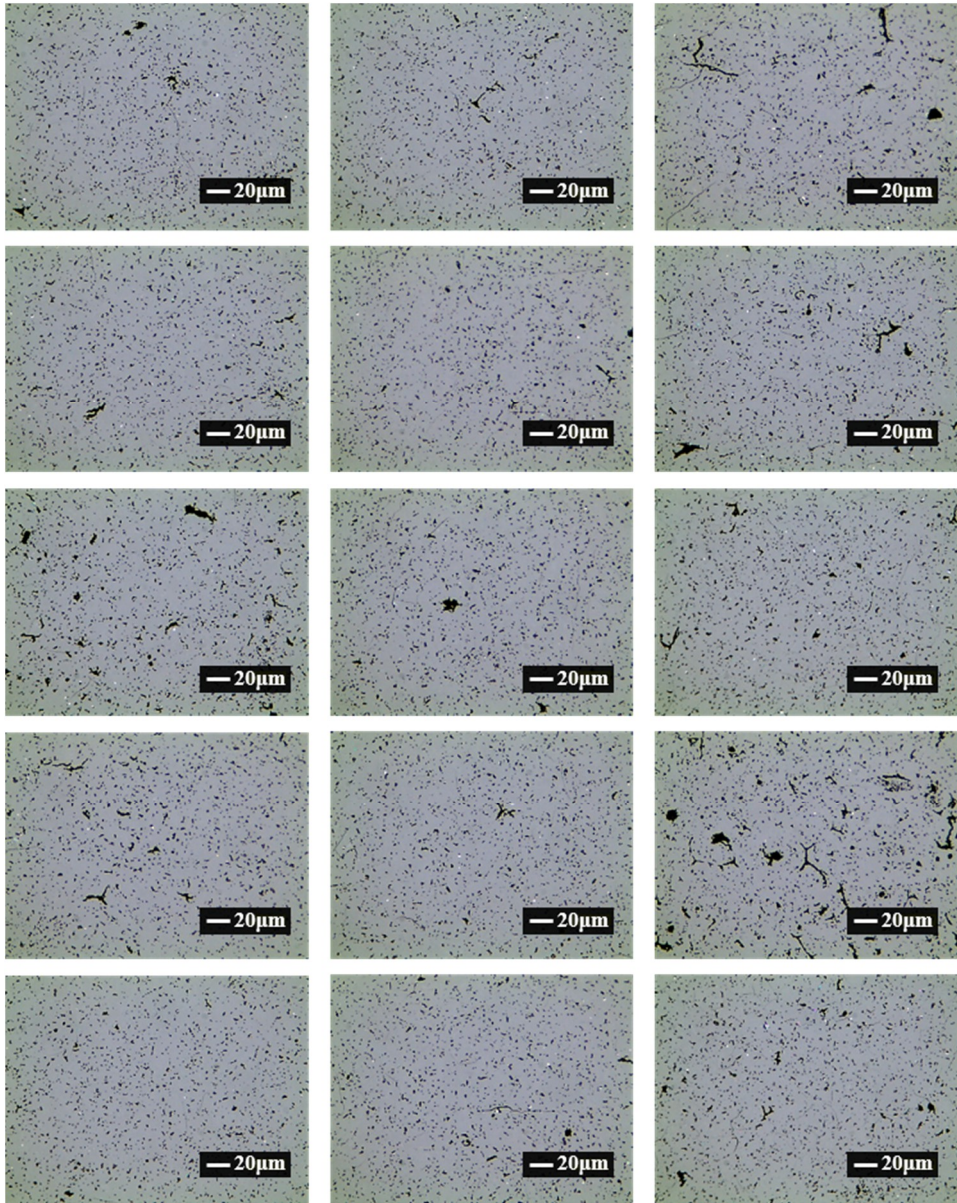**Fig. 71 | Pol: Polishing of the as-received surface (CCI)**
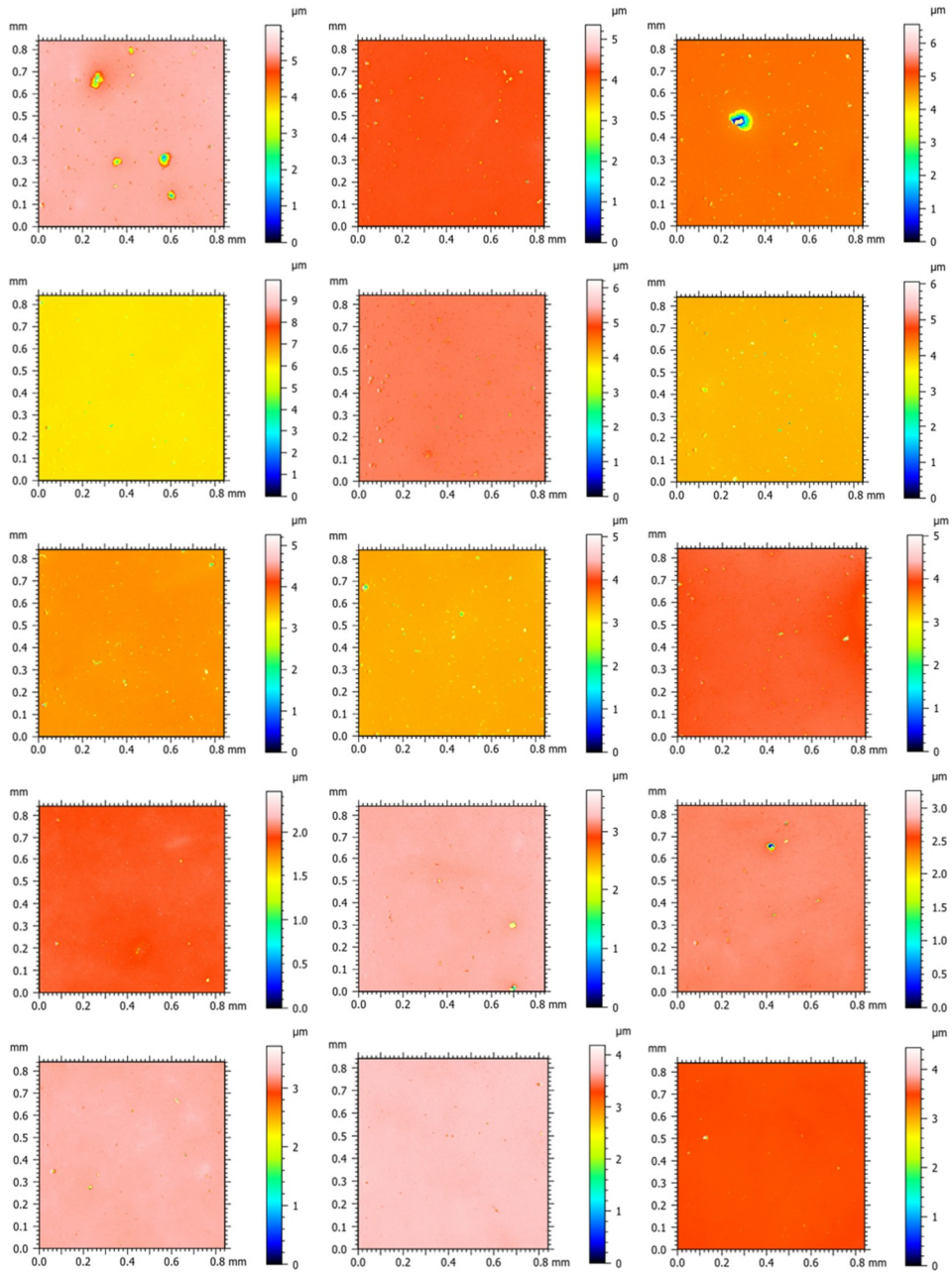
**Fig. 72 | Crk+Pol: Polishing of the cracked+oxidized surface (CCI)**
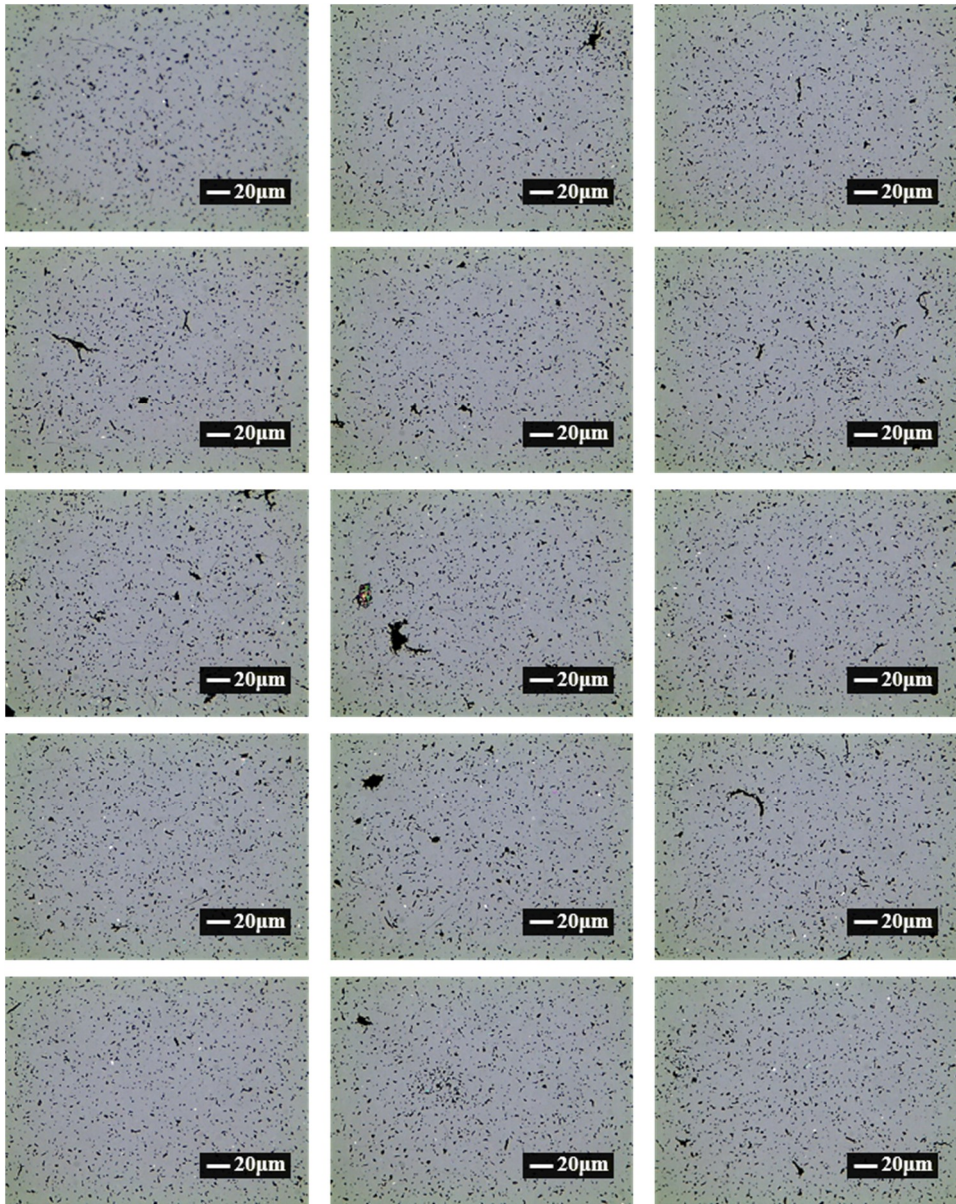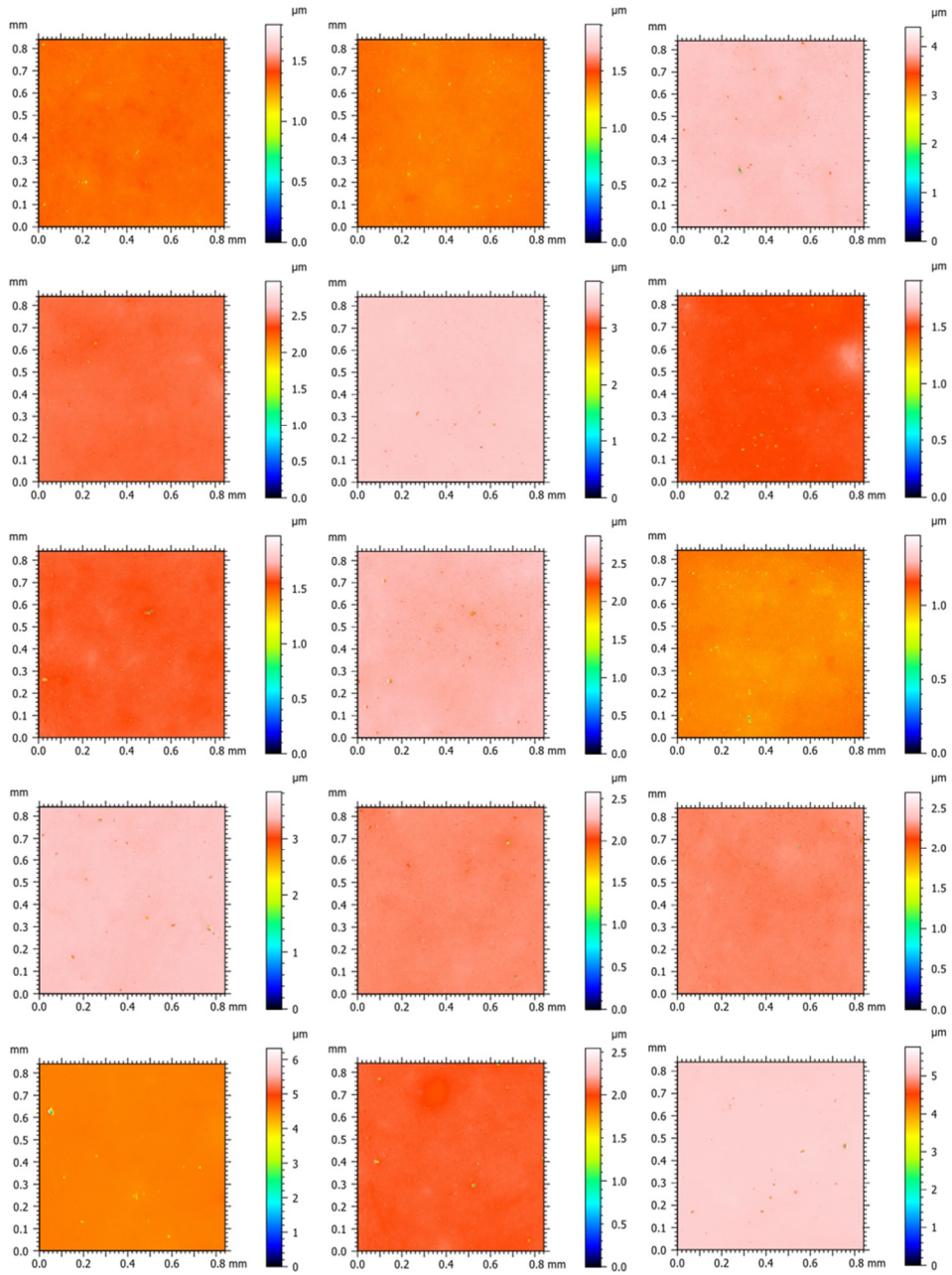
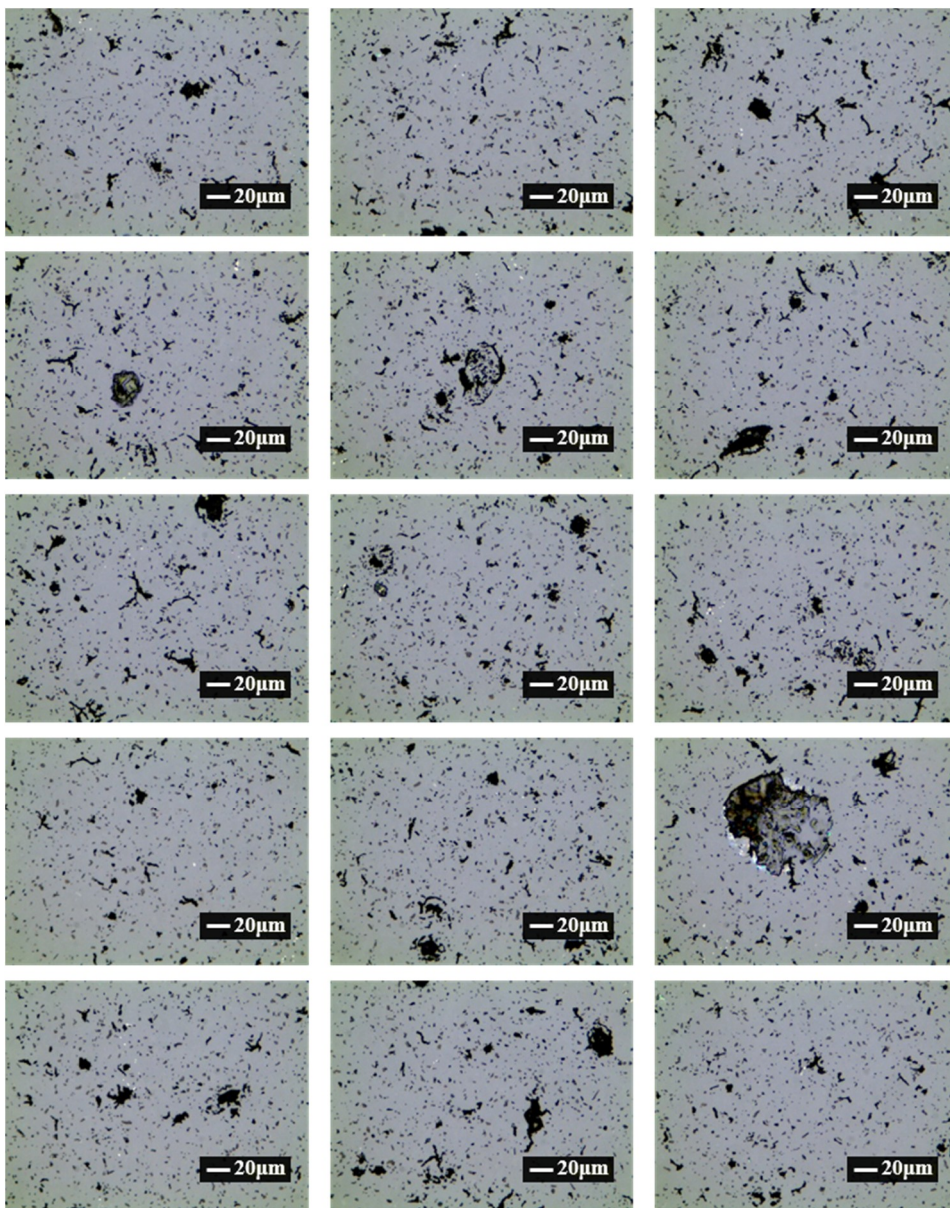**Fig. 73 | Crk(Ar)+Pol: Polishing of the cracked surface (CCI)**
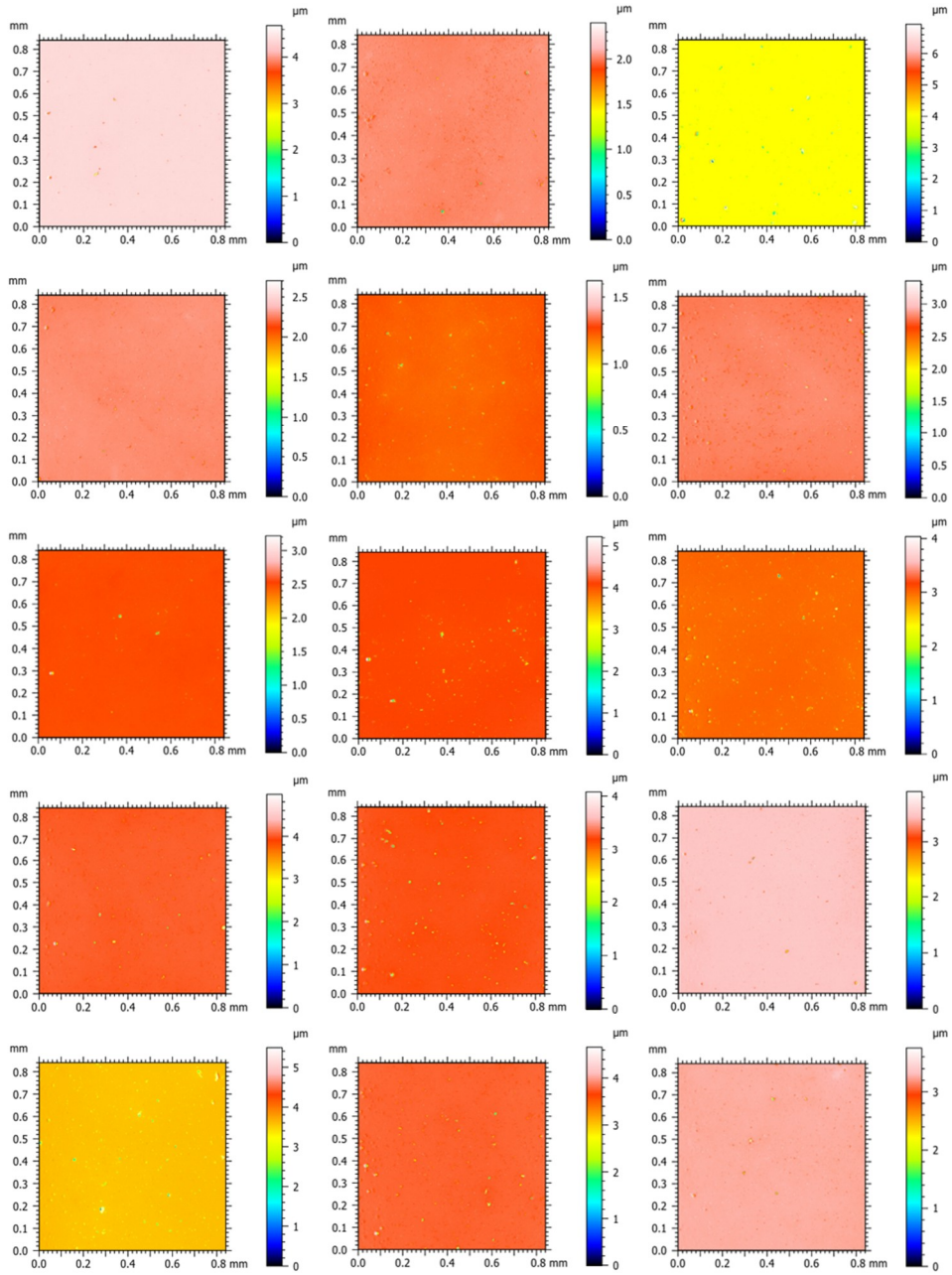
**Fig. 74 | LaPol: LaPol of the as-received surface (CCI)**

95
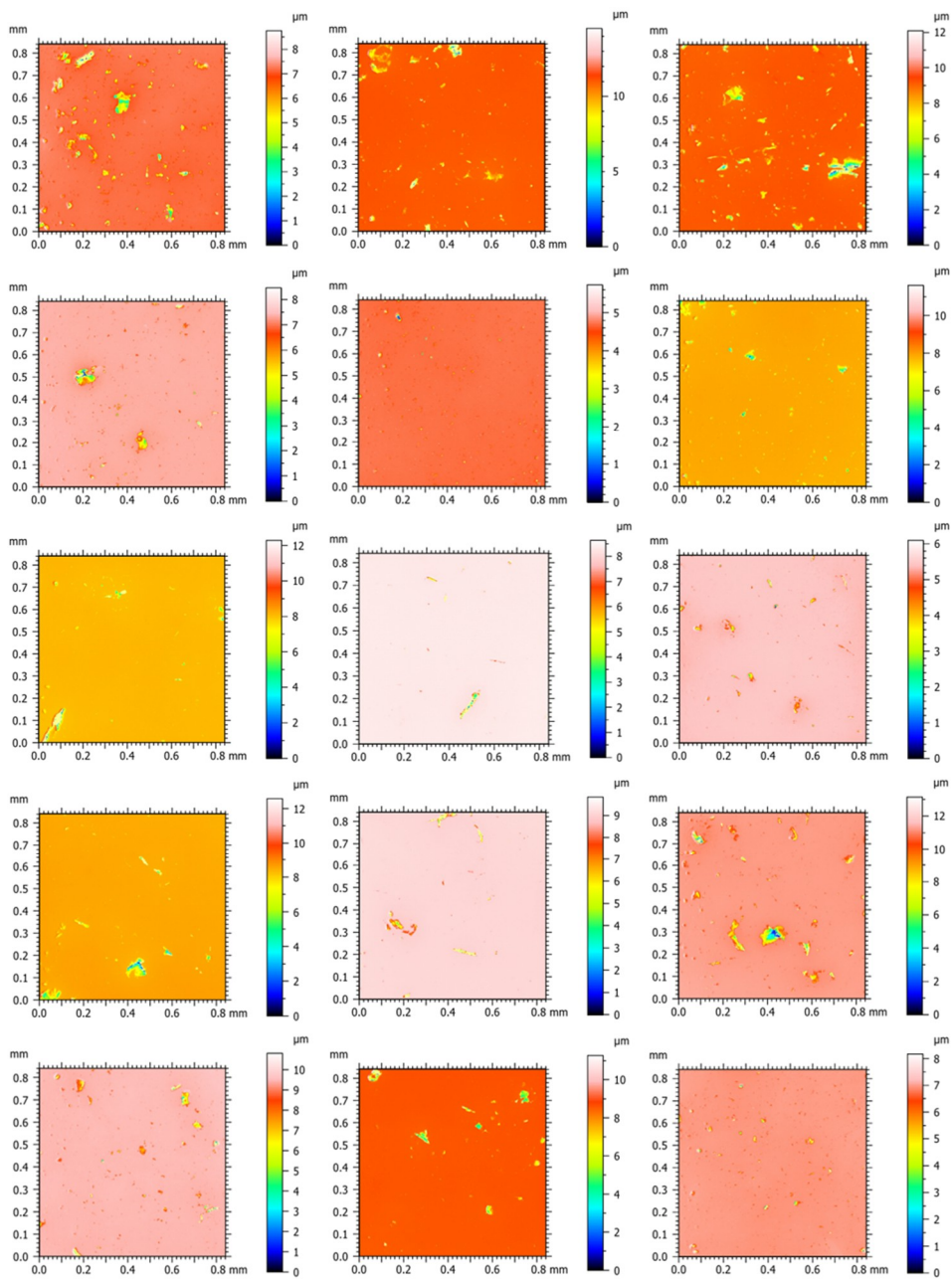
**Fig. 75 | Crk+LaPol: LaPol of the cracked+oxidized surface (CCI)**
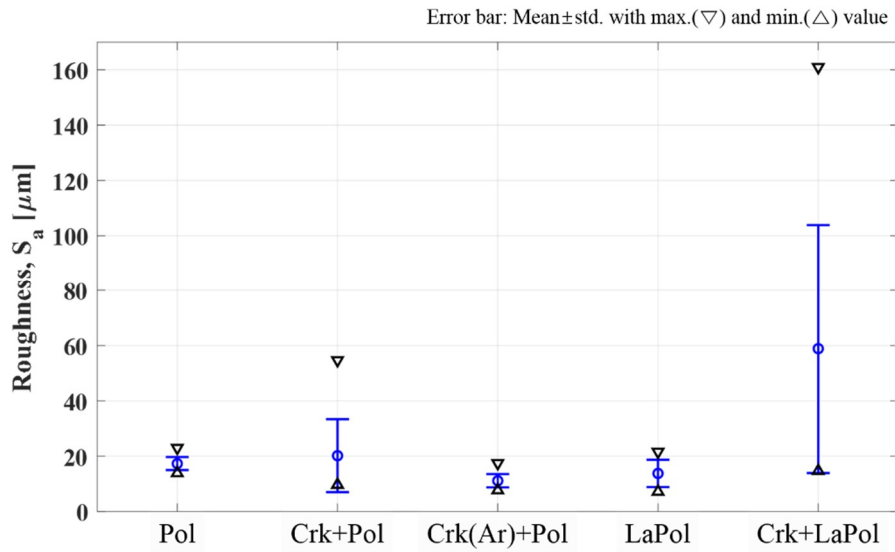
**Fig. 76 | Surface roughness ($S_a$) of final polished surface**
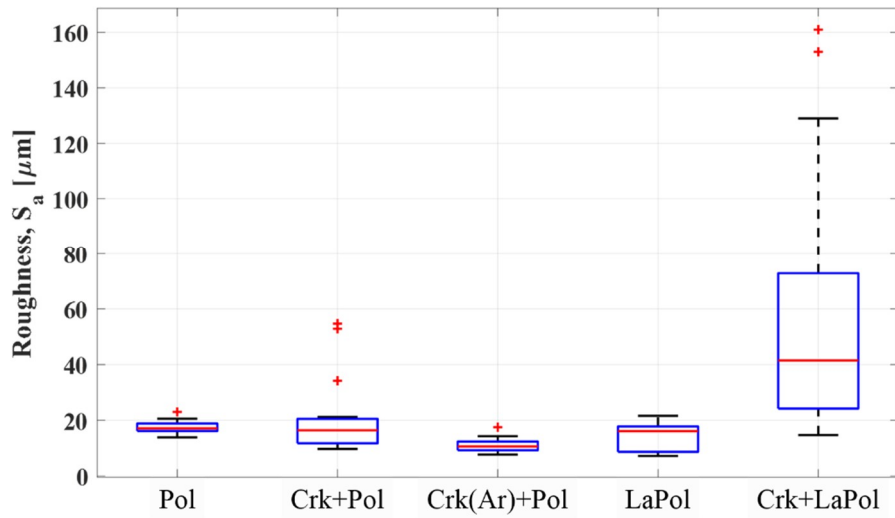


**Fig. 77 | Surface roughness ($S_a$) of final polished surface (box plot)**

## 5.4.  Fabrication of 3D Surface

In order to demonstrate the hybrid process, spherical 3D surface was fabricated. The laser beam induced material removal process was conducted for fabricating the concave shape. The LaPol and Pol process was then carried out for mirror surface fabrication. The design of the model and the laser beam parameter were set on the custom made tool path generator as listed in Table 18, which provides the tool path as shown in Fig. 78. The fabricated surface was measured by using line profiler through its center and compared to the model design as shown in Fig. 79.

**Table 18 | Parameters for fabrication of 3D surface**

| Model design | |
|---|---|
| Model Type | Sphere |
| Radius at Z= 0 mm | 30 mm |
| Depth from Z=0 mm | 0.05 mm |
| **Laser beam machining** | |
| Output power | 111.1 W (=35% duty ratio) |
| Feed rate | 25 mm/s |
| Assist gas | Compressed air |
| **Polishing** | |
| Pressure (Force) | 45.69 kPa (30 N) |
| Tool diameter | 30 mm |
| Rotational speed | 1200 RPM |
| Dwell time | ~ 10 h |
| Feed rate | 25 mm/s |
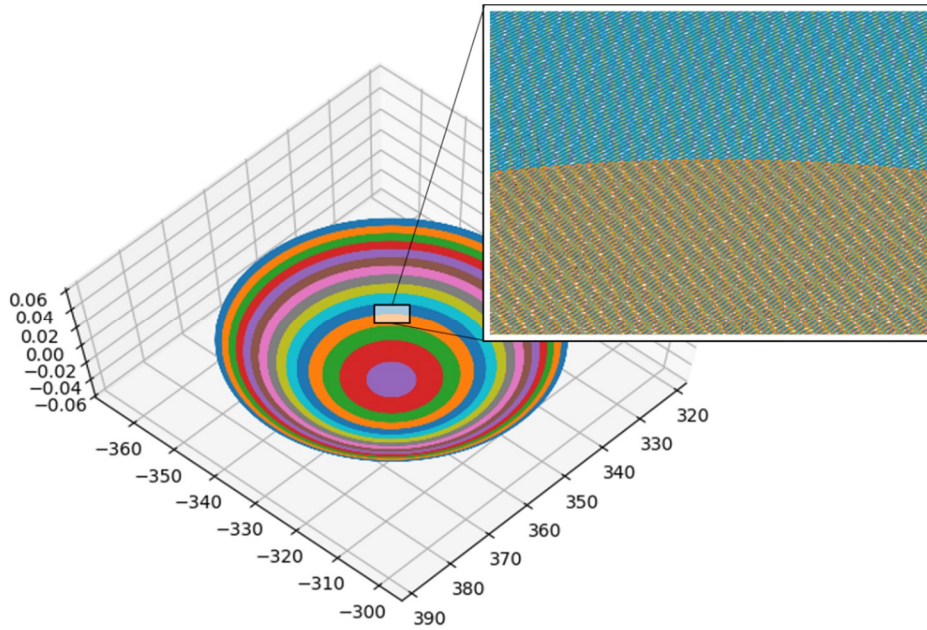
**Fig. 78 | Tool path for fabrication of 3D surface**
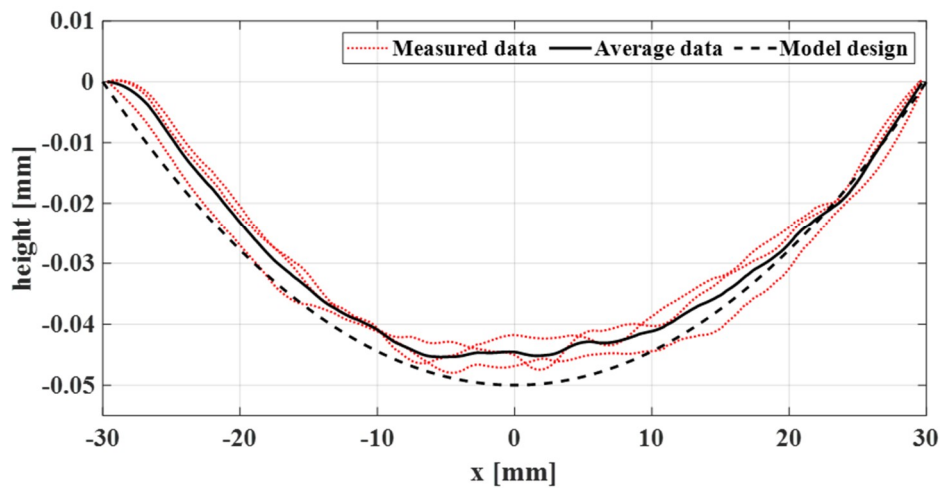


**Fig. 79 | Evaluation of 3D surface with the model design (line profiler)**

# Chapter 6. Discussion

## 6.1.  System Configuration

Modern computer controlled optical surfacing (CCOS) machines normally have the z-axis tilted by some degrees, as shown in Fig. 80. Therefore, the pressure and relative velocity follow Gaussian distribution on the contacting area, which makes the removal more predictable. However, the hybrid tool developed in this study moves with a self-rotating and planetary motion. This is because a tilted structure is incompatible with the laser irradiation during polishing.
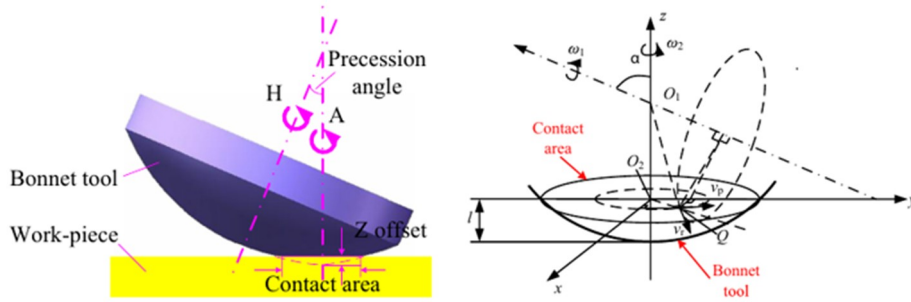


**Fig. 80 | Tilted polishing tool**

Although the system employs a plane tool end, the pressure distribution might not be flat. Furthermore, the slurry circulation system has no filtration, so that chips from the SiC removal are mixed with the slurry. This might have a degrading effect on material removal.

## 6.2. Laser-SiC Interaction

When a Nd:YAG laser was irradiated on SiC in a previous study, the hardness of the SiC surface increased with higher laser energy density [39]. In this study, however, using a $CO_2$ laser, the hardness decreased with higher laser power.

The laser irradiated cracking was characterized in this study in terms of lateral length and depth. Although the fracture probability of SiC increases with temperature differences [88], it is very hard to predict crack generation and propagation.

In order to separate the effect of oxidation on MRR enhancement from that of laser induced cracks, argon gas was used as an assist gas in this study. In laser beam machining, the removal depth using oxygen was higher than with argon gas [43], suggesting that argon can affect surface heating and ultimately cracking during laser beam irradiation.

## 6.3. Hybrid Process

It was demonstrated in the current study that laser induced crack generation enhanced the MRR of the successive process. However, there are many parameters, both in polishing and lasers irradiation, which should be studied before the hybrid process can be an industrial application. And, a well-designed combination of serial or hybrid processes should be developed for more practical application.

In this study, surface roughness was evaluated to determine surface integrity. However, other factors can be used to evaluate surface integrity, such as residual stress or subsurface damage.

# Chapter 7. Conclusion

According to the review of previous literature, LAM was carried out without a water-based coolant or slurry, therefore, research work on hybrid LaPol had not been published yet. In this study, the first attempt at LaPol in a slurry environment was made by combining a $CO_2$ laser source and mechanical polishing, achieving an enhancement of the MRR with no significant difference in surface roughness, as compared to that in a normal polishing process. After 120 min of conducting the process, the MRR in the LaPol process increased by 79.03% as compared to that in the normal polishing process (Pol), and less than 15 nm of surface roughness was achieved in both the cases. In the successive process of laser induced crack generation and polishing, the effect of the pre-cracked surface on the material removal in subsequent polishing or LaPol process was investigated. Based on XRD and XPS analyses, it was concluded that the laser induced crack was the major facilitating factor in the removal mechanism as compared to a crystalline structure or laser induced surface oxidation. The MRR increased by 44.93% in Crk+Pol and 34.80% in Crk(Ar)+Pol, as compared to that in a normal polishing (Pol) process. The current study is expected to satisfy the increasing demand for various SiC application and to contribute to the expansion of hybrid machining field.

# Bibliography

[1]     J. J. Berzelius (1824). Untersuchungen über die Flussspathsäure und deren merkwürdigsten Verbindungen, *Annalen der Physik*, 77 (6) 169-230.

[2]     H. Moissan (1904). Nouvelles recherches sur la météorité de Cañon Diablo, *Competes Rendus*, 139 773-86.

[3]     N. W. Jepps and T. F. Page (1983). Polytypic transformations in silicon carbide, *Progress in crystal growth and characterization*, 7 (1-4) 259-307.

[4]     J. M. Casstevens, A. Rashed, R. Plummer, D. Bray, R. L. Gates, E. Lara-Curzio, M. K. Ferber, and T. Kirkland. (2001) Silicon carbide high performance optics: a cost-effective, flexible fabrication process, *International Symposium on Optical Science and Technology*, 458-467.

[5]     J. Robichaud, J. Schwartz, D. Landry, W. Glenn, B. Rider, and M. Chung. (2005) Recent advances in reaction bonded silicon carbide optics and optical systems, *Optics & Photonics 2005*, 586802-586802-7.

[6]     A. Beaucamp, P. Simon, P. Charlton, C. King, A. Matsubara, and K. Wegener (2017). Brittle-ductile transition in shape adaptive grinding (SAG) of SiC aspheric optics, *International Journal of Machine Tools and Manufacture*, 115 29-37.

[7]     Z. Li and R. C. Bradt (1986). Thermal expansion of the hexagonal (4 H) polytype of SiC, *Journal of Applied Physics*, 60 (2) 612-614.

[8]     G. L. Harris, *Properties of silicon carbide*. 1995: Iet.

[9]     M. E. Levinshtein, S. L. Rumyantsev, and M. S. Shur, *Properties of Advanced Semiconductor Materials: GaN, AIN, InN, BN, SiC, SiGe*. 2001: John Wiley & Sons.

[10]     C.-M. Zetterling, *Process technology for silicon carbide devices*. 2002: IET.

[11]     J. D. Reddy, A. A. Volinsky, C. L. Frewin, C. Locke, and S. E. Saddow (2007). Mechanical properties of 3C-SiC films for MEMS applications, *MRS Online Proceedings Library Archive*, 1049.

[12]     D. Malacara, *Handbook of optical engineering*. 2001: CRC Press.

[13]     T. Doi, E. Uhlmann, and I. D. Marinescu, *Handbook of ceramics grinding and polishing*. 2015: William Andrew.

[14]     L. Rayleigh (1917). Polish, *Transactions of the Optical Society*, 19 (1) 38.

[15]     F. Preston (1927). The theory and design of plate glass polishing machines, *J. Soc. Glass Tech.*, 11 214.

[16]     H. Y. Tam, H. Cheng, and Y. Wang (2007). Removal rate and surface roughness in the lapping and polishing of RB-SiC optical components, *Journal of Materials Processing Technology*, 192 276-280.

[17]     H. Cheng, L. Ren, Y. Feng, Y. Yam, H. Tong, and Y. Wang (2008). Mechanisms for grinding and polishing of silicon carbide with loose abrasive sub-aperture tools, *Advances in Manufacturing Technology–XXII*, 65.

[18]     F. Klocke and R. Zunke (2009). Removal mechanisms in polishing of silicon based advanced ceramics, *CIRP Annals-Manufacturing Technology*, 58 (1) 491-494.

[19]     G. Liu, Z. Huang, X. Liu, and D. Jiang (2010). Removal behaviors of different SiC ceramics during polishing, *Journal of Materials Science & Technology*, 26 (2) 125-130.

[20]     A. Kubota, Y. Hatasako, T. Takita, and M. Touge (2015). Abrasive-free polishing of single-crystal 4H-SiC with silica glass plates, *ECS Journal of*

*Solid State Science and Technology*, 4 (12) P468-P475.

[21]     Z. L. Li, W. B. Lee, B. C. Cheung, L. Ho, and Y. G. Fu. (2015) A study of computer controlled ultra-precision polishing of silicon carbide reflecting lenses for enhancing surface roughness, *Key Engineering Materials*, 437-445.

[22]     M. Tsai, S. Wang, C. Tsai, and T. Yeh (2015). Investigation of increased removal rate during polishing of single-crystal silicon carbide*, The International Journal of Advanced Manufacturing Technology*, 80 (9-12) 1511-1520.

[23]     J.-K. Ho, C.-Y. Huang, M.-Y. Tsai, and C.-C. Tsai (2016). Investigation of Polishing Pads Impregnated with Fe and Al2O3 Particles for Single-Crystal Silicon Carbide Wafers*, Applied Sciences*, 6 (3) 89.

[24]     Y. Gu, W. Zhu, J. Lin, M. Lu, and J. Sun (2017). Investigation of silicon carbide ceramic polishing by simulation and experiment*, Advances in Mechanical Engineering*, 9 (11) 1687814017729090.

[25]     B. Lauwers, F. Klocke, A. Klink, A. E. Tekkaya, R. Neugebauer, and D. Mcintosh (2014). Hybrid processes in manufacturing*, CIRP Annals-Manufacturing Technology*, 63 (2) 561-583.

[26]     J. Kozak and K. P. Rajurkar. (2000) Hybrid machining process evaluation and development, *Proceedings of 2nd international conference on machining and measurements of sculptured surfaces, Keynote Paper, Krakow*, 501-536.

[27]     S. Sun, M. Brandt, and M. Dargusch (2010). Thermally enhanced machining of hard-to-machine materials—a review*, International Journal of Machine Tools and Manufacture*, 50 (8) 663-680.

[28]     C. Brecher, M. Emonts, C.-J. Rosen, and J.-P. Hermani (2011). Laser-

assisted milling of advanced materials, *Physics Procedia*, 12 599-606.

[29]  D.-H. Kim and C.-M. Lee (2014). A study of cutting force and preheating-temperature prediction for laser-assisted milling of Inconel 718 and AISI 1045 steel, *International Journal of Heat and Mass Transfer*, 71 264-274.

[30]  N. Kobayashi, Y. Wu, M. Nomura, and T. Sato (2008). Precision treatment of silicon wafer edge utilizing ultrasonically assisted polishing technique, *Journal of Materials Processing Technology*, 201 (1-3) 531-535.

[31]  F.-J. Shiou and H.-S. Ciou (2008). Ultra-precision surface finish of the hardened stainless mold steel using vibration-assisted ball polishing process, *International Journal of Machine Tools and Manufacture*, 48 (7-8) 721-732.

[32]  H. Suzuki, S. Hamada, T. Okino, M. Kondo, Y. Yamagata, and T. Higuchi (2010). Ultraprecision finishing of micro-aspheric surface by ultrasonic two-axis vibration assisted polishing, *CIRP Annals-Manufacturing Technology*, 59 (1) 347-350.

[33]  W. M. Lin, S. K. Chee, H. Suzuki, and T. Higuchi. (2013) Polishing Characteristics of a Low Frequency Vibration Assisted Polishing Method, *Advanced Materials Research*, 450-454.

[34]  H. Cheng, Z. Feng, Y. Wang, and S. Lei (2005). Magnetorheological finishing of SiC aspheric mirrors, *Materials and Manufacturing Processes*, 20 (6) 917-931.

[35]  H. Yamaguchi, K. Yumoto, T. Shinmura, and T. Okazaki (2009). Study of finishing of wafers by magnetic field-assisted finishing, *Journal of advanced mechanical design, systems, and manufacturing*, 3 (1) 35-46.

[36]  K. Yamamura, T. Takiguchi, M. Ueda, H. Deng, A. Hattori, and N. Zettsu (2011). Plasma assisted polishing of single crystal SiC for obtaining atomically flat strain-free surface, *CIRP Annals-Manufacturing Technology*,

60 (1) 571-574.

[37]     N. Takahashi, Y. Toyokawa, Y. Yamada, and J. Ikeno (2017). Study on laser assisted polishing of SiC, *Proceedings of JSPE Semestrial Meeting*, 2017S 519-520.

[38]     X. Yang, X. Liu, L. Wang, H. Zhang, X. Yao, and Z. Huang (2017). Effects of artificial defect on the material residual strength of SiC ceramics after thermal-shock, *Materials Science and Engineering: A*, 707 159-163.

[39]     P. Shukla, S. Nath, G. Wang, X. Shen, and J. Lawrence (2017). Surface property modifications of silicon carbide ceramic following laser shock peening, *Journal of the European Ceramic Society*, 37 (9) 3027-3038.

[40]     C. Wang, S. Kurokawa, T. Doi, J. Yuan, Y. Sano, H. Aida, K. Zhang, and Q. Deng (2017). The Polishing Effect of SiC Substrates in Femtosecond Laser Irradiation Assisted Chemical Mechanical Polishing (CMP), *ECS Journal of Solid State Science and Technology*, 6 (4) P105-P112.

[41]     X. Zhang, D. Wen, Z. Deng, S. Li, Q. Wu, and J. Jiang (2018). Study on the grinding behavior of laser-structured grinding in silicon nitride ceramic, *The International Journal of Advanced Manufacturing Technology*,    1-11.

[42]     H. Tönshoff and C. Emmelmann (1989). Laser cutting of advanced ceramics, *CIRP Annals-Manufacturing Technology*, 38 (1) 219-222.

[43]     M. Islam and G. Campbell (1993). Laser machining of ceramics: a review, *Material and Manufacturing Process*, 8 (6) 611-630.

[44]     N. B. Dahotre and S. Harimkar, *Laser fabrication and machining of materials*. 2008: Springer Science & Business Media.

[45]     A. K. Dubey and V. Yadava (2008). Laser beam machining—a review, *International Journal of Machine Tools and Manufacture*, 48 (6) 609-628.

[46] A. N. Samant and N. B. Dahotre (2009). Laser machining of structural ceramics—a review, *Journal of the European Ceramic Society*, 29 (6) 969-993.

[47] W. M. Steen and J. Mazumder, *Laser material processing*. 2010: Springer Science & Business Media.

[48] P. Parandoush and A. Hossain (2014). A review of modeling and simulation of laser beam machining, *International journal of machine tools and manufacture*, 85 135-145.

[49] S. M. Copley, M. Bass, and R. G. Wallace. (1979) Shaping silicon compound ceramics with a continuous wave carbon dioxide laser, *Proc. 2nd Symp. "The Science of Ceramic Machining and Surface Finishing", spec. publ. Not. Bureau of Standards*, 283-293.

[50] Z. Zhang and M. Modest (1998). Energy requirements for ablation or decomposition of ceramics during CO 2 and Nd: YAG laser machining, *Journal of Laser Applications*, 10 (5) 212-218.

[51] D. Sciti and A. Bellosi (2001). Laser-induced surface drilling of silicon carbide, *Applied Surface Science*, 180 (1) 92-101.

[52] H. Wang, H. Lin, C. Wang, L. Zheng, and X. Hu (2016). Laser drilling of structural ceramics—A review, *Journal of the European Ceramic Society*.

[53] A. N. Samant and N. B. Dahotre (2010). Three-dimensional laser machining of structural ceramics, *Journal of Manufacturing Processes*, 12 (1) 1-7.

[54] A. J. DeMaria and T. V. Hennessey Jr (2010). The CO2 Laser: The Workhorse of the Laser Material Processing Industry, *SPIE Professional Magazine*.

[55] G. Chryssolouris, *Laser machining: theory and practice*. 2013: Springer Science & Business Media.

[56]    J. Verhoeven, J. Jansen, R. Mattheij, and W. Smith (2003). Modelling laser induced melting, *Mathematical and Computer Modelling*, 37 (3-4) 419-438.

[57]    J. Roy, S. Chandra, S. Das, and S. Maitra (2014). Oxidation behaviour of silicon carbide-a review, *Rev. Adv. Mater. Sci*, 38 (1) 29-39.

[58]    T. Lichko, Y. A. Kryl, and V. Rymar (1993). High-temperature reaction between silicon carbide and nitrogen under pressure, *Powder metallurgy and metal ceramics*, 32 (4) 281-285.

[59]    P. Shukla and J. Lawrence, *Characterization and modification of technical ceramics through laser surface engineering*, in *Laser Surface Engineering*. 2015, Elsevier. p. 107-134.

[60]    W. D. Callister Jr and D. G. Rethwisch, *Fundamentals of materials science and engineering: an integrated approach*. 2012: John Wiley & Sons.

[61]    L. Ji, Y. Yan, Y. Bao, and Y. Jiang (2008). Crack-free cutting of thick and dense ceramics with $CO_2$ laser by single-pass process, *Optics and Lasers in Engineering*, 46 (10) 785-790.

[62]    W. Spitzer, D. Kleinman, and D. Walsh (1959). Infrared properties of hexagonal silicon carbide, *Physical Review*, 113 (1) 127.

[63]    Z. Tong, L. Liu, L. Li, and H. Bao (2018). Temperature-dependent infrared optical properties of 3C-, 4H-and 6H-SiC, *Physica B: Condensed Matter*, 537 194-201.

[64]    Z. Zhang and M. Modest (1998). Temperature-dependent absorptances of ceramics for Nd: YAG and $CO_2$ laser processing applications, *Transactions-American Society of Mechanical Engineers Journal of Heat Transfer*, 120 322-327.

[65]    I. Shigematsu, K. Kanayama, A. Tsuge, and M. Nakamura (1998). Analysis of constituents generated with laser machining of Si3N4 and SiC, *Journal*

*of materials science letters*, 17 (9) 737-739.

[66]   W. M. Haynes, *CRC handbook of chemistry and physics*. 2014: CRC press.

[67]   R. Aghan and L. E. Samuels (1970). Mechanisms of abrasive polishing*, Wear*, 16 (4) 293-301.

[68]   C. J. Evans, E. Paul, D. Dornfeld, D. A. Lucca, G. Byrne, M. Tricard, F. Klocke, O. Dambon, and B. A. Mullany (2003). Material removal mechanisms in lapping and polishing*, CIRP Annals-Manufacturing Technology*, 52 (2) 611-633.

[69]   J. Luo and D. A. Dornfeld (2001). Material removal mechanism in chemical mechanical polishing: theory and modeling*, IEEE transactions on Semiconductor Manufacturing*, 14 (2) 112-133.

[70]   D. A. Hanaor, Y. Gan, and I. Einav (2015). Contact mechanics of fractal surfaces by spline assisted discretisation*, International Journal of Solids and Structures*, 59 121-131.

[71]   H. Hertz, *On the contact of rigid elastic solids and on hardness, chapter 6: Assorted papers by H. Hertz*. 1882, MacMillan, New York.

[72]   K. L. Johnson and K. L. Johnson, *Contact mechanics*. 1987: Cambridge university press.

[73]   I. N. Sneddon (1965). The relation between load and penetration in the axisymmetric Boussinesq problem for a punch of arbitrary profile*, International Journal of Engineering Science*, 3 (1) 47-57.

[74]   K. J. P. Johnson, Cambridge (1985). Contact Mechanics Cambridge Univ.

[75]   G. Straffelini (2015). Friction and Wear*, Springer International Publishing, Switzerland. doi*, 10 978-3.

[76]    H. Rahnejat, *Tribology and dynamics of engine and powertrain: fundamentals, applications and future trends*. 2010: Elsevier.

[77]    E. Rabinowicz and R. Tanner (1966). Friction and wear of materials, *Journal of Applied Mechanics*, 33 479.

[78]    M. Jenkins and A. Stamboulis, *Durability and reliability of medical polymers*. 2012: Elsevier.

[79]    Z. Dong and H. Cheng (2014). Study on removal mechanism and removal characters for SiC and fused silica by fixed abrasive diamond pellets, *International Journal of Machine Tools and Manufacture*, 85 1-13.

[80]    N. Diaz, E. Redelsheimer, and D. Dornfeld, *Energy consumption characterization and reduction strategies for milling machine tool use*, in *Glocalized solutions for sustainability in manufacturing*. 2011, Springer. p. 263-267.

[81]    S. Kara and W. Li (2011). Unit process energy consumption models for material removal processes, *CIRP Annals-Manufacturing Technology*, 60 (1) 37-40.

[82]    M. U. s. Guide (1998). The mathworks, *Inc., Natick, MA*, 5 333.

[83]    H. Cheng, *Independent variables for optical surfacing systems*. 2016: Springer.

[84]    S. Agarwal and P. V. Rao (2008). Experimental investigation of surface/subsurface damage formation and material removal mechanisms in SiC grinding, *International Journal of Machine Tools and Manufacture*, 48 (6) 698-710.

[85]    T. Suratwala, L. Wong, P. Miller, M. Feit, J. Menapace, R. Steele, P. Davis, and D. Walmer (2006). Sub-surface mechanical damage distributions during grinding of fused silica, *Journal of Non-Crystalline Solids*, 352 (52-54)

5601-5617.

[86]     W. H. Bragg and W. L. Bragg (1913). The reflection of X-rays by crystals, *Proc. R. Soc. Lond. A*, 88 (605) 428-438.

[87]     R. Hoffmann, *The same and not the same*. 1995: Columbia University Press.

[88]     H. Uchimura, A. Kokaji, and M. Kaji. (1992) Evaluation of fast fracture strength of ceramic components under multiaxial stress states, *ASME 1992 International Gas Turbine and Aeroengine Congress and Exposition*, V002T04A011-V002T04A011.

# Acknowledgement

# Appendix

## A1.  Optical Microscope

➢ Model: BX53M + BX3M-LEDR (Olympus)

➢ Light source: reflected white LED 5700K

➢ White balanced with silicon wafer, exposure 800 μs and amplification 30 %

**Table. Specification of observing condition**

| Magnification | x50 | x500 |
|---|---|---|
| Eyepiece | x10 | x10 |
| Objective lens | x5 | x50 |
| Numerical aperture (NA) | 0.15 | 0.5 |
| Working distance (WD) [mm] | 20 | 10.6 |
| Objective Field Number [mm] | 26.5 | 26.5 |
| Luminance [%] | 35 | 60 |

## A2.  Surface Profiler

➢ Model: SJ-410 (Mitutoyo)

➢ Resolution: 0.0001 μm (8 μm Z range)

➢ Stylus: Tip radius 2 μm, angle 60°

➢ Standard: ISO 4287-1996 and -1997

➢ Gaussian Filter: ISO 11562-1996

**Table. Specification of measuring condition**

| Roughness range [μm] | Ra ≤ 2.0 | Ra ≤ 0.02 |
|---|---|---|
| Cut-off length, λs [μm] | 2.5 | 2.5 |
| Number of sampling length, N | 5 | 20 |
| Traversal speed [mm/s] | 0.5 | 0.05 |
| Traverse length [mm] | 4.8 | 1.68 |

## A3.    Non-contact 3D Surface Profiler

➢ Model: CCI-Optics-RM (Taylor Hobson)

➢ Measuring area : 0.8 mm x 0.8 mm

➢ Pixel: 1024 x 1024

➢ Objective lens: 20x (zoon x1)

➢ Filter: 0.08 mm (cut-off)

➢ Measuring points: 15 pts

➢ Standard: ISO 25178

➢ Gaussian Filter: ISO 16610

    ■ ISO 16610-21, Linear profile filters (published 2011)

    ■ ISO 16610-61, Linear areal filter (published 2015)

# A4.    Tool Path Generator: MATLAB Code

```matlab
%% Initialize
clear all;
close all;
clc;

% Origin of the tool path
Xorg = 355.00; Yorg = -332.00;
ORIGIN = [Xorg Yorg];

r = 65/2;   % radius of the workpiece

type = 'spiral' % or 'raster'

raster_dist = 1;     % raster distance

deg_inc = 1;
nR = round(r/3);   % number of rotation

%% TOOL path generation
if type == 'raster'

    p = [-r, r; r, -r];

    scan_no = 2*r/raster_dist;

    if mod(scan_no,2) == 0
        scan_no = scan_no + 1;
    end

    n_pts = scan_no * 2;

    y_temp = linspace(p(1, 2), ...
        p(2, 2), scan_no);
    y_temp2 = [y_temp; y_temp];

    yi = y_temp2(1:end)';

    for i = 1:length(y_temp)
        [xintemp(i, :), yintemp(i, :)] = ...
            linecirc(0, y_temp(i), 0, 0, r);
    end

    idx = find(isnan(xintemp(:, 1)));

    xintemp(idx, :) = [];
    xi_temp = xintemp(:, 1);
    x_temp2 = [xi_temp'; xi_temp'];
    xi_temp = x_temp2(1:end)';

    x_temp = [];    x_temp2 = [];
```

```matlab
        yintemp(idx, :) = [];
        yi_temp = yintemp(:, 1);
        y_temp2 = [yi_temp'; yi_temp'];
        yi = y_temp2(1:end)';

        y_temp = [];    y_temp2 = [];

        px = [1, -1];

        temp = '1221';
        x_temp = [];
        for i = 1:ceil(length(yi) / length(temp))
            x_temp = cat(2, x_temp, temp);
        end

        x_temp2 = x_temp(1:length(yi));

        for i = 1:length(x_temp2)
            xi(i) = xi_temp(i) * px(str2num(x_temp2(i)));
        end

        xi = transpose(xi);

        ang=0:raster_dist:2*pi;
        xp=r*cos(ang)+Xorg;
        yp=r*sin(ang)+Yorg;

        XX = xi  + Xorg;
        YY = yi  + Yorg;

elseif type == 'spiral'
        deg_init = 0;
        theta = deg2rad(deg_init : deg_inc : 360*nR);

        R = r * theta/max(theta);

        [X1, Y1] = pol2cart(theta, R);
        [X3, Y3] = pol2cart(theta, -R);

        % from edge to center, then to edge
        X = [fliplr(X3) X1]'+ Xorg;
        Y = [fliplr(Y3) Y1]'+ Yorg;

        %
        d_cri= 3*pdist([X(end) Y(end); ...
            X(end-1) Y(end-1)], 'euclidean');

        d=zeros(size(X));

        temp = 0;
        idx = [];
        for i=2:length(X)
            pts_set = [X(i), Y(i); X(i-1), Y(i-1)];
            d(i) = pdist(pts_set, 'euclidean');
            temp = temp + d(i);
            if (temp >= d_cri)
```

```matlab
            idx = cat(2, idx, i-1);
            temp = 0;
        end
    end

    XX1 = X(idx);
    YY1 = Y(idx);


    XX2 = flipud(XX1);
    YY2 = flipud(YY1);

    XX = [XX1; XX2];
    YY = [YY1; YY2];

    % summation of tool path distances
    d = zeros(size(XX));
    for i=2:length(XX)
        pts_set = [XX(i), YY(i); XX(i-1), YY(i-1)];
        d(i) = pdist(pts_set, 'euclidean');
    end
    L_tot = sum(d);

    F = 25.0; % in mm/sec

    time_spent = L_tot / F;

end

%% Visualizatoin and verification of the tool path
figure()
set(gcf, 'pos', [800 200 525 545]);

box on;
plot(XX, YY, 'linewidth', 1); grid on;
fo = 'times new roman';
sz = 14;
set(gca, 'color', 'none', 'FontSize', sz, ...
    'FontName', fo, 'FontWeight', 'bold')
axis([320 390 -370 -290])

xlabel('X [mm]')
ylabel('Y [mm]')

%% Generation of the G-code for tool path

G = repmat({'G01'}, size(XX));

X = repmat({' X'}, size(XX));
GX = cellstr(num2str(XX, '%.5f\n'));

Y = repmat({' Y'}, size(XX));
GY = cellstr(num2str(YY, '%.5f\n'));

GXY = [G X GX Y GY];
```

118

```matlab
XY = [XX YY];

TP = cell(length(GXY), 1);

for i = 1:length(GXY)
    TP{i} = strjoin(GXY(i, :));
end

writetable(cell2table(TP), 'TP.txt');
winopen('TP.txt')
```

**Appx. 1 | Tool path generator Matlab code**

# 국 문 초 록

실리콘 카바이드는 우주 광학 분야에서 거울 또는 그 구조체로 사용될 수 있는 가장 좋은 재료 중 하나이다. 그 이유는 재료 고유의 낮은 밀도, 높은 강성, 낮은 열팽창, 내화학성 등 우수한 기계적 물성 및 화학적 특성을 갖고 있기 때문이다. 광학부품을 만들기 위해서 재료는 폴리싱 공정을 거치면서 형상 정밀도와 표면 조도를 동시에 만족시켜야 한다. 그러나 오직 수 마이크로미터 수준의 재료 제거를 목표로 하는 폴리싱 공정은 시간이 가장 많이 소요되는 공정 중 하나이다. 뿐만 아니라, 재료 자체의 아주 높은 경도와 취성으로 인해, 실리콘 카바이드는 터닝 또는 밀링 공정과 같은 전통적인 방법으로는 가공이 매우 어렵고 비용이 많이 소비된다.

실리콘 카바이드의 표면 폴리싱에 대한 연구는 단순 기계적 폴리싱에서부터 플라즈마, 자기장 또는 초음파 등의 외부 보조 에너지원을 사용하는 하이브리드 폴리싱에 이르기까지 다양한 연구가 수행된 바 있다. 하지만 기존 연구의 대부분은 주로 표면 조도 향상을 목적으로 하고 있어, 폴리싱의 재료제거율 향상에 대한 연구는 여전히 부족한 실정이다. 레이저는 하이브리드 가공에서 생산성 향상을 목적으로 자주 이용되는 외부 에너지원이지만, 폴리싱 공정에 보조 에너지원으로서 적용된 사례는 없다.

　본 연구에서는 $CO_2$ 레이저와 슬러리 기반의 기계적 폴리싱 장치를 결합함으로써, 레이저 보조 폴리싱 (Laser assisted polishing, LaPol) 공정을 새롭게 개발하여 실리콘 카바이드의 폴리싱 생산성을 향상시키고자 한다. 레이저 빔은 자체 제작된 하이브리드 공구의 내부로 조사(照射)되어 재료 표면까지 집속 도달될 수 있으며, 공구의 회전과 동기화되어 조사될 수 있다. 재료 표면에 레이저 유도 미세 크랙을 생성하여 이 크랙이 이어지는 폴리싱 공정의 생산성에 미치는 영향에 대해 평가했다. 이를 위해, 출력에 따른 레이저 유도 미세 크랙의 길이와 깊이, 표면 경도 및 표면 거칠기가 평가되었으며, 더불어 레이저 조사 전/후의 결정 구조 변화 및 구성 원소 변화를 평가했다. 레이저 유도 미세 크랙을 생성한 후, 레이저 보조 폴리싱을 수행했을 때, 기존 폴리싱에 비해 재료제거율이 79% 향상되었으며, 레이저 유도 미세 크랙 생성 후 일반 기계적 폴리싱을 수행했을 때는 표면의 손상 없이 45%의 재료제거율 향상 효과를 얻었다. 본 연구에서 제안된 레이저 보조 폴리싱과 그 재료 제거 메커니즘은 다양한 하이브리드 가공 분야 및 실리콘 카바이드의 산업적 응용 분야 확장에 기여할 것으로 기대한다.

중심어: 하이브리드 가공, 표면마무리, 레이저 보조 폴리싱, 실리콘 카바이드, 세라믹

**학번:** 2013-30943